# High redshift Lyman-α hunt
Galaxies as precious forged jewels

Ia Kochiashvili

Dissertation
Submitted for the Degree
Philosophiæ Doctor
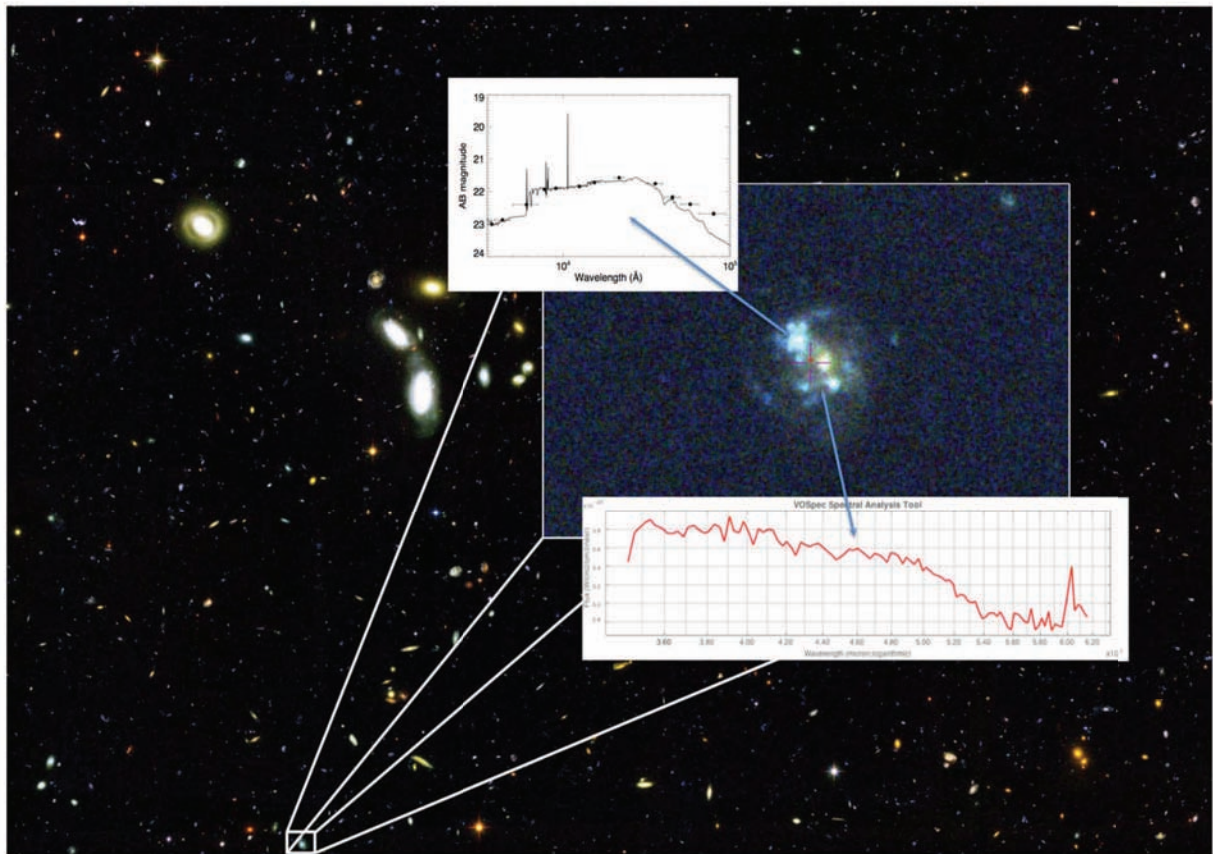
Dark Cosmology Centre
The PhD School of Science
Faculty of Science
University of Copenhagen

Acknowledgements

First of all, I would like to thank Jens Hjorth, Marianne Vestergaard and Kristian Pedersen for giving me this wonderful, life-changing opportunity to work at DARK.

Many thanks to my supervisor, Johan Fynbo and to Lise Christensen and Bo Milvang-Jensen for help and support. Special thanks to Palle Møller for being a great mentor and for supporting me in my research. Thanks to Kim Nilsson for helping me out with my very first steps in our field. Thanks to all my DARK colleagues, who became my lifetime friends. I will always keep in my heart beautiful memories of the time I spent with you all and I hope I will have opportunities to come back to visit the centre and collaborate with you! Thanks to Daniele, Antonio, Radek, Martina, Ece, Matteo, Nicolò and everyone else, whose name might be missing from this list, but who equally deserves to be named here, for the wonderful hours, days and years together in many adventures across Denmark and the World!

Special thanks to Julie Meier, for being the person I could always count on.

Many thanks to my opponents, Anja Andersen, Simona Mei and Páll Jakobsson for taking the time to read and evaluate this thesis.

I would also like to thank my family: my wonderful mother, Nino, who has always been not only a parent, but most importantly, my best friend. Thanks for the nights I slept in the telescope dome, while you were observing; for the starry skies I've seen at dawn, when coming back home, wondering about what those twinkling little dots looked like from nearby. Thanks to Pasquale and Idolina for Alberto, the greatest gift of my life.

And finally, thanks to my two biggest loves - my baby, whom I am looking forward to meet in a few months and my dearest husband, Alberto, for his endless love, his support and attention, which I feel every single second. My love, thank you for making my life a living fairytale!

Abstract

Galaxy formation and evolution has been intensively studied in the past two decades. Results and discoveries revolutionized the field and we now have much better understanding of how these huge conglomerates of baryonic and dark matter evolve.

In the framework of two different projects, which constitute the backbone of this thesis, I investigated the nature of almost 100 emission-line galaxies selected with the narrow-band selection method. These candidates can be: galaxies with Hα emission lines at redshift $z \sim 0.6$, [OIII]/Hβ emission-line galaxies at redshift $z \sim 1.15$ and [OII] emitters at $z \sim 1.85$.

I used the near-infrared data from NB1060, Y and J filters to perform colour-colour and colour-magnitude selections. With the broad-band data from CANDELS catalogue, I performed SED fitting and derived photometric redshifts and other physical properties for the candidate emission-line galaxies. Significant differences between the two selection methods have been found. The colour-colour selection method, tends to pick galaxies with high colour excess and can leave some strong emission-line candidates with relatively lower colour excess out of the sample. The populations of selected galaxies can also be very biased. The colour-magnitude selection method picks not only "normal" galaxies, but also starburst ones.

I investigated the physical properties and colour indices for the selected galaxies, obtaining the following results. *I)* Stellar masses for narrow-band selected galaxies are found to be in the range $M_* \sim 10^7 - 10^{11} M_\odot$. The derived star-formation rates suggest that they can be either normal galaxies in the main sequence of the M_* vs. SFR relation, or starburst ones. *II)* A steepening of the M_* vs. SFR slope for the galaxies in the lower part of the mass range ($M_* < 10^{9.4} M_\odot$) is found. *III)* From studying the spatial distribution of our sample the discovery of a galaxy protocluster at the redshift of $z = 1.85$ and the likely discovery of a filament at $z = 1.15$ are reported. The identification of these gravitationally bound structures holds regardless of selection method employed in the analysis.

In this thesis, I also briefly summarise the first results of an on-going investigation of galaxies selected according to their robust spectroscopic redshifts from the large MUSYC multiband survey. The aim of this project is to study the evolution of the physical properties of galaxies across large redshift range ($0 < z < 6$) and see their implications on the evolution of the universe.

ABSTRAKT

Galaksedannelse og udvikling har været et aktivt forskningsområde i flere årtier. Særligt i 1990erne skete der en revolution i forskningen og vi har nu en meget bedre forståelse af, hvordan disse enorme konglomerater af baryonisk og mørkt stof dannes og udvikler sig.

I forbindelse med to forskellige projekter, der udgør rygraden i denne afhandling, har jeg undersøgt naturen af næsten 100 emission-line galakser udvalgt på baggrund af smalfilter fotometri. Disse kandidater kan være: galakser med Hα emissionslinjer ved en rødforskydning på $z \sim 0.6$, [OIII]/Hβ emissionslinegalakser ved en rødforskydning på $z \sim 1.15$ og endelig [OII]-galakser ved $z \sim 1.85$.

Jeg har benyttet nær-infrarøde data fra NB1060 smalfilteret, samt de normale Y og J bredfiltre til at udføre farve-farve og farve-størrelsesklasse udvælgelser. Ved hjælp af yderligere data fra CANDELS kataloget har jeg udmålt spektrale energifordelinger og afledt fotometriske rødforskydninger og andre fysiske egenskaber ved kandidat emission-line galakserne. Væsentlige forskelle er blevet fundet mellem de to udvalgssmetoder. Farven-farve-metoden har tendens til at udvælge galakser med kraftige emissionslinje ækvivalentbredder og overser nogle stærke emissionlinje kandidater med relativt lavere ækvivalentbredde. Farve-størrelsesklasse-udvalgelsesmetoden opfanger ikke kun "normale" stjernedannende galakser, men også starburstgalakser.

Jeg har også undersøgt de fysiske egenskaber og farveindekser for de valgte galakser og derved opnået følgende resultater. *I)* Stellarmasser af de udvalgte galakser findes at være i intervallet $M_* \sim 10^7 - 10^{11} M_{\odot}$. De afledte stjernedannelsesrater tyder på, at nogle er normale galakser på hovedserien for stjernedannende galakser og starburstsgalakser over hvoeserien. *II)* En stejlere M_* vs. SFR hældning for galakserne i den nederste del af masseområdet ($M_* < 109.4 M_{\odot}$) er fundet. *III)* Ved at studere den rumlige fordeling af vores galakser har vi opdaget en protocluster ved en rødforskydning på $z = 1.85$. Desuden er der en mulig filamentær struktur ved $z = 1.15$. Identifikationen af disse storskalastrukturer er ikke afhængig af udvælgelsesmetoden anvendt i analysen.

აბსტრაქტი

გალაქტიკების წარმოშობისა და ევოლუციის შესწავლა ასტრონომების ნიერ აქტიურად მიმდინარეობს ბოლო ორი ათწლეული ა. ამ დ ო ის ნ ნამდვილ ბი ნ ნ ნ ბ შ ბ ბ ბ ბ ად მ ჩ ნ ებ ა მოახდინეს გადატრიალება ნ ცნიერების ამ დ ო კ დ ა დ ა თ ი ს ჩ ნ გ ა ა ა ნ ბ უ კ თ ესი ცოდნა, თუ რას წარმოადგენს ბარიონული და ბ ნ ი ნ ნ ე ი ა ნ შ ე გ ნ ი ს უ ა უ ვ ლ ბ ი ხსოვ ბ ბ ი.

ორი პროექტის ფა გლ ბ ი, რომ ლ ც ამ თ ზ ს ი ნ ა ა ა ა წ ი ს შ დ ბ ს, ნ ჩვ ა ე IC ე ი ხ უ ა ხ ი ნ ი ა ა ტ ი ნ ს ბ ნ ბ ს კლ კ. ე ა ა ა ი ბ შ ჩ ლ ი ნ ა ვ წ ო ო ო ვ ა შ ჩ ი ს მ თ დ. ე ი ხ უ ა ნ ი კ ნ დ ა ტ ბ შ ი ლ ი ი ო ს: ა ა ა ი ბ, $H\alpha$ გ მ ხ ვ ბ ს ხ ი ი, $z \sim 0.6$ წ თ ლ წ ნ ვ ლ ბ ზ, $[OIII]/H\beta$ ა [OII] გ მ ხ ვ ლ ბ, $z \sim 1.15$ ა $z \sim 1.85$ წ თ ლ წ ნ ვ ლ ბ ზ, შ ს ა ი ს ა.

ნ გ მ ვ ყ ნ ვ წ ო ო ო ვ ი NB1060 ა ფ ი ო ო ო ვ ი Y ა J ფ ლ ტ ბ ი ნ ლ ბ ლ ი მ ნ ც ბ ი კ ნ დ ა ტ ა ო ი ფ ი ს ნ შ ნ ბ ს ა ფ ი ს ნ შ ნ ბ ს ა ხ ლ ი ს ი ნ ი ნ შ ჩ ვ ა დ. შ ჩ ლ ი კ ნ დ ა ტ ბ ს თ ი ს გ მ ვ ყ ნ ფ ტ მ ტ ლ ი ა კ ვ ბ CANDELS კ ა ლ ი დ ნ, ა ე ს ტ ლ ი ნ გ ს ნ წ ლ ბ ი, ნ ვ ა ა ა ი ა ა ი ფ ტ ნ ტ ლ ი წ თ ლ წ ნ ვ ლ ბ ი ა ხ ვ ფ ი ი კ ი ი ნ ხ ა ი თ ბ ი. ო ი ხ ვ ა ს ხ ა შ ჩ ვ ს ნ თ დ ი ნ ლ ი შ დ ბ ს მ ი ა ო ი ნ ი შ ნ ლ ი ვ ი გ ნ ხ ვ ა ბ ი ნ ა წ ო ნ ი. კ ო ი, ფ ი ს ნ შ ნ ბ ლ ი თ ი შ ჩ ვ ს ნ თ დ ი ს თ ი ს ა ნ ხ ა ი თ ბ ლ ი ი ს ი გ ა ა ა ი ბ ს შ ჩ ვ ა, რ ო ლ ი ა ც ნ დ ლ ი ფ ი ს ნ შ ნ ბ ლ ბ ი ა კ ი. ა ნ თ ო ი ნ შ ს ა ი ლ ა კ ლ ვ ს ნ ი დ ნ ა ტ ო ვ ს ზ გ ი თ ი კ ა კ ა ე ი ხ უ ა ხ ი ნ ი კ ნ დ ა ტ ი გ ა ა ა ი კ ა, რ ო ლ ს ა ც შ დ ა ბ ი თ ხ უ ს ტ ი ფ ი ს ნ შ ნ ბ ლ ი ა კ ვ ს. შ ჩ ლ ი გ ა ა ა ი ბ ს პ პ ლ ა ი ა ც ე ვ ლ ც ი ს ა ა უ ლ ი ს უ ა ს ა ს ა ხ ა ვ ს. ფ ი ს ნ შ ნ ბ ლ ი თ ა ა ხ უ ს ტ ი ს ი დ ი თ შ ჩ ვ ს ნ თ დ კ ა ა ბ ლ ი ა ' ნ ო ლ უ ' გ ა ა ა ი კ ბ ს ა ვ დ ე ს კ ლ ვ ს ი ა, ა ა ე ე ი.წ. ' ს ტ ა ბ ა ს ტ ბ ს ა ც ' (გ ა ა ა ი კ ბ ს, რ ო ლ ი ა ვ ა ს კ ლ ა ვ ი წ ო ო ო ვ ი ს ტ მ ი ნ ო ა ლ უ ი თ ა ნ შ დ ა ე ი თ IC ა ნ ჯ ე ნ ა ა ა ი).

ნ გ მ ვ კ ვ ლ ვ შ ჩ ლ ი გ ა ა ა ი ბ ს ფ ი ი კ ი ი თ ვ ს ბ ბ ი ა ნ ვ ა შ დ ე ი ხ ს ი ს შ დ ბ ს: $I)$ ვ წ ო ო ო ვ ი ფ ლ ტ ი თ შ ჩ ლ ი გ ა ა ა ი კ ა ა ვ ა ს კ ლ ა ვ ი ი ა ს ბ ი ნ ც ლ ბ ს დ ი დ შ უ ა ლ ე ბ ი - $M_* \sim 10^7 - 10^{11} M_\odot$. ნ ი ლ ბ ლ ი ვ ა ს კ ლ ა ვ ი წ ო ო ო ვ ი ს ტ ნ ს ი ს ს ი დ ი თ, გ ა ა ა ი ბ ი შ ი ლ ბ ა ნ დ ა ო ბ დ ე ნ ნ ა ს ა ა ვ ა ს კ ლ ა ვ ი წ ო ო ო ვ ი ს ტ ნ ს ი ს ა მ ი კ ი დ ბ ლ ბ ი ს ა ნ ' ი ა ა ა ნ ი ნ დ ვ ო ო ბ ზ ', ა ნ ს ტ ა ბ ა ს ტ ბ ს ა ე ი. $II)$ ვ ჰ ვ ლ, რ ო ვ ა ს კ ლ ა ვ ი ი ა ს ბ ა ა ვ ა ს კ ლ ა ვ ი წ ო ო ო ვ ი ს ტ ნ ს ი ს ა მ ი კ ი დ ბ ლ ბ ი ს ო ლ ი ც ი კ ბ ო ა ი ს ა ა ი ლ ი ნ ი ა ნ ა ს ბ ი ს გ ა ა ა ი ბ ს შ ნ ი ვ ლ ს ი ($M_* < 10^{9.4} M_\odot$). $III)$ კ ნ დ ა ტ ბ ს ს ი ვ ლ ი გ ნ წ ლ ბ ს შ ს ა ვ ლ ს შ დ ბ ა დ ნ ხ დ ა $z = 1.85$ წ თ ლ წ ნ ვ ლ ბ ზ გ ა ა ა ი ი გ ო ვ ს, ა $z = 1.15$ წ თ ლ წ ნ ვ ლ ბ ზ გ ა ა ა ი ი ბ ჯ ს (filament) ნ ა ა ა ბ ა თ ი ა ნ მ ო ს ი ნ ა. ა ნ გ ა ვ ი ტ ც ი ლ ა დ შ კ ა ვ ი ბ ლ ი ს ტ ნ ქ ტ ლ ი ს ი დ ნ ი ი კ ა ი ა დ ა ო ბ დ ა ლ ი ა ა ი ს შ ჩ ვ ს ნ თ დ ზ.

ა ნ თ ი ხ ი ს შ ი ნ ა ს ა წ ო ვ დ გ ნ პ ჰ ლ ა დ შ დ ბ ს ნ დ ი ა ი პ ო ე ტ ი ს თ ა ო ბ ზ, რ ო ლ ს ფ ა გ ლ ბ ა წ ყ ვ ა ა ც MUSYC კ ა ლ ი დ ნ ს ტ ლ ო ს კ პ ი წ თ ლ წ ნ ვ ლ ბ ი ნ ი ლ დ ვ ი თ შ ჩ ლ ი გ ა ა ა ი ბ ს. პ ო ე ტ ი ს ნ მ ა ნ ი გ ა ა ა ი ბ ს ფ ი ი კ ი ი თ ვ ს ბ ბ ი ს ე ვ ლ ც ი ს შ ს ა ვ ლ ა დ ი დ წ თ ლ წ ნ ვ ლ ბ ი ს ი ა პ ა ზ ო ნ შ $(0 < z < 6)$ ა ს ა ა ა ო ს ე ვ ლ ც ა თ ა ნ ნ ა თ ი კ ა ვ ი ს ი ს დ ა დ გ ნ ა.

CONTENTS

1

INTRODUCTION

It is only shallow people who do not judge by the appearances, the true mystery of the world is the visible, not the invisible

Oscar Wilde, "The Picture of Dorian Gray"

1.1 GENERAL PROLOGUE

Curiosity has been one of the main driving forces in the progress of mankind. Curiosity that was transformed into useful knowledge made humans learn about and use nature's forces in their everyday life. The history of science in general and of astronomy in particular, is like a staircase - every step is needed to reach the one above. Every step is vital, every step is an achievement. In some of these steps, human civilisations learned that stars in the heavens were not pinned or painted on a giant vault, that they were not all at the same distance and that some of them were "wandering" across the sky in their specific patterns while others did not seem to move at all. It was accepted for centuries that planets revolve around the Earth in their specific orbits (Geocentric model). Until, in the 15th century Nicolaus Kopernikus argued that the Geocentric model of the universe was wrong and that the Earth was one of the planets orbiting around the Sun. A crucial step in the history of astronomy took place in 1609, when Galileo Galilei, for the first time, looked at the sky with a telescope. Galileo was the first human to see and sketch the moon from the telescope, to discover the four moons of Jupiter, called Galileian moons, to look at the Sun and find sunspots and to resolve the Milky Way into stars.

1.2 INSTRUMENTATION

Since Galileo's first observations in 1609, there has been tremendous progress in making new, bigger and more powerful instruments that would allow scientists to explore the skies above with more accuracy and make impressive discoveries.

1.2.1 BIG GROUND-BASED AND SPACE TELESCOPES

The progress of modern astronomy is largely based on ever improving telescopes and instruments, although a lot has changed with centuries. Unlike in early times, observational data nowadays is obtained not only with large ground-based telescopes, but also using space-bound facilities. In particular the early 1990es is an important period for modern astronomical facilities and technology.

April 1990 marks the beginning of the Hubble Space Telescope (HST) era. The HST became one of the most successful astronomical space projects, and brought a tremendous amount of data with extraordinary quality. With its 2.4m mirror, the HST is the biggest (so far) optical, near UV and near IR (together with the 3.5m FIR Herschel Space Observatory) telescope and played a crucial role in major discoveries and breakthroughs over more than two decades.

The milestone of progress in modern astronomical facilities in my opinion, still lies in the construction of the Very Large Telescope, although the project has been accepted only after the New Technology Telescope (NTT) saw its first light in 1989[1]. As the name implies, the latter was based on a new technology that ESO implemented and that had never been used before. Its 3.58m primary mirror has been made using special glass-ceramic material, with very low thermal expansion coefficient, which allows to build very thin and wide mirrors. Building thin, wide and undistorted mirrors is of a vital importance because a) a wide and undistorted mirror allows to collect more light and therefore achieve good depth and resolution, b) a thin mirror means less weight, which makes it possible to transport the mirror with less risks, and what is more important, handle it properly during observations. The way this could be achieved lies in the implementation of the active optics (Woltjer 2006), which allows to correct for even tiny deformation on the surface of the mirror by adjusting its shape with motion.

NTT was the sort of a test facility of ESO in order to accept the Very Large Telescope project. The Very Large Telescope (VLT) is the combination of four big monolithic mirror (8.2m) unit telescopes, which together with Japan's SUBARU (8.2m), GEMINI (8.1m) are among the largest monolithic telescopes in the World. VLT's first Unit Telescope (UT1, Antu) saw its first light in 1998 and the project has been completed in 2000. In 2004-2007 four 1.8m auxiliary telescopes have been mounted on the platform allowing the four UTs to work in the interferometer mode (Cesarsky 2000).

ESO's other major breakthrough is the successful implementation of Adaptive Optics. Adaptive Optics helps to correct for the atmospheric turbulence, therefore makes it possible to obtain very high quality imaging and spectral data[2].

1.2.2 INSTRUMENTS

All modern telescopes are equipped with a wide range of instruments covering different parts of the electromagnetic spectrum (spectrographs, photometers, spectro-polarimeters,

---

[1]`http://www.eso.org/sci/facilities/lasilla/telescopes/ntt.html`
[2]`https://www.eso.org/public/teles-instr/technology/adaptive_optics/`

etc.). Nowadays, the four UTs of VLT are equipped with 14 different instruments and two extra instruments for the interferometry mode. These are: CRIRES (CRyogenic high-resolution pre-dispersed InfraRred Echelle Spectrograph), FLAMES (Fibre Large Array Multi Element Spectrograph), FORS2 (FOcal Reducer/low dispersion Spectrograph 2), HAWK-I (High Acuity Wide field K-band Imager), KMOS (K-band Multi-Object Spectrograph), MUSE (Multi Unit Spectroscopic Explorer), NACO (Nasmyth Adaptive Optics System (NAOS) - Near-Infrared Imager and Spectrograph (CONICA)), SINFONI (Spectrograph for INtegral Field Observations in the Near Infrared), SPHERE (Spectro-Polarimetric High-contrast Exoplanet REsearch), UVES (Ultraviolet and Visual Echelle Spectrograph), VIMOS (VIsible Multi-Object Spectrograph), VISIR (VLT Imager and Spectrometer for mid Infrared), X-SHOOTER and MIDI (MID-infrared Interferometric instrument) and AMBER (Astronomical Multi-BEam combineR) for the Interferometry mode [3].

The HST, at the moment has six instruments on-board: WFC3 (Wide Field Camera 3), COS (Cosmic Origins Spectrograph), ACS (Advanced Camera for Surveys), STIS (Space Telescope Imaging Spectrograph), NICMOS (Near Infrared Camera and Multi-Object Spectrometer) and FGS (Fine Guidance Sensors).

The work presented in this thesis is mostly based on data from VLT's HAWK-I, VIMOS and X-SHOOTER instruments. Part of the work also included data from the decommissioned instrument ISAAC (Infrared Spectrometer And Array Camera) and the ACS and WFC3 instruments on-board HST.

1.2.3 DATA AND THE WAY WE HANDLE IT

New and modern telescopes deliver high quality data, which on the one hand, is very accurate and useful for exploring astronomical objects in greater detail, and on the other hand, gets bigger and bigger in size per data file, accumulates into the databases and becomes more and more demanding on computer power to download, process and use in everyday scientific work. For example, a single data file of the VISTA (Visible and Infrared Survey Telescope for Astronomy) telescope is as large as 9 GB, and this is just one file from one of the large telescopes. The data growth rate is exponential and for just one database, it grew from 50 TBs to more than 650 TBs between 2008-2014 (NASA's infrared science archive database; see Fig. 1.1). This number will quickly get larger. The demand on high performance supercomputing increases rapidly. And the picture gets even more dramatic if we add another aspect of growing need of the computer resources, that comes from large computer simulations.

A good solution to the problem, that is being developed since 2002, is the creation of the Astronomical Virtual Observatory. The Astronomical Virtual Observatory is the global solution for handling the ever-growing observational data in a user-friendly environment. The first step in achieving this goal, is to standardise the data from different telescopes and databases so that it can be processed equally. Tools for data handling, pro-

---

[3]More on ESO's instruments at `http://www.eso.org/public/teles-instr/`
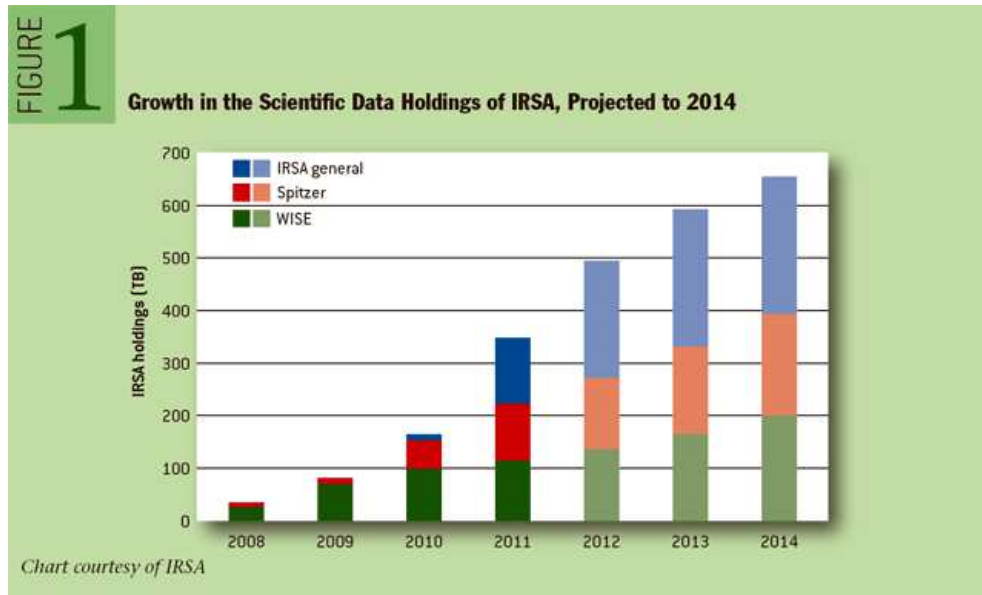
Figure 1.1: The observational database growth rate for 2008-2014 on the example of the infrared science archive (IRSA, NASA). IRSA is responsible to accumulate data from Spitzer, WISE, Herschel, Planck, 2MASS, IRAS, COSMOS, BLAST, etc. Although some of these telescopes stopped delivering data already, others are still actively filling up the space; growing with an impressive rate. (Histogram from: `http://queue.acm.org/detail.cfm?id=2047483`)

cessing and retrieving final results, have been developed continuously and great progress in this direction has been achieved. There are various software packages available that can be used for different tasks both within the global VO framework, and in single-user mode. Examples are the ALADIN code that allows to query the object in all VO databases and retrieve photometry or spectroscopy from all ground-based and space observatories as well as simply load local files, make astrometric, photometric or spectroscopic measurements of various sort. SPLAT (spectral analysis tool) allows to retrieve all spectral information about the object, collect it together, analyse it in the database and download the processed spectrum in a form that is ready to be published. TOPCAT (tool for operations on catalogues and tables) is an interactive software for handling the data catalogues, VOSED (a virtual observatory tool to build and analyse SEDs (Gutiérrez et al. 2011)) to retrieve the spectral energy distribution of a given astronomical object and many more.

1.3   Modern Cosmology in a nutshell

Let us take a step back and continue our brief journey through the history of astronomy, which is impressive and very interesting. From Egyptian priests that have been immensely powerful with their knowledge of astronomy to Greek philosophers that first attempted to create a complete model of the universe to the middle-ages, when scien-

tists were fighting church dogmatics, it is one giant book of discoveries and milestones that human civilisation reached to come to the digital era of ground-based and space observatories and to accelerate the progress even further. It is a long story to tell, but one always has to cut it short for one reason or another. I will begin from the early XX century, which marks the start of the modern cosmology era.
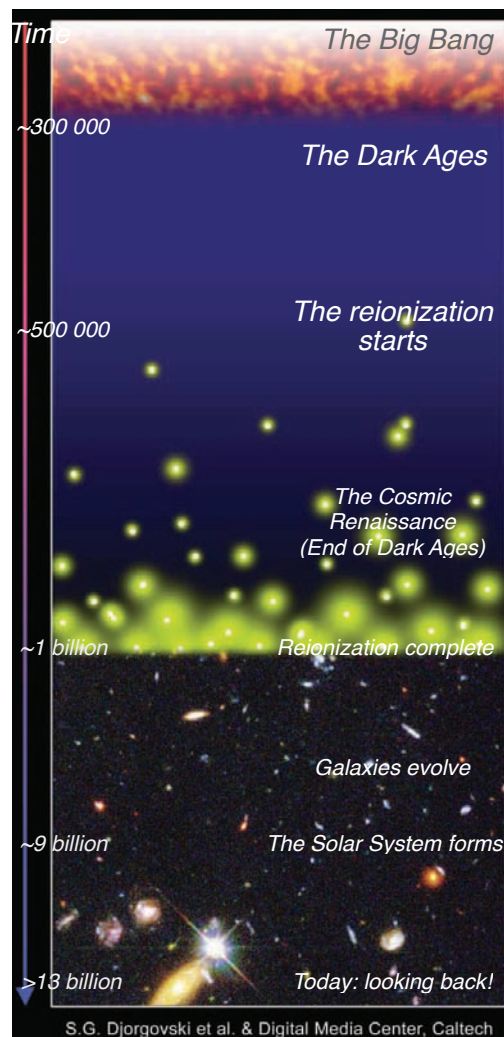
Figure 1.2: The Cosmic Evolution sketch by S. G. Djorgovski et al. & Digital Media Center, Caltech (`http://www.astro.caltech.edu/~george/reion/`)

Our understanding of the evolution of the universe from its beginnings to the present days is represented in Fig. 1.2. A large majority of scientists agree today that our universe as we know it experienced a Big Bang about 13.8 Gyr ago. Although the name leaves room for wrong interpretations. As Peebles et al. (1991) stated in their review article,

"The name, Big Bang, is unfortunate because it may be misunderstood as referring to an event in a singular start of expansion of the universe. Whatever started the expansion, perhaps an inflationary epoch, perhaps something even more wild, is not intrinsic to the standard model." However this is the term that is widely used in modern Cosmology and let us follow the tradition.

The very early universe, up to 10^{-43} seconds after the Big Bang, is the subject of extremely speculative ideas on how it came into existence. It is widely accepted (but of course still debated) that the universe then entered an inflation epoch, in which it expanded violently (or more precisely exponentially) and increased its scale length by many orders of magnitude (Baumann 2009).

At the end of cosmic inflation, the universe was filled with an extremely hot and dense plasma of elementary particles, opaque to electromagnetic radiation. As the universe expanded, it cooled down allowing the formation of bound states of particles. At first the quarks and gluons, which made up the primordial plasma, combined into hadrons (protons and neutrons), which in turn combined into light atomic nuclei during the Big Bang nucleosysthesis (Baumann 2009; Ryden 2003).

About 380.000 years after the Big Bang the temperature of the universe fell below 3000 K, and ions and electrons in the plasma combined to form atoms of neutral hydrogen and helium. This is known as the epoch of recombination. As a consequence of recombination, photons decoupled from matter and could travel freely through the universe. The relic of this era can be observed as the cosmic microwave background radiation (CMB) at a redshift of z=1100 (Baumann 2009; Ryden 2003).

1.3.1   STRUCTURE AND COMPOSITION OF THE UNIVERSE

The Universe is homogeneous and isotropic on large scales obeying the so-called cosmological principle (Cervantes-Cota & Smoot 2011). A. Friedmann in 1922 used Einstein's field equations to derive a mathematical model of how the homogeneous and isotropic Universe would expand or contract (Friedmann 1922; Ryden 2003). The same model has been independently derived by four different scientists in different years. These were: A. Friedmann, G. Lemaître, H. Robertson and A. Walker (Friedmann 1922; Lemaître 1931; Robertson 1935; Walker 1937). The line element in FRW (Friedmann, Robertson, Walker) metric is expressed with the following equation:

$$ds^2 = -dt^2 + a^2(t)\left[\frac{dr^2}{1 - kr^2} + r^2(d\theta^2 + sin^2\theta d\phi^2)\right] \tag{1.1}$$

where t is the cosmic time, r, θ and ϕ are the elements of the polar coordinates, k is the curvature that can be $k = 0$, or ± 1 corresponding to the flat, closed or open Universe (see Fig.1.3); $a(t)$ is the scale factor in the metric that contains all the temporal evolution. In order to find the temporal evolution of the scale factor, $a(t)$, one uses the valid theory for gravity, which is General Relativity (GR). The solution can be obtained from the Einstein-Hilbert Lagrangian (Cervantes-Cota & Smoot 2011):

$$\mathcal{L} = \frac{1}{16\pi G}(R + L_m)\sqrt{-g} \tag{1.2}$$

where R and G are the Ricci scalar and the Newton constant respectively and $g = |g_{\mu\nu}|$ is the determinant of the metric tensor. Performing variation to the eq.1.2 one obtains Einstein's field equations:

$$R_{\mu\nu} - \frac{1}{2}Rg_{\mu\nu} = 8\pi G T_{\mu\nu} \tag{1.3}$$

where $T_{\mu\nu} \equiv -\frac{2}{\sqrt{-g}}\frac{\partial L_m \sqrt{-g}}{\partial g^{\mu\nu}}$ is the stress energy-momentum tensor.

The GR cosmological field equations in the FRW metric Have following form (Cervantes-Cota & Smoot 2011):

$$H^2 \equiv \left(\frac{\dot{a}}{a}\right)^2 = \frac{8\pi G}{3}\rho - \frac{k}{a^2} \tag{1.4}$$

and

$$\frac{\ddot{a}}{a} = -\frac{4\pi G}{3}(\rho + 3p) \tag{1.5}$$

where H is the *Hubble parameter*, a is the scale factor of the Universe, ρ and p are the density and pressure of the perfect fluid. The dots represent the time-derivatives. As mentioned k characterizes the curvature of the space-time (Cervantes-Cota & Smoot 2011; Ryden 2003). If we take into account all relativistic effects of the Universe, the Friedmann equations for the entire matter and radiation in the Universe, can be written in the following form

$$\Omega = \Omega_R + \Omega_M + \Omega_\Lambda = 1 + \frac{k}{a^2 H^2} \tag{1.6}$$

Here Ω_R represents the radiation component dominated by the CMB (very small at present, 5×10^{-5}); $\Omega_M \equiv \frac{8\pi G \rho_m}{3H^2}$ characterizes the matter content and the $\Omega_\Lambda \equiv \frac{\Lambda}{3H^2}$ is the cosmological constant parameter characterizing the dark energy content of the Universe (Cervantes-Cota & Smoot 2011).

The cosmological constant was first introduced by A.Einstein in his equations of General Relativity (Einstein 1915) in order to allow for a static solution. In 1998 it came back and now characterizes the accelerated expansion of the Universe.

There are few ways of testing the accelerated expansion of the Universe (and thus the existence of so-called dark energy content that has the largest ($\sim 70\%$) contribution into the matter-radiation content and is responsible for the accelerated expansion). The current "Dark Energy Survey Mission" (DES[4]) is probing the Dark Energy content of the Universe with four different methods. Namely, using:

1) Type Ia Supernovae (SN) - In 1998-1999 two independent groups of astronomers lead by Saul Perlmutter, Brian Schmidt and Adam Riess, published articles

---

[4]http://www.darkenergysurvey.org/science/

about the accelerated expansion of the Universe using SN Ia as standard(izable) candles (Riess et al. 1998; Perlmutter et al. 1999). Their work was awarded with the Nobel Prize in 2011.

Currently, DES is studying the spectra of ~ 3000 SN host galaxies, which will help to make redshift-magnitude relation acquire more accurate values than available at present.

2) Baryon Acoustic Oscillations (BAO) - studying Baryon Acoustic Oscillations is another way of tracing the Dark Energy content in the Universe (Seo & Eisenstein 2003). As SNe are considered to be standard candles in astronomy, so are the BAOs the standard rulers, allowing to measure the properties of the Universe at different cosmological redshifts. The aim of DES is to determine the angular sizes of the oscillations at different redshifts.

3) Galaxy Clusters (GC) Counting the galaxy clusters at different redshifts is yet another way of probing the Dark Energy (Mohr et al. 2003). The idea is to see how the structure formation changes across the Universe's history. The Dark Energy is responsible for the expansion of the Universe, therefore it affects the evolution of the structure in it and also the formation of the galaxy clusters depends on the interplay between the gravity and the dark energy.

DES will combine observational material and the computer simulations to measure the galaxy cluster masses and test the influence of the dark energy on the evolution of the galaxy clusters with the Universe.

4) Weak Gravitational Lensing(WL) Studying the influence of the gravity on the objects in the universe is another way of probing the nature of the dark energy (Melchior et al. 2015). Analyzing the large scale structure formation and evolution through cosmic time is one of the best ways to probe the relation between dark energy and the gravity and the effects of weak lensing are good tools to test the cosmic shear.

DES will create the catalogue of about 300 million galaxies that experience weak lensing studying the influence of the dark component upon the evolution of the structure (more can be read on the DES webpage in the footnote and in the cited articles).

It can be easily noticed that the values of Ω (density parameter) in Eq. 1.6 can cause the curvature (k) value to vary. Namely, when $\Omega > 1$, then $k > 0$, characterizing the positively curved (closed) Universe; when $\Omega < 1$, $k < 0$, characterizing the negatively curved (open) Univserse and obviously, the case when $\Omega = 1$ the curvature has a critical value $k = 0$. Fig. 1.3 is a good graphical representation of how the Universe with different curvatures looks like and what happens to the structures and distances between them in different cases.

The CMB measurements suggest that the energy, matter and radiation content of the Universe is distributed in following fractions: Dark Energy - $\sim 68\%$, Dark Matter - $\sim 27\%$ and only $\sim 5\%$ of the matter is in the baryonic form - anything that we can observe nowadays (Planck Collaboration et al. 2014).

We can define the redshift (z) here as a measure of the expansion of the Universe:

$$1 + z = \frac{a_0}{a(t)} \tag{1.7}$$
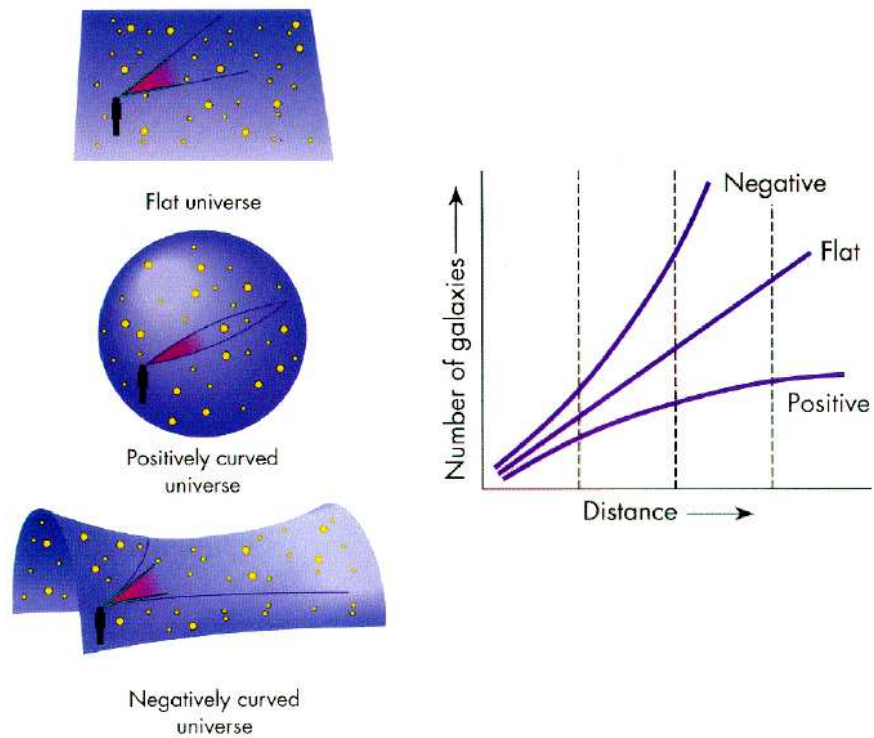
Figure 1.3: The graphical view of the Universe with different curvatures corresponding to different k values $k = \pm 1$ corresponds to the positively and negatively curved space-time (closed and open Universe) and $k = 0$ is the case of the flat Universe. Source: `http://abyss.uoregon.edu/~js/images/curvature.gif`
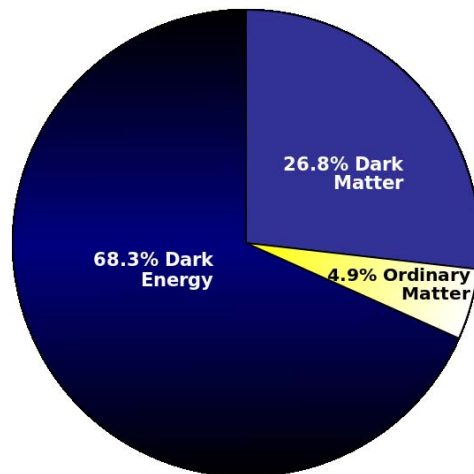
Figure 1.4: The composition of the Universe as by the latest results from Planck Collaboration et al. (2014): the dark energy is responsible of about 68.3% of the total composition of the Universe; the contribution of the dark matter is about 26.8% and baryonic content (stars, galaxies, interstellar and intergalactic gas, dust etc. is about 4.9%. Photo source: `http://pics-about.space/dark-matter-dark-energy-vs?p=2`).

where a_0 is a scale factor at present and is set to unity; consequently, at present, $z_0 = 0$ and further we look into the past of the Universe, the value of redshift grows.

Observationally, redshift can be obtained using emission or absorption lines in the spectra of objects and has a form:

$$1 + z = \frac{\lambda_{obs}}{\lambda_{em}} \tag{1.8}$$

where λ_{obs} and λ_{em} are the observed and intrinsic wavelengths of the emission/absorption line, accordingly.

1.3.2 The discovery of the Hubble law

For this thesis there are some other people that we have to also mention: Edwin Hubble is definitely among them. We can name him as the most important figure, who made astronomy do one gigantic jump into understanding the universe in which we live.

One of the major findings that Edwin Hubble is credited with is the discovery of the nature of "extragalactic nebulae". In the early 1920es Hubble was observing the M31 and M33 nebulae and managed to identify some Cepheid variable stars inside them. Determining the distances using Cepheids as standard candles was already an established method, which was first implemented by Henrietta Swan Leawitt. This helped Hubble to measure the distances to those Cepheids. Some of the results were surprising for they appeared to be a behemoth number of the order of 300 kpc (Hubble 1925). Hubble
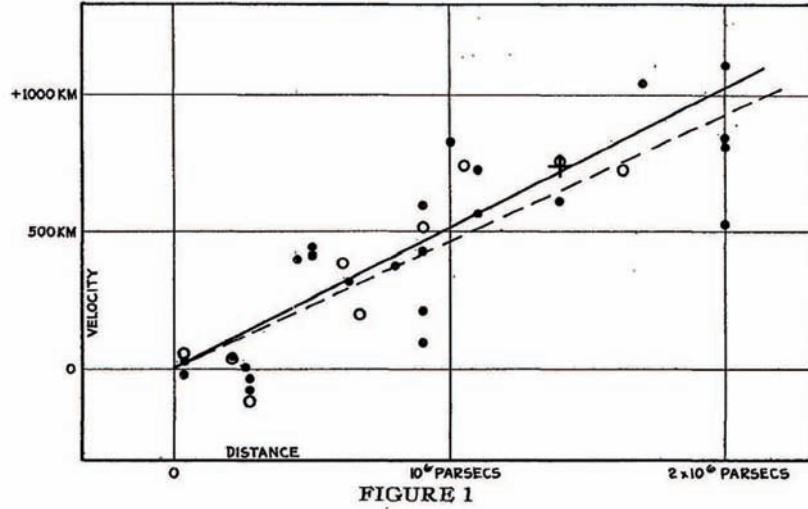
Figure 1.5: Hubble's discovery of the expanding universe (Hubble 1929). Just like it was believed in early centuries that the stars were pinned to the sky with some magic nails, so was it believed before Hubble that the universe was static and unchanging. Even the great Albert Einstein did believe static state of the universe. This discovery though, brought us to new level; to the era of Cosmology.

concluded that some nebulae in the Messier catalogue hence did not belong to our galaxy. He named these objects "extragalactic nebulae".

In the following years, he has been investigating the spiral and diffuse extragalactic nebulae (galaxies). This investigation has been followed by the classification of the nebulae into elliptical, spiral and irregular types (Hubble 1926). However, Hubble's valuable work did not stop here. He continued deriving properties of galaxies. Matching the velocities (mainly measured by Vesto Slipher) and distances to nebulae he came to the discovery that revolutionised our understanding of the universe. Edwin Hubble found that most of the galaxies were receding from Milky Way and the recession speed increased with the distance (Hubble 1929). This can be summarised in the following formula:

$$v = H_0 \times r \tag{1.9}$$

where H_0 is called a Hubble parameter and according to the latest measurement (Planck Collaboration et al. 2014) is equal to $H_0 = (67.3 \pm 1.2)$km s^{-1} Mpc^{-1} and r is the distance to the galaxy.

1.4 GALAXIES

After the recombination epoch, the universe entered a period known as the "dark ages". It was filled with a relatively homogeneous distribution of matter with very small deviations and residing in the deep darkness. Slowly, the overdense areas started to collapse under the effect of gravity, giving birth, after about 150 million years, to the first stars and

quasars (Natarajan & Yoshida 2014; Ryden 2003). The radiation emitted by these newly formed structures ended the dark ages and the reionization era begun. Observations of the Ly-α forest of quasars show that the epoch of reionization happened at $z > 6$ (Songaila 2004).

But our picture of the evolution of the universe, is far from being complete and so detection and study of the primordial galaxies will help us understand when galaxy formation started, reionization happened and the dark ages ended.

As stated above, galaxies bring to light a significant part of the baryonic content of the universe. And therefore, we can observe and study them. In the past two decades, a flood of new data in all wavelength ranges, revealed the hidden mysteries of galaxy formation and evolution. From powerful hot UV content to cold dust-obscured star-formation in the IR, we are now able to determine some very important properties of galaxies at different redshifts (e.g. star formation rates, stellar masses, metallicities, etc). These properties allow us to understand how our universe evolved from its early stages until now and what processes it and its resident galaxies have undergone. But not all the mysteries are solved yet. Some of the major questions for cosmologists to answer nowadays are why structures such as galaxies exist in the universe at all? How and when exactly do these huge stellar nurseries form and evolve? Modern telescopes and deep sky surveys together with future facilities like e.g., the James Webb Space Telescope (JWST), the European Extremely Large Telescope (E-ELT) and the EUCLID mission are expected to deliver very detailed answers to these (and many more) questions.

1.4.1 Classification of galaxies

Edwin Hubble not only discovered galaxies, but also was the first to classify them into a morphological system, basis of which is actively used also today though obviously, with some modifications (Hubble 1936). Hubble's classification, so-called Hubble Tuning Fork, of the galaxies is presented on Fig.1.6. He divided galaxies into the distinct groups according to their appearance. Namely, the galaxies that resembled ellipses of different eccentricity from almost circular to the extended ones without any morphological additions followed by two different types of spiral galaxies - with and without distinctive bulges ending with the types, which were not fitting elsewhere and were named irregulars (Hubble 1936; Longair 2008).

The revised Hubble sequence for galaxies

With progress in observational facilities, obviously, galaxy classification significantly changed too. Hubble, in his works was classifying only the brightest galaxies, whilst with the new telescopes, new types of galaxies have been discovered having different morphological and luminosity properties. For example, the Seyfert galaxies, radio galaxies, starbursts, etc. Most of them contain an active galactic nuclei. Let us briefly summarize the modern classification of galaxies and what we know about them at present.

Elliptical galaxies do not show any additional structural features to the elliptical
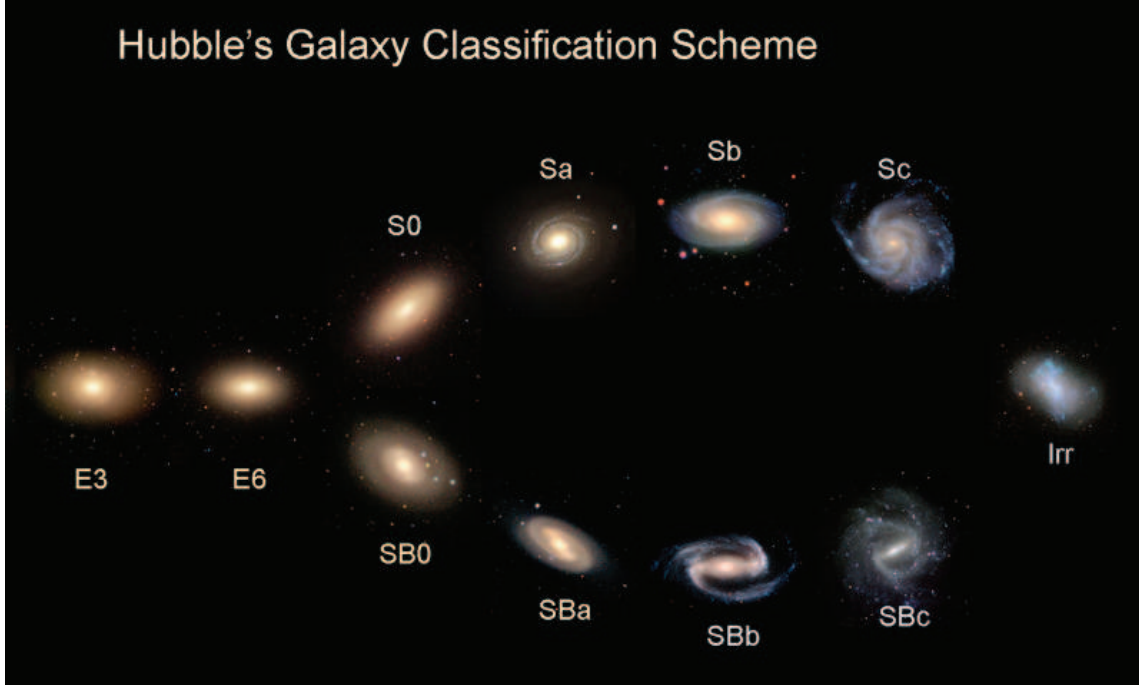
Figure 1.6: The Hubble Tuning Fork diagram (Hubble 1936). In this diagram, Hubble arranged galaxies in three groups - ellipticals, spirals and irregulars. Ellipticals with different ellipticities were placed on the diagram from galaxies with almost spherical shapes to extended elliptical shapes with increasing eccentricities. The spiral galaxies he divided into two groups - normal and barred spirals and at the end of the diagram, he placed galaxies with more chaotic shapes that would not fit into ellipticals or spirals, under the irregular subgroup.

shapes. They come in different sizes and ellipticities and vary between the most luminous galaxies known so far, ($M_B \approx -24$) to the dwarf ellipticals (dE) (Longair 2008). The surface brightness profile for elliptical galaxies has been first obtained by de Vacouleurs as a $r^{1/4}$ law (de Vaucouleurs 1948; Longair 2008):

$$log_{10}\left[\frac{I(r)}{I(r_e)}\right] = -3.3307\left[\left(\frac{r}{r_e}\right)^{1/4} - 1\right] \tag{1.10}$$

where r_e is the half-radius of the total luminosity emitted by the galaxy and $I(r_e)$ is the surface brightness at that radius. The luminosity for the entire surface of the elliptical galaxy can then be calculated using:

$$L = 7.215\pi I_e r_e^2\left(\frac{b}{a}\right) \tag{1.11}$$

Here b/a is the ratio of the major and minor axes of the elliptical galaxy.

Spiral galaxies are characterized by their spiral-like structure, emerging from the central bulge. Hubble divided spiral galaxies into two types: "normal" and "barred" spirals (see Fig. 1.6). In the "normal" spirals, the arms emerge directly from the central

bulge instead, in the "barred" spirals the bulge is extended into a bar-like structure. Both, "normal" and "barred" spiral galaxies can be divided into three sub-groups: S(B)a[5] - spirals with tightly wound arms that do not resolve into individual stars (Longair 2008), S(B)b - type spirals have a little bit more open arms that can be resolved into stars and the central bulge is smaller than that in the S(B)a spirals. S(B)c type spirals that can be decomposed into stars, stellar clusters and molecular clouds. In modified classification, the sub-classes extend to include also the galaxies with more chaotic structures.

Lenticular galaxies - (lens-like galaxies) are those that show distinct disk-like component and very smooth light distribution. Lenticulars are close to the spiral galaxies - their structure shows a clear central bulge and are also close to the ellipticals by properties (Longair 2008).

The light distribution for all types of galaxies that can be decomposed into the central bulge and other components (spiral and lenticular galaxies) can be expressed with the following formula:

$$I(r) = I_0 e^{-\frac{r}{h}} \tag{1.12}$$

where h is the scale length of the disc of a galaxy (in the order of 3kpc). I_0 is the central surface brightness. The total luminosity can be calculated using the expression:

$$L = 4\pi h^2 I_0 \tag{1.13}$$

A more general form of the luminosity function has been proposed later by Sérsic (1963) and has a form:

$$log_{10}\left[\frac{I(r)}{I(r_e)}\right] = -b_n\left[\left(\frac{r}{r_e}\right)^{1/n} - 1\right] \tag{1.14}$$

Irregular galaxies - everything that was lacking symmetry and structure, Hubble unified into the irregular galaxy types. The irregular galaxies were those that looked very similar to the Milky Way satellite Large and Small Magellanic Clouds.

De Vaucouleurs revised Hubble sequence into the classification scheme that allows a smooth transition between galaxies of different types from ellipticals to lenticulars and further to spirals and irregulars (de Vaucouleurs 1974).

Nowadays, as we manage to discover galaxies at great distances (with large redshifts), we see that most of these morphological features break down as we advance in looking into the past of the Universe and it is better to characterize galaxies according to the properties different from their morphology. One way to characterize galaxies is to divide them into the blue and red sequences. The red sequence consists of non-star-forming, high-mass spheroidal galaxies that are "red and dead". The blue sequence, on the other hand, consists of actively star-forming, low mass galaxies (Longair 2008).

---

[5]"B" - corresponds to the "barred" spiral galaxy types

The above-described classification of galaxies can be made studying their multiband luminosity characteristics. We now can proceed to introduce different methods of detection and study of galaxies.

1.4.2 PHOTOMETRY OR SPECTROSCOPY? BOTH!

In order to study galaxies in different epochs in the Universe, we need to find a way to first detect them at different redshifts and then study their nature. How do we do this? What are the methods and tools that we can use? And what is it that we are looking for?

Accurately measuring distances to galaxies is vital because it allows us to correctly locate them into the space-time. Correctly located galaxies, on the other hand, allow us to know what is the true relation between different galaxy populations and how galaxies form and evolve at different stages in the evolution of the universe. Knowing the answers to these questions, then allows us to reconstruct its history and resolve the quest of the formation and evolution of the universe itself.

The baryonic content of the universe, trapped into stars, interstellar and intergalactic media, consists of different chemical elements. The most abundant of these elements are hydrogen and helium, with the former making up about 74% of the entire chemical composition of the universe and the latter about 24%. Therefore, once decided to hunt for the early galaxies, one has to look for the hydrogen in emission or absorption at high redshift.

There are two main ways of recording the light from galaxies: spectroscopy and photometry. Spectroscopic measurements allow to study in detail the light from an object. Photometric ones on the other hand, is a measure of the flux in a given wavelength interval typically defined by a filter.

Spectroscopic observations of galaxies are very precise, and allow us to measure redshifts with very high accuracy ($\lesssim 1\%$ depending on the resolution). It is a way of detecting and studying chemical composition and dynamical properties of galaxies. For galaxies at high redshifts acquiring spectroscopic data can become very difficult due to the faintness of the sources. These objects are very faint and they either remain undetected or require enormous integration time to get out spectra with good enough signal-to-noise ratio (S/N) to establish robust conclusions.

The photometric redshift method comes to aid in this case. Unlike spectroscopy, photometry does not require enormously long exposure times and it is possible to obtain data in multiple bands simultaneously, which helps in constructing spectral energy distributions of galaxies and in obtaining their physical properties. Photometry has become one of the main alternative tools to spectroscopy. Having multi-wavelength data and reconstructing the spectral energy distribution (SED) of the galaxy from the existing synthetic spectra, allows us to derive the redshift and some other properties of galaxies with good enough accuracy to be used as a good substitution to spectra. Also, photometry probes a much deeper magnitude depth compared to the one reached by spectroscopy.

It is a very fast and reliable method but the price to pay is a much lower precision in the determination of redshifts, namely $\sim 3 - 10\%$ accuracy depending on the number of wavebands used (Oyaizu et al. 2008; Mo et al. 2010).

Once an object has been selected as a candidate for being a high redshift galaxy through a (robust) photometric determination of its redshift, spectroscopic follow-up measurements are performed. However, the photometric redshift method being less accurate than spectroscopy, can be a source of confusion. Therefore one has to be really careful when deriving redshifts through photometry.

Combining these two methods, one can obtain precise redshifts and dynamical properties of galaxies, and also reconstruct some physical quantities, among these SFRs, stellar masses, dust extinction. This way one can obtain a detailed knowledge of the history of the universe both from the individual galaxy properties point of view and from the point of view of statistical analysis of galaxy populations.

1.4.3   SED FITTING CODES

Good progress has been made in recent years in implementing complex SED fitting codes, which allow us to obtain robust SED fits for galaxies at different redshifts. The various software packages available have the same basic concept: they contain theoretical "ingredients" that mix and match with the obtained multiband fluxes to get out the best-fit SEDs and some of the physical parameters of the galaxy. In Fig. 1.7 we give a schematic view of how one of the SED fitting codes (Hyper-Z, by Bolzonella et al. (2000)) works.

The method is based on the identification of the strong spectral breaks, such as the Balmer break (4000 Å) and the Lyman break (912 Å) in the spectrum of the galaxy. Matching the model spectra and input multiband fluxes. Since the actual information that we have to input in the code is photometry, in order to obtain reliable results, it is better to have fluxes from as many broadband ranges as possible, making it easier for the code to find the best SED fit of a galaxy. The fitting is made using the standard χ^2 minimisation approach. The best-fit spectrum is selected according to the χ^2 formula:

$$\chi^2(z) = \sum_{i=1}^{N_{\text{filters}}} \left[\frac{F_{\text{obs},i} - b F_{\text{temp},i}(z)}{\sigma_i} \right]^2 , \tag{1.15}$$

where N_{filters} is the number of used filters. F_{obs} and F_{temp} are the observed and template fluxes respectively, σ is the flux uncertainty and b is a normalisation parameter (Bolzonella et al. 2000; Arnouts et al. 1999; Ilbert et al. 2006).

Now a little more details about above-stated SED-fitting "ingredients".

Template spectra

Template spectra can be of two types: observed SEDs or synthetic models. Out of the observed SEDs, the Coleman, Wu & Weedman (Coleman et al. 1980) is one of the most used set of spectra. They combine data of different morphological types of galaxies and
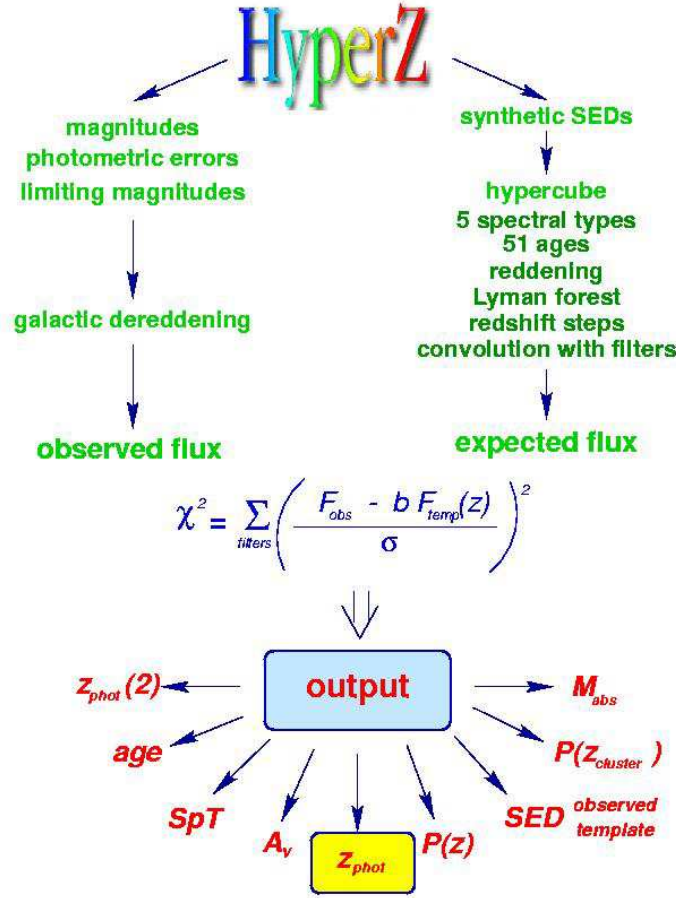
Figure 1.7: The schematic view of the SED fitting code, Hyper-Z (Bolzonella et al. 2000) and how it is functioning. The code matches the input photometric data with the synthetic SED models and picks the one that has minimum χ^2 match with the observed magnitudes and gives the output SED fit and physical parameters like e.g., M_*, SFR, photometric redshift, age, E(B-V), etc.

apply the corrections corresponding to different redshifts. E.g. K-corrections, assumed colour-redshift and magnitude-redshift relations, etc. The alternative to the observational SED templates, are the synthetic spectral libraries. There are different sets available among these, PEGASE (Fioc & Rocca-Volmerange 1999), BC03 (Bruzual & Charlot 2003), CWW (Coleman et al. 1980).

The most complete and widely used set of synthetic spectra is that of Bruzual & Charlot (2003). This template combines simulated spectra of galaxies with wide range of masses and metallicities and different morphological types. The templates are constructed on the basis of Padova and Geneva stellar tracks (Girardi et al. 2000; Lejeune & Schaerer 2001).

Initial Mass Function

The initial mass function (IMF) characterises the mass function for a new born population of stars (i.e. before any of the stars have departed from the main sequence or lost mass in other ways). The IMF was first introduced in (Salpeter 1955), where it was assumed to be a power law distribution of the type:

$$\xi(M) = cM^{-(1+x)}, \tag{1.16}$$

where x is the slope and c is a normalisation constant. Stellar evolution theory and a prescription for the star-formation history is then required to account for the stellar content of a model galaxy and its evolution in time. Of course, this characterization is far from trivial since the colour of a galaxy can be influenced by different properties and the outcome can be very similar in different cases; e.g. a red colour of a galaxy can be induced by the old stellar population, or the cold, re-heated dust that emits radiation in the IR part of the spectrum. When studying galaxies in the close neighbourhood, we can resolve stars or stellar clusters inside them and therefore discriminate between the different origins mentioned above, but when studying early galaxies (i.e. galaxies that are at high redshifts and are very distant from us), the only information available comes from the integrated flux of the entire system, which of course, makes it impossible to judge properly, and one has to make assumptions of various sort. However, these assumptions are the only way (and quite a good way at present) to study the formation and evolution of galaxies and derive crucial hints for understanding them.

There has been significant improvements in obtaining more accurate IMF for SED fitting since 1955. The Salpeter IMF tends to overrepresent less massive stars, underestimating the contribution from massive stars. Various other authors published their works on improving the IMF estimates trying to include the contribution not only from massive, but also from less massive, old stars (Miller & Scalo 1979; Kroupa 2001; Chabrier 2003).

The form of the IMF that is most widely used in SED fitting templates, is the one by Chabrier (2003). The model includes effects from all star types. However there are of course concerns about the universality of the IMF. One cannot assume the same initial values for all galaxy types across the entire galaxy formation and evolution history. Another point that one has to take into account is that the IMF only includes the contribution from the baryonic part of the matter, the influence of the dark matter, remains not very well-known.

Gas and dust

Other important components in galaxies are gas and dust. The two play a vital role in understanding not only the galaxy structure, but the way emission and absorption features of the galaxies are influenced by different types of atoms and molecules surrounding them. Contribution from the interstellar gas of different temperature is included into the SED fitting codes.

Gas in galaxies can be in different forms and therefore can be traced differently. It can be in the hot ionized, warm molecular, warm neutral or cold atomic forms. Characteristic temperatures may vary between $\sim 10^4 - 10^5 K$ (Anderson et al. 2009; Kennicutt & Evans 2012) for hot environments to several thousands down to $\sim 10 K$. The hot gas formation mechanism is believed to be following: atmospheres of hot O and B type stars release the ionizing photons that heat up the cool interstellar gas (HII regions). Another significant input into reheating interstellar gas can come from supernovae (SNe). SNe explosions eject enormous amount of material in the interstellar medium (ISM) creating massive shock waves that heat up the interstellar gas up to $\sim 10^6 K$.

The warm gas is in the molecular or neutral form. The most frequent molecules are H_2, CO and OH. As H_2 cannot be observed in emission as it does not have a dipole moment, the easiest to detect is the CO because of its strong emission lines that are easy to observe. As for the neutral gas in the ISM, it can be traced by 21cm emission of the hyperfine atomic hydrogen spin flip transition and is one of the most interesting and important to map throughout the entire cosmic history, because of the long lifetime ($\sim 10^7 yr$, Furlanetto et al. (2006)) and therefore the best way to trace the "dark ages" of the universe. The 21cm emission is widely used to map the structure of the Galaxy.

The origin of dust in the interstellar medium, is not precisely known. However the dust content in the local galaxies has been studied in detail, and good dust-extinction models have been developed to explain the nature and the contribution from the dust in galaxies. This work is based on the Calzetti et al. (2000) extinction law. The Calzetti et al. (2000) work is based on studying far infrared (FIR) properties of 40 starburst galaxies; the authors carefully study the temperature and properties of the dust in these starbursts. These results are then included in the SED-fitting codes as a model for the dust extinction.

Star Formation Rate

The star formation rate (SFR) characterises the transformation of the interstellar gas and dust into stars per unit time. As a matter of fact, SFR is impossible to obtain observationally; the only way is to infer it from the available observables. Fluxes from different spectral range, can be converted into the star formation rate estimates (a central review on this approach is Kennicutt (1998)). Below I will briefly review some of the SFR estimates (Calzetti 2013).

UV light: characterises the contribution from massive, hot O and B type stars in the galaxy. The UV indicator constants may vary depending on the used assumptions on IMF, template SED and star formation history. But overall, it has the following form:

$$\text{SFR(UV)} = 3.0 \cdot 10^{-47} \lambda L(\lambda),^6 \tag{1.17}$$

IR flux: the contribution to IR emission comes from the heated dust. It emits

---

[6]here and elsewhere SFR is measured in $M_\odot/\text{yr}$, λ is the wavelength of the flux (converted into luminosity) in Å and L is the luminosity in erg/s

IR light across the entire infrared spectrum ranging from 5 to ~ 1000 μm. UV-heated dust produces the NIR radiation while the gas influenced by lower mass stars, can be traced with the long-wavelength IR emission. In order to derive SFR indicators from IR radiation, one has to take into account the entire contribution from IR spectral range. The IR estimates then has a following form:

$$\text{SFR(TIR)} = 2.8 \cdot 10^{-44} L(\text{TIR}),\tag{1.18}$$

where TIR stands for total infrared emission. $L(\text{TIR})$ is the total stellar luminosity absorbed and re-emitted by ISM.

Ionised gas and forbidden lines. Another SFR indicator is the emission coming from the ionised gas. The young stars in galaxies produce huge amount of energetic photons that ionise the interstellar gas; Hydrogen emission-lines are created in this way. The Hα line flux can be converted into the SFR in the following way:

$$\text{SFR(H}\alpha) = 5.5 \cdot 10^{-42} L(\text{H}\alpha).\tag{1.19}$$

Forbidden lines are good tracers of star formation in cases where Hα line is not available for some reason. The strongest forbidden line that can be used to trace the star formation is the [OII] line. The conversion, according to Kennicutt (1998) has the following form:

$$\text{SFR([OII])} = 1.4 \cdot 10^{-41} L(\text{[OII]}).\tag{1.20}$$

1.4.4 SOME FUNDAMENTAL RELATIONS FOR GALAXIES

Since the discovery of nebular rotation by Vesto Slipher (Slipher 1914; Sofue & Rubin 2001), efforts have been made to find correlation between different properties as for elliptical so for spiral "nebulae". Out of these efforts came some fundamental relations for different types of galaxies that can be used to study their evolution in different evolutionary epochs of the Universe and the evolution of the Universe itself. The "fundamental plane" and the "Tully-Fisher" relations are some of the first ones to mention that hold the clues about the evolution of elliptical and spiral galaxies in the nearby Universe.

Fundamental Plane

There have been extensive studies to find relation between different properties of elliptical galaxies, i.e. correlation between their luminosities, velocities, element abundances etc. (Longair 2008). There are two most important works that must be mentioned in this context. First one is the study by Faber & Jackson, who found the correlation between luminosity (L) and velocity dispersion (σ) for elliptical galaxies in the form of $L \propto \sigma^x$ with $x \propto 4$ (Longair 2008; Faber & Jackson 1976). Other studies found that $3 < x < 5$. This relation was allowing to measure the distance to the elliptical galaxy by measuring its flux density. Further advancing Faber-Jackson relation, Djorgovski & Davis (1987) introduced the "fundamental plane" relation, which lies in plotting the three-dimensional

relation between Luminosity (L), velocity dispersion (σ) and mean surface brightness of the elliptical galaxy (Σ). The relation can be found in various different forms in the literature; for example, it can be expressed in the following way:

$$L \propto \sigma^{8/3} \Sigma_e^{-3/5}. \tag{1.21}$$

Tully-Fisher Relation

In 1975, Tully and Fisher found the strong correlation between the width of the Hydrogen 21 cm line profiles and the intrinsic luminosities of spiral galaxies (Fisher & Tully 1975; Longair 2008) of the form:

$$L_B \propto \Delta V^\alpha \tag{1.22}$$

where L_B is the total luminosity of a spiral galaxy in the B-band, ΔV is the velocity width of the neutral hydrogen line and $\alpha = 2.5$. Tully-Fisher relation found to have even tighter correlation in infrared wavebands than in the visible (Longair 2008; Aaronson & Mould 1983). Thus, measuring 21 cm velocity and inferring absolute H band magnitude makes it possible to calculate the distance to the spiral galaxy.

With the progress in modern astronomy, we now manage to look deep into the past of the Universe and therefore, study galaxies at earlier stages of their evolution, therefore we need relations other than the ones described above, because these relations hold in the local Universe only. When probing galaxies with high redshift, we are aiming on finding relations between e.g. galaxy's mass and metallicity or mass and the star formation rate. Below I will briefly describe these two:

Mass-metallicity relation

The mass-metallicity relation is one of the most fundamental relations. The evolution of this relation with the redshift, on the other hand, gives hints on the galaxy formation and evolution picture and the physical processes happening inside the galaxies.

Metallicity can be obtained from the spectral lines of a galaxy. The ratio between the intensity of the line for a given metal (usually oxygen or iron, e.g. Kirby et al. (2013)) with the one of the hydrogen line is the desired quantity. The metallicities defined in this way are then plotted against stellar masses of galaxies. This gives the well-studied M_* vs. Z relation, shown in Fig. 1.8.

M_* vs SFR relation

Another very important relation is the one between the stellar mass and the star-formation rate of a galaxy. This relation is also one of the fundamental ones because it gives hints on the mass assembly process in galaxies and studying the evolution of this relation across redshift can help resolving the galaxy formation and evolution quest.
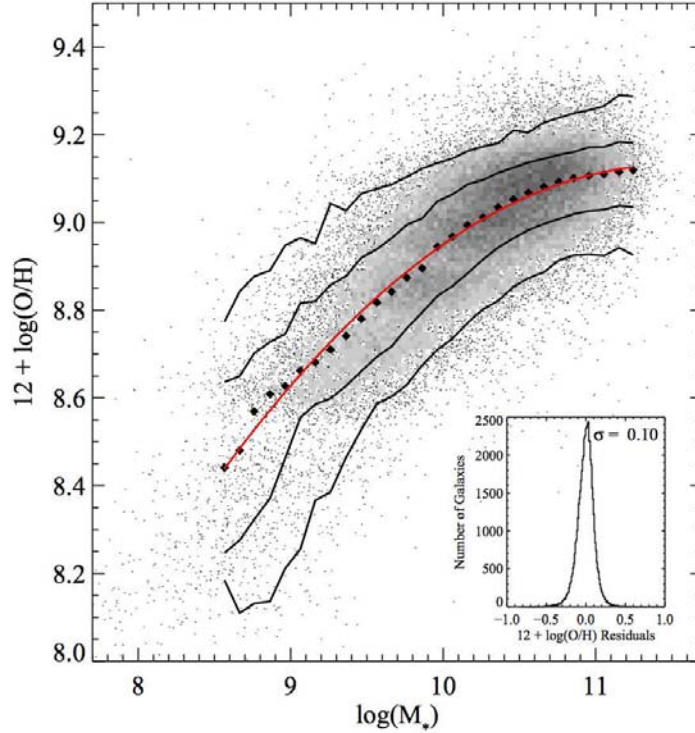
Figure 1.8: M_* vs Z relation for ~ 53400 star-forming galaxies (Tremonti et al. 2004). The big black dots represent the medians per mass bin. The red solid line is the polynomial fit to the data. The plot in the right lower corner presents the residuals of the fit.

The relation has a power law form, SFR $\propto M_*^\alpha$, where the slope, α, can vary depending on the sample selection method. According to the star-formation rate value per given mass, galaxies can be split into normal and starburst types.

Fig. 1.9 shows the M_* vs SFR relation by Rodighiero et al. (2011). As we can see, most of the galaxies form so-called "main sequence" of the relation. While there are galaxies that have exceedingly high star-formation rate (more than 1 dex higher than the SFR in the main-sequence galaxies). These are called starburst galaxies. It is very important to know what is the ratio between different types of galaxies and how they move from one phase to another.

In the right low corner of Fig. 1.9, the authors plot the specific star formation rate (sSFR), which measures the SFR per unit mass. The dashed and dotted lines mark the same SFR excess as in the main plot.

1.5   How we search is how we reach: young galaxies and how to find them

The selection of the galaxy sample on which to base an analysis is an integral part for obtaining valid and valued results on galaxy formation and evolution quest. There are
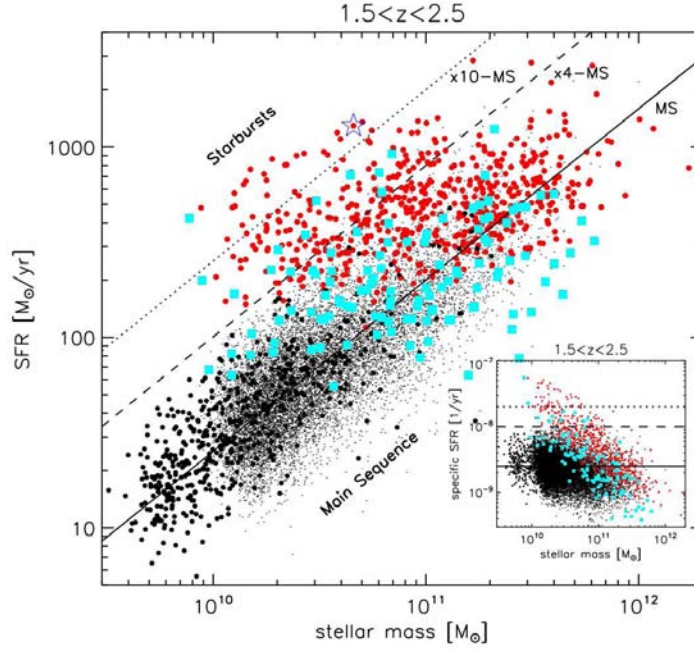
Figure 1.9: M_* vs SFR relation for galaxies in the redshift range $1.5 < z < 2.5$ (Rodighiero et al. 2011). The points of different colours represent galaxies from different samples (red dots and cyan squares are galaxies from "shallow" and deep PACS-GOODS South sample, big black dots are BzK GOODS galaxies and small black dots are BzK-COSMOS galaxies). The solid line marks the main-sequence of the M_* vs SFR relation; dashed and dotted lines mark the SFRs 4 and 10 times higher than MS. The blue star marks one of the most extreme starburst galaxy.

many different methods of targeting galaxies and building samples. Each of them has its pros and cons. Sample selection totally and completely depends on the scientific goal. Below I will briefly describe only some of the galaxy sample selection methods and the science behind them as an example focusing a bit more details on description of the method used in this thesis.

1.5.1 FLUX-LIMITED SAMPLES

IR selection

The infrared selection method traces luminous and very massive galaxies ($L_{IR} > 10^{11} L_\odot$; $M > 10^{10} M_\odot$). Galaxies selected with this method are called (ultra)luminous infrared galaxies (LIRGS and ULIRGS). Besides their characteristic powerful IR luminosity, these galaxies are very dusty, with on-going dust-obscured star formation. The rate of their star-formation is enormous. Studying galaxies with this method allows us to probe massive, extremely star-forming galaxies at low-to-intermediate redshifts. Morphologically, LIRGS and ULIRGS are compact ellipticals, spheroids or disk galaxies, found in single or merger states (Jacobs et al. 2011).

Lyman-Break Selection

This method aims at detecting galaxies by tracing their rest-frame UV light and therefore the Lyman-break in their spectra. Lyman-break galaxy (LBG) selection has been successfully used since the late 1990es, when Steidel & Hamilton (1993) first obtained photometric results for galaxies selected with their UGR colour, see Fig. 1.10. The extremely red colour in the $U - G$ plane and flat $G - R$ colour indicates the presence of the Lyman-break and therefore selects actively star-forming galaxies with few to no dust obscured processes inside them (the reason why we are looking for the powerful UV Lyman-break in the visible to near UV part of the spectrum is the high redshift of the candidate galaxy, which makes its spectrum being shifted to the above-stated bands. The bands may change depending on the redshift). According to Giavalisco (2002), in order to be a Lyman-break candidate, a galaxy should satisfy the following criteria (basically demanding that the object has a Lyman-limit break between the U_n and G bands):

$$(U_n - G) \geq 1 + (G - R); (G - R) \leq 1.2 \tag{1.23}$$
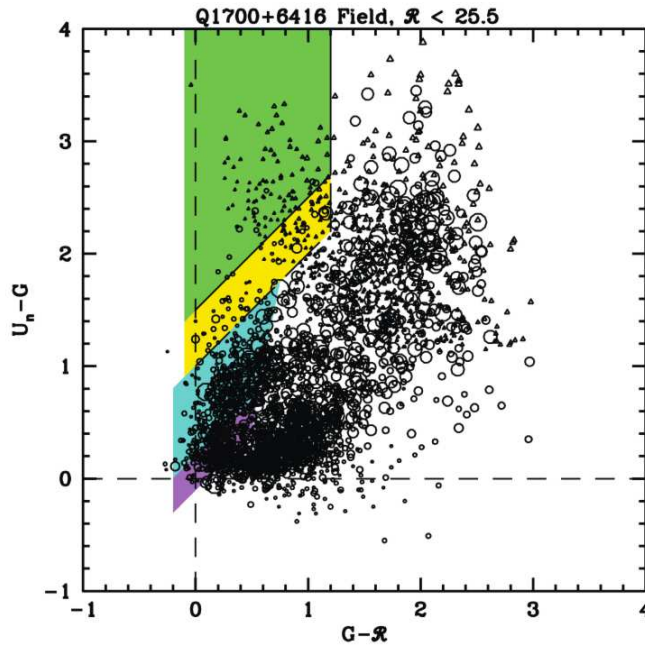
Figure 1.10: Lyman-break selection. Colour-colour diagram selecting LBGs (Giavalisco 2002). The open circles represent objects and they are scaled according to the angular size on the sky. The Open triangles are the cases, where only the limits of the $U_n - G$ colour has been derived. The cyan and magenta areas mark the selection of LBGs at $z \sim 3$ whereas the green and yellow areas mark the selection area of the LBGs at $z \sim 1.5 - 2$.

LBG selection method is a very good tracer of objects up to intermediate ($z \sim 2$ - Burgarella et al. (2011)) and high redshifts ($z \sim 6$ - Steidel et al. (1996); Vanzella
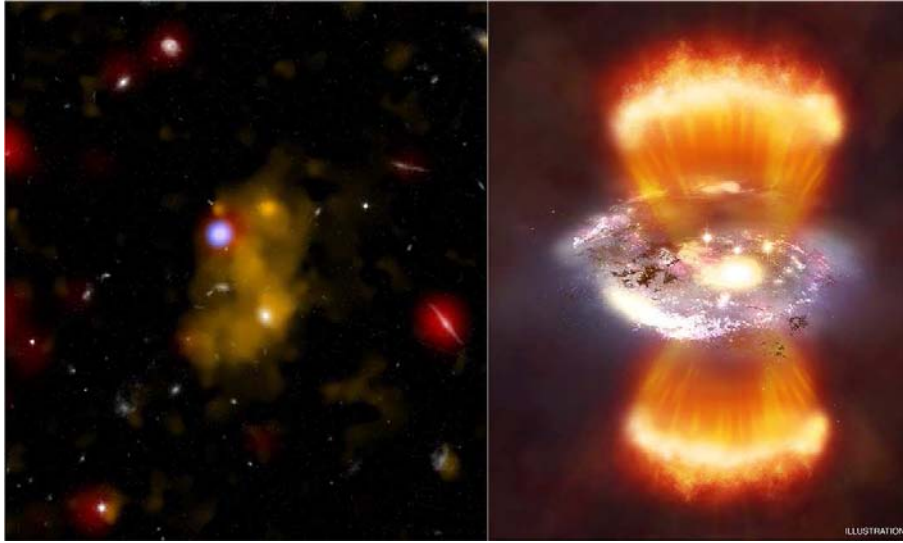
Figure 1.11: (Credit: Chandra X-Ray Observatory. Left: The giant Lyman-α blob $z \sim 3.1$ by Geach et al. (2009) and the artist's impression of the distant Lyman-α galaxy (right). `http://chandra.harvard.edu/photo/2009/labs/`)

et al. (2009)). Galaxies selected in this way, have bursty star formation and are usually very blue. Morphologically, they do not usually follow the Hubble scheme, but are more clumpy, extended or merging galaxies (Giavalisco 2002).

1.5.2 Narrow-band Selected Samples

High-redshift Lyman-α hunt

Partridge & Peebles (1967) predicted that the ionizing radiation in the early galaxies could possibly be found in the form of Lyman emission-series. Because of the high hydrogen abundance in the early universe and the fact that the Lyman series are the most energetic, they assumed that the strongest among the lines in the Lyman series, the Lyman-α line, would be the best traceable line.

This initiated the development of the narrow-band selection technique, which since then has become a very useful tool in the detection and study of galaxies at intermediate to very high redshifts. In fact, this method is very effective in the identification of galaxies at cosmic dawn. Being enormously far, it is almost impossible to trace any reasonable continuum emission from the first galaxies, and the narrow-band selection technique comes to rescue here. The method relies on comparing the flux in the narrow-transmission filter with its broad-band counterpart.

Emission lines in spectra have higher flux compared to the continuum and because of this even when the continuum spectrum of the galaxy is too weak to be detected, the emission-lines can still be found. Narrow-band filters are designed to detect the emission-lines that fall in their small passband range. The flux in the narrow-band filter

is compared with the broad-band filter that is its transmission counterpart (see Fig. 1.12) and the objects that are brighter in the narrow-band filter compared to the broad-band filter (or sometimes even absent from the broad-band filter) are selected to be candidate high-redshift Lyman-α galaxies.
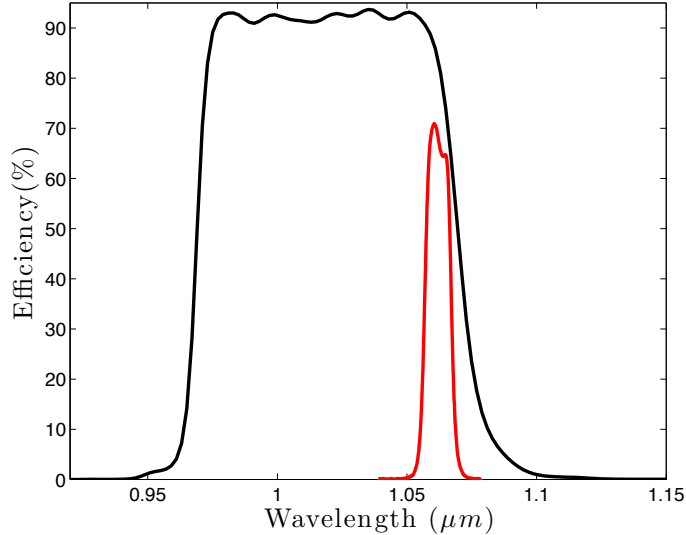
Figure 1.12: The wide and narrow filter transmission curves overplotted (this work). Narrow-band selection method selects galaxies that have excess flux in the narrow filter to that of the wide filter. The main goal is the detection of high redshift Lyman-α emitters, first galaxies formed after Dark Ages.

Emission-line selection can be done in two different ways: by comparing narrow and broad-band colours for two wide and one narrow filters, where one of the wide filter covers narrow transmission and another is located redwards of this composition, or using only two filters - one wide and one narrow.

In the first case, two narrow-wide colours are compared and galaxies that have flux excess in both cases are selected for study. In the second case, a narrow filter magnitudes and the narrow-wide colour are obtained and galaxies are selected with some predefined criteria. Any of the two methods allows us to detect otherwise extremely faint, or undetected in the continuum, very high redshift galaxies.

However, not only high redshift Lyman-α emission-lines fall into the narrow-band filters, but the lower redshift so-called interlopers too. The most common emission-lines that interlopers have are: Hα, [OIII]/Hβ, and [OII]; sometimes also [NII] and other weaker emission lines. The ways of distinguishing between real and "forged" Ly-α candidates is by investigating the wide filter fluxes on the bluer side from the narrow-band and its counterpart wide filters; once undetected in those, galaxies are the candidate high redshift Ly-α.

Recent studies by Matthee et al. (2015) found the two most luminous Lyman-α Emitters (LAEs) in the COSMOS field. Both of these candidates are spectroscopically

confirmed Ly-α galaxies at redshifts $z > 6$ with extremely high Equivalent Widths > 200 Å. A follow-up study by Sobral et al. (2015) found, for the first time, evidence for POPIII stellar population inside one of the galaxies by identifying the [He II] line in the spectrum together with the Ly-α one.
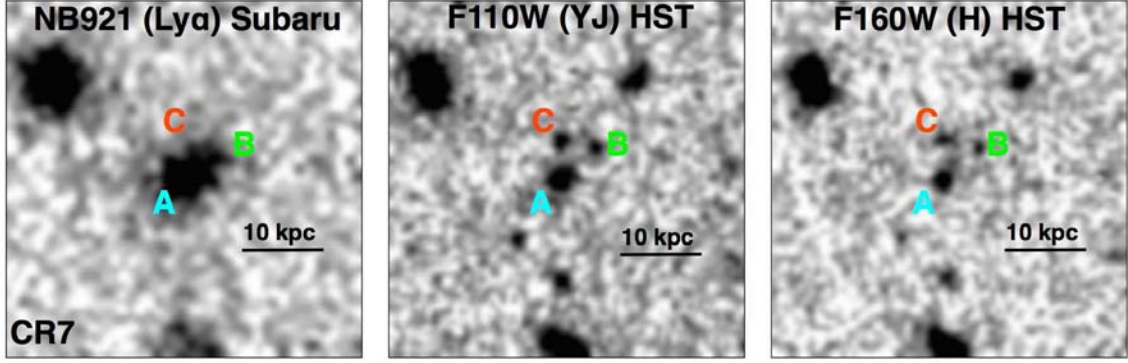
Figure 1.13: CR7 by Sobral et al. (2015) - a galaxy with the very high EW (> 200 Å) and the only galaxy with the detection of HeII line. First galaxy known to host POP III stellar population. A, B and C represent the blobs belonging to the same object.

The narrow-band selection method is an excellent tool not just for identification of the first galaxies, but also for studying the nature of interlopers. Deriving physical properties of the "forged Ly-α galaxies" leads us to study the universe in the wide redshift range. Galaxies selected with the narrow-band method are of course actively star-forming objects in different epochs. Morphologically, narrow-band selected galaxies can vary from compact objects to clumpy, complex structures. Narrow-band selected galaxies allow us to probe extreme ends of the mass-SFR relation (see Sect. 1.4.4), and trace the evolution of the two across long timescales.

1.6 THIS WORK IN PERSPECTIVE

The main goal of this thesis was to explore that properties of the emission line galaxies found when searching for very high redshift Lyman-α galaxies. Unfortunately, a treasure hunt of this sort, in most cases, leaves the searcher empty-handed. The reason why this happens is that the galaxies one is looking for are very, very distant and therefore very faint. On top of that, without a precise knowledge of when exactly the reionization epoch started, one does not have a clear "boundary" up to where we should look for primeval galaxies.

There have been photometric detections of galaxies at as high redshift as ~ 12 (Coe et al. 2013; Brammer et al. 2013), but no spectroscopically confirmed candidates have been reported so far above $z > 8.2$ (Tanvir et al. 2009).

Having no high-redshift Lyman-α detection in my pocket, does not mean that there can be nothing exciting to work on. Together with my collaborators, I have been working on understanding the nature of galaxies at various (lower) redshifts.

We investigated what happens to the slope of the M_* vs SFR relation for low mass galaxies ($M_* < 10^{9.5} M_\odot$) in the redshift range $0.5 < z < 2$. How can the sample selection method bias the galaxy populations in two similar projects. We discovered a galaxy protocluster at the redshift $z \sim 2$ and a large scale structure at the $z \sim 1.15$. These studies are described in Chap. 2 and Chap. 3.

We also tried to understand the galaxy formation and evolution picture in more global frame, across the redshift range of $0 < z < 6$. This project is on-going and we expect to have some very important results when it will get into the final phase of its development.

Finally, in Chap. 4, I summarise results obtained so far and discuss future developments.

2

SELECTION AND STUDY OF GALAXIES AT $z = 0.6 - 2$

Emission line selected galaxies at $z = 0.6 - 2$ in GOODS South: Stellar masses, SFRs, and large scale structure

Ia Kochiashvili[1,2], **Palle Møller**[3], **Bo Milvang-Jensen**[1], **Lise Christensen** [1], **Johan P.U. Fynbo**[1], **Wolfram Freudling** [3], **Benjamin Clément** [4,5], **Jean-Gabriel Cuby** [6], **Johannes Zabl** [1], **Stefano Zibetti** [7]

[1] Dark Cosmology Centre, Niels Bohr Institute, University of Copenhagen, Juliane Maries Vej 30, DK-2100 Copenhagen Ø, Denmark 2Abastumani Astrophysical Observatory, Ilia State University, Kakutsa Cholokashvili Ave 3/5, Tbilisi 0162, Georgia [3] European Southern Observatory, Karl Schwarzschild Strasse 2, D-85748 Garching bei München, Germany [4] Steward Observatory, University of Arizona, 933 North Cherry Avenue, Tucson, AZ, 85721, USA
[5] CRAL, Observatoire de Lyon, Universite ÌĄ Lyon 1, 9 Avenue Ch. Andre ÌĄ, 69561 Saint Genis Laval Cedex, France
[6] Aix Marseille Université, CNRS, LAM (Laboratoire d'Astrophysique de Marseille) UMR 7326, 13388, Marseille, France
[7] INAF-Osservatorio Astrofisico di Arcetri, Largo Enrico Fermi 5, I-50125 Firenze, Italy]

Abstract

We have obtained deep NIR narrow and broad (J and Y) band imaging data of the GOODS-South field. The narrow band filter is centred at 1060 nm corresponding to redshifts $z = 0.62, 1.15, 1.85$ for the strong emission lines Hα, [OIII]/Hβ and [OII], respectively. From those data we extract a well defined sample ($M(AB) = 24.8$ in the narrow band) of objects with large emission line equivalent widths in the narrow band. Via SED fits to published broad band data we identify which of the three lines we have detected and assign redshifts accordingly. This results in a well defined, strong emission line selected sample of galaxies down to lower masses than can easily be obtained with only continuum flux limited selection techniques. We compare the (SED fitting-derived) main sequence of star-formation (MS) of our sample to previous works and find that it has a steeper slope than that of samples of more massive galaxies. We conclude that the MS steepens at lower (below $M_\star = 10^{9.4} M_\odot$) galaxy masses. We also show that the SFR at any redshift is higher in our sample. We attribute this to the targeted selection of galaxies with large emission line equivalent widths, and conclude that our sample forms the upper boundary of the MS.

We briefly investigate and outline how samples with accurate redshifts down to those low stellar masses open a new window to study the formation of large scale structure in the early universe. In particular we report on the detection of a young galaxy cluster at $z = 1.85$ which features a central massive galaxy which is the candidate of an early stage cD galaxy, and we identify a likely filament mapped out by [OIII] and $H\beta$ emitting galaxies at $z = 1.15$.

2.1 INTRODUCTION

The study of galaxies at both intermediate and high redshifts has gained tremendous momentum from the concerted efforts to gather deep imaging of large fields and from the ensuing high-quality photometry covering broad spectral ranges. Analyses exploiting those data to derive prime observables such as star-formation rates (SFRs) and stellar masses $M_\star$ have revealed that galaxies follow scaling relations that evolve with redshifts (Brinchmann et al. 2004; Noeske et al. 2007; Daddi et al. 2007). The most comprehensive investigations are based on multi-band photometry, and the ability to obtain redshift information by fitting theoretical model data is a critical component (Daddi et al. 2007; Karim et al. 2011; Bayliss et al. 2011; Koyama et al. 2013). The photometric redshift accuracy also places a fundamental limitation on the results from the unavoidable uncertainty in the assignment of redshifts to each galaxy, an uncertainty that propagates to all the derived physical parameters of the galaxies.

There are different methods of addressing the galaxy formation and evolution quest. Galaxy samples are selected differently and therefore probe different aspects of galaxy evolution. Intensively star-forming galaxies have been studied for nearly two decades with the help of the Lyman-break selection technique (Steidel et al. 2003; Shapley 2011). Flux limited high-redshift samples selected at primarily red wavelengths include luminous infrared galaxies (LIRGs), ultra luminous infrared galaxies (ULIRGs), and massive ($M_\star \sim 10^{10.7} M_\odot$) red ellipticals (Jacobs et al. 2011). Sub-millimetre selected samples target high-redshift galaxies with unprecedented star-formation rates (Michałowski et al. 2010; Hodge et al. 2013). Long-duration gamma-ray bursts (GRBs) select fainter and bluer star-forming galaxies (Le Floc'h et al. 2003; Christensen et al. 2004). Also selection effects play a role here, because it has been suggested that GRB hosts have to have low stellar masses (e.g. Castro Cerón et al. 2010), while dusty GRBs occur primarily in more massive host galaxies (Krühler et al. 2011). Absorption-line selected samples allow us to study the gas content of galaxies and can be used to probe the mass-metallicity relation (Ledoux et al. 2006; Møller et al. 2013; Christensen et al. 2014). In a nutshell, these methods all address different populations of galaxies and have different advantages and disadvantages for particular science goals.

To investigate the $M_\star$ vs SFR relation for galaxies found in isolation and in clusters, none of these methods will simultaneously probe the low-mass end of the star-forming main sequence and cover intermediate-to-high redshifts. An alternative method that can help us in achieving this goal is the narrow-band imaging technique (e.g. Pritchet & Hartwick 1987). Emission-line-selected samples are smaller, but the advantage is that they allow us to probe fainter objects than broad-band-selected samples do and still have a much more accurate photometric redshift determination (Ly et al. 2012; Sobral et al. 2014). Narrow-band selected objects have excess flux in the narrow-band filter compared to a broad-band filter that covers adjacent wavelengths. Primarily, this technique has been used to detect high-redshift Lyman-α (Lyα) emission lines because $Ly\alpha$ is a good tracer of galaxies at the beginning of the reionization era (Partridge & Peebles 1967;

Malhotra & Rhoads 2004; Nilsson et al. 2007).

The goal of this paper is to fill in the knowledge gap concerning the low-mass end of the main sequence of star-forming galaxies in a broad redshift range. We have analysed emission-line sources selected from deep 1060 nm narrow-band ($NB1060$ hereafter) and Y- and J-band observations of the GOODS-South field from Clément et al. (2012). The GOODS-South field is ideal for our objective because the field has been observed in a wide range of wavelengths and with good photometric accuracy (Giavalisco et al. 2004) allowing for very detailed photometric scrutiny of sources in the field. When searching for emission-line galaxies at redshifts $z \sim 7.7$, we also detect galaxies with emission lines other than $Ly\alpha$ falling within the narrow-band filter. In this way, we can probe the universe in four independent redshift slices: besides the high-redshift $Ly\alpha$ line, we detect galaxies at $z = 0.6$ from strong $H\alpha$ emission lines, at $z = 1.12/1.18$ from [OIII]/$H\beta$ emission lines, and $z = 1.85$ where galaxies with strong [OII] emission lines lie. We performed multi-band photometry SED fitting and derived masses and SFRs of 40 emission-line galaxies at three different redshift slices. We analysed the redshift evolution of the $M_\star$-SFR relation spanning more than four decades in stellar mass from a unique data set.

The paper is organized as follows. In Sect. 2 we describe candidate-selection process and the data sets used for this project. Section 3 characterises the spectroscopic and photometric properties of the selected galaxies and compare with redshifts from the MUSYC survey. Sections 4 and 5 present the results and discusses these.

Throughout this paper, we assume a flat cosmology with $\Omega_\Lambda = 0.70$, $\Omega_m = 0.30$, and a Hubble constant of $H_0 = 70$ km s^{-1} Mpc^{-1}.

2.2 SELECTION OF EMISSION-LINE GALAXIES

2.2.1 IMAGING OBSERVATIONS

The GOODS South field was observed with VLT/HAWK-I in the 1060 nm narrow-band and broad J- and Y-band filters (see filter transmission curves in Fig.2.1) as part of a Large ESO Programme (Prog-Id: 181.A-0485, PI: Cuby) and a HAWK-I science verification programme (Prog-Id: 60.A-9284(B), PI: Fontana). For details on the observations and data reduction we refer to Castellano et al. (2010) and Clément et al. (2012). The field is in the northern half of the GOODS-S field (centred at RA,Dec = $03^h32^m29^s$,-$27^d44^m42^s$, J2000).

2.2.2 CANDIDATE SELECTION

For object detection and photometry, we used the software package SExtractor (Bertin & Arnouts 1996). For the actual selection of candidate emission line galaxies we only relied on the Hawk-I $NB1060$, Y and J-band images. As a detection image we use the narrow-band image, and photometry is subsequently done in all three images with aperture sizes defined in the $NB1060$ image. Before object detection the detection image is convolved
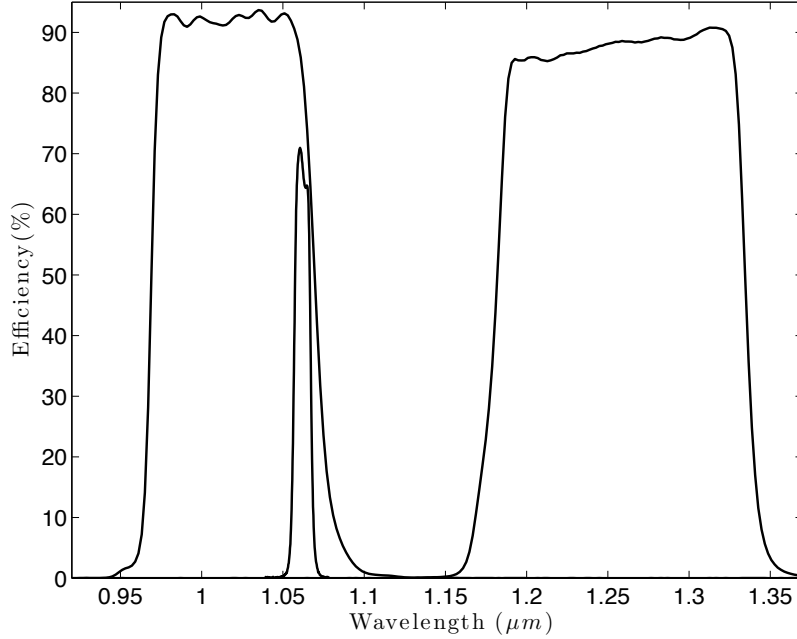
Figure 2.1: Transmission curves for the $NB1060$, Y, and J-band filters. The narrow filter transmission is located in the red wing of the Y-band filter and is entirely outside the J-band transmission range.

with a Gaussian filter function having a FWHM equal to that of point sources. We used a detection threshold of 1.5 times the background sky-noise in the unfiltered detection image and a minimum area of 15 connected pixels above the detection threshold in the filtered image. Isophotal apertures are defined on the detection image and those same isophotal apertures are used in the different bands ($NB1060$, Y, J). We rejected objects close to the chip gap and the edge of the image where the noise is higher. The regions of the field masked out in this way are shown in Fig. 2.14. In total, we detect 2700 objects at a signal-to-noise ratio greater than 5 in the narrow-band. We measured the flux of all objects in the isophotal aperture that is suitable for precise colour measurement since the effective seeing of the images are very similar. To have a measure of the total magnitudes, we used the so-called AUTO aperture in SExtractor. The AUTO aperture is an elliptical aperture defined by the isophotal shape of the object. For objects blended with neighbours a scaled isophotal flux is used to estimate the total flux. Our final catalogue is complete (10σ detection) down to $M(AB) = 24.8$ in the narrow band.

To select objects with excess flux in the narrow band, we employed the method introduced by Møller & Warren (1993) and refined by Fynbo et al. (2003). This method uses two broad band filters that bracket the narrow band. Plotting the two narrow-minus-broad colours against each other causes objects with an emission line within the narrow pass band to drop diagonally down to the left (Fig. 2.2 upper panel). We computed the distribution of the cloud of continuum emitters using theoretical spectral energy
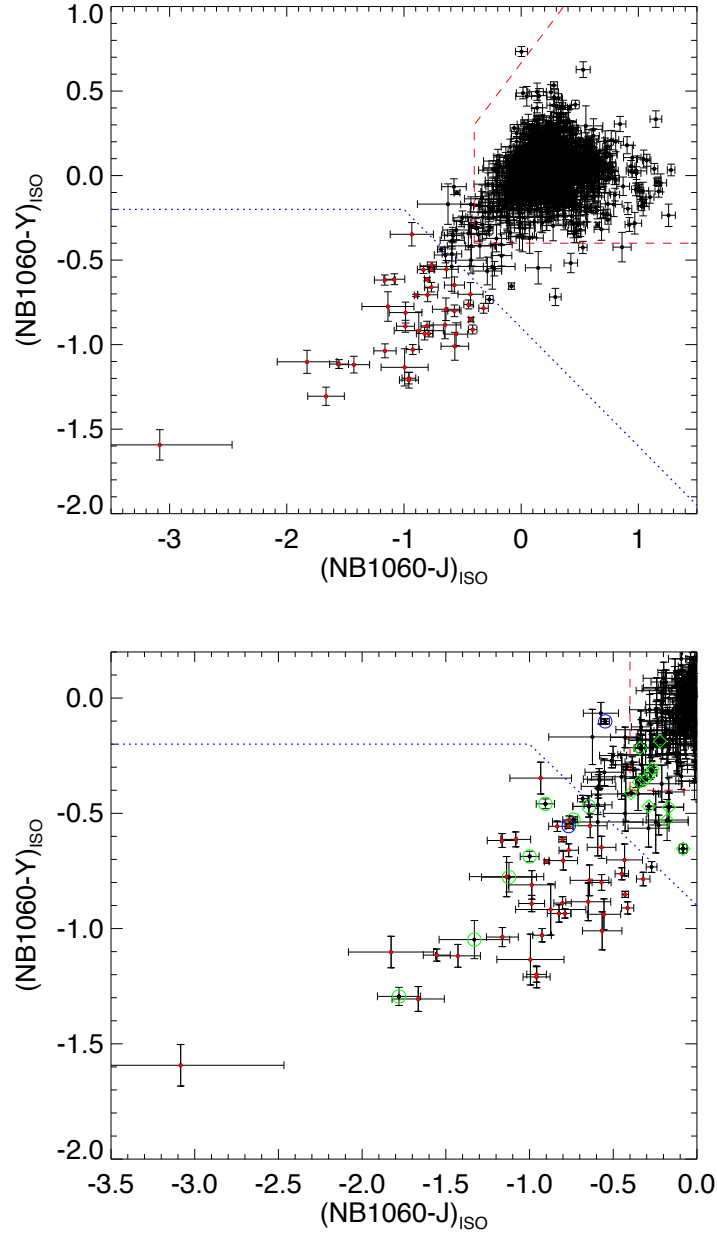
Figure 2.2: Colour-colour diagram for objects detected in the NB1060 image and brighter than NB1060(AUTO) = 24.8. The top panel represents the colour distribution of continuum and emission-line galaxies. The expected region occupied by continuum emitters is enclosed by a red dashed line, whereas the region we use to select candidate line emitters lies below the blue dotted line. Red dots represent objects from the basic sample, i.e. objects that meet the selection criteria. The lower panel additionally shows objects in green circles and green diamonds that have emission-lines but do not enter our basic sample because they either are masked or lie outside a conservatively defined selection area (therefore above the blue dotted line).

distributions from Bruzual & Charlot (2003), and enclosed the region where the model galaxies fall in Fig. 2.2 (for details see Fynbo et al. (2003)). All objects in our catalogue are plotted in the upper panel of Fig. 2.2, and it is seen that most objects do indeed fall inside the red dashed line. The selection window we have adopted is seen below and to the left side of the main locus of continuum objects. For $NB1060 - J < -1$, we selected objects with $NB1060 - Y < -0.2$. For $NB1060 - J > -1$ we use $NB1060 - Y < -0.7 \times (NB1060 - J) - 0.9$. The 40 objects found inside this area and, at least 1σ from the border, make up our "basic sample" and are listed in Table 2.1 and are highlighted in Fig. 2.2. The basic sample is complete in that we have included all objects within the unmasked area of the observed field down to $NB1060 = 24.8$, and it is therefore suitable for statistical studies within the unmasked area that spans 38.7 square arcminutes on the sky.

We searched the NED/IPAC[1] and SIMBAD (Wenger et al. 2007) databases and found spectroscopic, secure redshifts for a subset of the basic sample, as listed in Table 2.1.

As a check of the selection, the images were inspected in ds9 in RGB mode, with blue=Y, green=NB1060, red=J. Objects were marked that looked green (i.e. showed some degree of narrow-band excess) and which looked like galaxies and not artefacts or noise. The mask used in defining the basic sample was not used, i.e. also objects located in higher noise regions of the image were included. After removing the basic sample of 40 galaxies and the ELG00 galaxy, this visually-identified narrow-band excess sample comprised 58 objects. There were three not necessarily mutually exclusive reasons for these galaxies not being part of the basic sample: (1) their colours were outside the selection region i.e. the observed EW was too low; (2) they were in a masked part of the image; or (3) they were fainter than NB1060(AUTO) = 24.8. SIMBAD was searched, and 18 of the 58 objects had a spectroscopic, secure redshift. For all 18 galaxies (named x01 to x18), the redshift matched an emission line (see Table 2.2). These 18 galaxies, as well as ELG00 (see below), do not fulfil our selection criteria and thus cannot be used in our basic sample, but together with the basic sample they form an "extended sample".

In addition we obtained spectra and determined redshifts for two objects as described in Sect. 2.3.1. The two objects are highlighted by blue circles in Fig. 2.2, where one is seen to be in our basic sample (ELG55) while the other is directly to the left of the large cloud of galaxies. This is an intriguingly strange position since it shows that it has an emission line in the $(NB1060 - J)$ colour, but no line in the $(NB1060 - Y)$ colour. It is not in the basic sample, so we have named it ELG00 and list it in the first line of Table 2.2.

In Fig.A.1 we show $NB1060$, Y and HST F606W-band thumbnails (the last is the deepest optical band we have) for all 40 galaxies in the basic sample, and also including ELG00 of the extended sample. As seen, all are indeed detected in the F606W-band so are not consistent with being Lyα emitters at $z = 7.7$. The candidates have very mixed morphologies ranging from bright spirals over irregular galaxies with multiple cores to

---

[1]The NASA/IPAC Extragalactic Database (NED) is operated by the Jet Propulsion Laboratory, California Institute of Technology, under contract with the National Aeronautics and Space Administration.
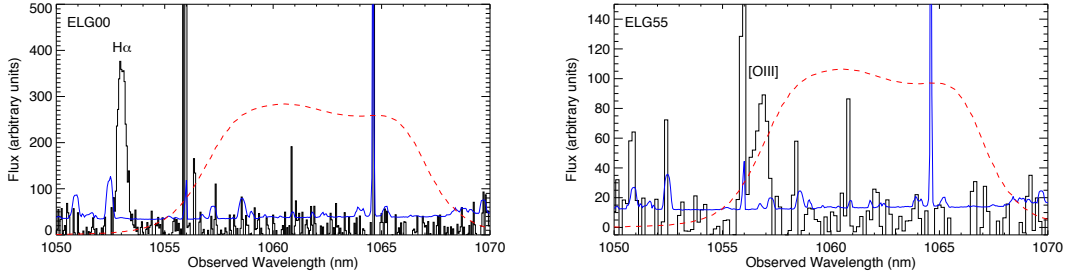
Figure 2.3: X-shooter spectra of ELG00 (left) and ELG55 (right). The red dashed line shows the NB1060 filter transmission curve, the blue solid line is the error spectrum. Hα of ELG00 is seen to be out of the narrow band pass transmission causing its peculiar colours.

very faint compact systems.

2.3 Characterization of the candidate emission-line galaxies

2.3.1 Spectroscopic observations

On March 15 and 16, 2013 we secured redshift measurements for two objects in our catalogue. The spectra were obtained with the X-shooter spectrograph (Vernet et al. 2011) installed at the Cassegrain focus of the Very Large Telescope (VLT), Unit 2 – Kueyen, operated by the European Southern Observatory (ESO) on Cerro Paranal in Chile (prog. ID 090.A-0147). The spectra were reduced with the ESO X-shooter pipeline 2.0 (Goldoni 2011). In Fig. 2.3 we show the X-shooter spectra around the region of the $NB1060$ filter.

One of the object (ELG55, lower panel of Fig. 2.3) belongs to the basic sample, and we see that the line is confirmed to [OIII]λ5007 based on the detection of [OIII]λ4959 and [OII]λ3727, and the derived redshift is 1.1107.

The other object (ELG00, upper panel of Fig. 2.3) is not in the basic sample but was observed because of its strange position in the colour-colour plot as described in Sect. 2.2.2 above. Here we see a strong Hα line (based on the detection of a wide range of other lines in the visual spectral region) and the derived redshift is 0.6045. The strong Hα line is located in the very wing of the filter curve as given by the ESO web page [2] We do not detect the [NII]λ6583 line in the spectrum.

2.3.2 Photometric redshifts

The very conservative selection criteria employed for our basic sample definition ensures that a strong emission line is present in the narrow-band filter. Therefore the task of

---

[2] http://www.eso.org/sci/facilities/paranal/instruments/hawki/inst/filters/hawki_NB1060.dat

Table 2.1: 40 objects in our statistically complete "basic sample". In the first column, we present our ID numbers for the candidate emission-line galaxies. Next we list RA & Dec, NB magnitudes, colours and redshift from our work accordingly. In cols. 7 and 8 we present redshifts reported in the MUSYC catalogue: z[peak] corresponds to the best assigned redshift by the survey and [zmin] and [zmax] represent 1σ minimum and maximum redshift values. Column 9 lists the emission lines observed in the narrow band filter; here [OIII] means [OIII]/Hβ. For 5 objects we could not uniquely assign a redshift; for four of them we have preferred value, which is listed first, while for ELG30 we do not have a preferred redshift identification and we consider all the three listed values possible. Column 10 lists emission-line fluxes and Col. 11 and 12 correspond to the observed frame equivalent width and references to the spectroscopic redshift literature, respectively.

ID	RA & DEC	NB	NB − Y	NB − J	Redshift	z[Peak]	z[min/max]	line ID	Em. Line flux	Eq.Width	Ref
ELG#	(2000.0)	mag (AUTO)	mag (ISO)	mag (ISO)	This work	MUSYC	MUSYC		[$10^{-17}erg/s/cm^2$]		
03	03:32:40.32 -27:47:22.71	22.11 ± 0.01	−0.61 ± 0.01	−0.80 ± 0.02	0.619	0.61	0.60/0.63	Hα	17.54 ± 0.14	188.3 ± 2.0	(1)
04	03:32:44.30 -27:46:59.99	23.60 ± 0.03	−0.62 ± 0.03	−1.16 ± 0.09	1.144	1.12	1.10/1.14	[OIII]	9.03 ± 0.13	288.1 ± 9.1	(2)
05	03:32:36.30 -27:47:32.63	23.43 ± 0.02	−1.20 ± 0.03	−0.96 ± 0.06	1.86	2.29	2.05/2.48	[OII]	28.55 ± 0.12	533.8 ± 11.3	(3)
06	03:32:37.20 -27:47:25.56	23.88 ± 0.06	−0.70 ± 0.07	−0.43 ± 0.11	1.85	−	−	[OII]	13.28 ± 0.22	405.5 ± 25.7	
09	03:32:41.34 -27:46:46.23	24.27 ± 0.05	−0.55 ± 0.05	−0.64 ± 0.10	0.62	0.60	0.56/0.64	Hα	1.98 ± 0.08	155.3 ± 8.2	
10	03:32:37.97 -27:46:51.86	21.03 ± 0.01	−0.71 ± 0.01	−0.90 ± 0.01	0.62	0.63	0.62/0.63	Hα	43.86 ± 0.41	235.8 ± 2.5	(4)
11	03:32:42.76 -27:46:33.19	24.45 ± 0.05	−0.81 ± 0.06	−0.99 ± 0.14	0.62	0.64	0.62/0.66	Hα	1.65 ± 0.08	201.2 ± 10.6	
12	03:32:37.36 -27:46:45.52	21.91 ± 0.01	−0.85 ± 0.01	−0.43 ± 0.02	1.843	2.26	2.22/2.31	[OII]	155.23 ± 0.19	257.3 ± 2.7	(5)
14	03:32:36.83 -27:46:51.52	24.51 ± 0.06	−0.88 ± 0.08	−0.65 ± 0.13	1.85	1.80	1.72/1.89	[OII]	2.85 ± 0.08	153.6 ± 9.7	
15	03:32:37.08 -27:46:47.03	23.10 ± 0.02	−1.03 ± 0.03	−0.93 ± 0.06	1.85	1.93	1.84/2.04	[OII]	24.09 ± 0.13	287.1 ± 6.1	
16	03:32:35.81 -27:46:43.62	23.26 ± 0.03	−0.79 ± 0.03	−0.32 ± 0.04	1.85	2.13	1.88/2.32	[OII]	21.17 ± 0.13	163.8 ± 5.2	(6)
20	03:32:36.69 -27:46:20.98	23.74 ± 0.02	−0.90 ± 0.04	−0.99 ± 0.08	1.85	1.90	1.80/2.00	[OII]	9.42 ± 0.07	234.3 ± 5.0	(3)
21	03:32:37.45 -27:46:15.34	24.55 ± 0.07	−0.79 ± 0.07	−0.64 ± 0.12	1.85	1.94	1.83/2.04	[OII]	4.52 ± 0.09	141.6 ± 10.5	
22	03:32:36.55 -27:46:12.28	22.60 ± 0.01	−0.93 ± 0.02	−0.79 ± 0.04	1.85	1.94	1.90/1.98	[OII]	53.91 ± 0.11	351.3 ± 3.7	(3)
23	03:32:39.52 -27:45:59.75	24.59 ± 0.08	−1.13 ± 0.11	−0.99 ± 0.20	1.85	1.86	1.43/2.31	[OII]	6.32 ± 0.14	314.9 ± 26.7	
25	03:32:39.33 -27:45:55.14	23.38 ± 0.04	−1.21 ± 0.05	−0.96 ± 0.08	1.85	1.90	1.75/2.04	[OII]	22.05 ± 0.24	474.7 ± 20.1	
26	03:32:45.73 -27:45:24.97	23.72 ± 0.04	−0.71 ± 0.04	−0.80 ± 0.08	1.15	1.09	1.05/1.12	[OIII]	5.29 ± 0.12	178.7 ± 7.6	
28	03:32:27.82 -27:46:35.07	24.02 ± 0.03	−1.31 ± 0.05	−1.67 ± 0.16	1.15	−	−	[OIII]	6.50 ± 0.11	699.8 ± 22.2	
30	03:32:30.03 -27:46:04.24	24.35 ± 0.05	−1.59 ± 0.09	−3.08 ± 0.61	1.15/1.85/0.62	−	−	[OIII]/[OII]/Hα	2.96 ± 0.16	1851.6 ± 97.9	
34	03:32:26.60 -27:46:05.02	24.76 ± 0.08	−0.77 ± 0.09	−1.14 ± 0.22	1.15	1.28	1.06/1.55	[OII]	1.38 ± 0.12	294.7 ± 24.9	
35	03:32:21.53 -27:46:18.71	23.31 ± 0.03	−0.80 ± 0.03	−0.57 ± 0.06	1.85	1.74	1.50/1.96	[OII]	29.74 ± 0.19	420.8 ± 13.4	
36	03:32:26.68 -27:45:54.79	23.98 ± 0.04	−1.12 ± 0.05	−1.43 ± 0.13	1.15	1.18	1.09/1.30	[OIII]	4.60 ± 0.15	566.7 ± 24.0	
37	03:32:21.69 -27:46:16.57	24.70 ± 0.07	−1.01 ± 0.08	−0.57 ± 0.12	1.85	2.45	2.32/2.59	[OII]	4.16 ± 0.10	274.7 ± 20.3	
41	03:32:21.26 -27:46:02.55	23.68 ± 0.03	−0.93 ± 0.04	−0.82 ± 0.07	1.85	1.53	1.12/1.74	[OII]	8.11 ± 0.11	272.6 ± 8.7	
43	03:32:19.60 -27:46:08.31	23.63 ± 0.03	−0.61 ± 0.03	−1.08 ± 0.09	1.15	1.07	1.05/1.09	[OIII]	5.43 ± 0.16	683.2 ± 21.7	
45	03:32:42.51 -27:44:15.55	23.38 ± 0.03	−0.66 ± 0.03	−0.77 ± 0.06	0.62	0.61	0.60/0.63	Hα	4.73 ± 0.12	169.6 ± 5.4	
51	03:32:16.50 -27:44:45.04	22.49 ± 0.02	−0.53 ± 0.02	−0.76 ± 0.04	1.15/0.62	1.11	1.10/1.12	[OIII]/Hα	19.61 ± 0.31	809.5 ± 17.1	
52	03:32:41.59 -27:42:50.68	24.62 ± 0.08	−0.35 ± 0.08	−0.93 ± 0.18	1.15	−	−	[OIII]	1.44 ± 0.12	238.3 ± 20.2	
53	03:32:13.15 -27:45:01.19	23.18 ± 0.02	−0.91 ± 0.03	−0.41 ± 0.04	1.85	2.06	1.95/2.17	[OII]	27.63 ± 0.12	249.4 ± 5.3	
54	03:32:12.98 -27:44:59.81	23.16 ± 0.02	−0.89 ± 0.03	−0.80 ± 0.05	1.85	−	−	[OII]	35.58 ± 0.15	476.8 ± 10.1	
55	03:32:16.31 -27:44:41.93	22.03 ± 0.01	−0.56 ± 0.01	−0.77 ± 0.02	1.1107	1.12	1.11/1.12	[OIII]	43.90 ± 0.14	159.8 ± 1.7	(*)
58	03:32:41.68 -27:42:04.45	23.50 ± 0.03	−1.04 ± 0.04	−1.16 ± 0.10	1.15/1.85	1.25	1.21/1.30	[OIII]/[OII]	4.81 ± 0.15	384.9 ± 12.2	
62	03:32:34.22 -27:42:31.37	24.37 ± 0.04	−1.10 ± 0.07	−1.83 ± 0.25	0.62	0.61	0.60/0.63	Hα	1.90 ± 0.07	202.4 ± 8.6	
65	03:32:39.20 -27:41:44.69	23.05 ± 0.02	−1.12 ± 0.03	−1.55 ± 0.08	1.15	1.14	1.12/1.15	[OIII]	9.54 ± 0.17	546.4 ± 11.6	
66	03:32:38.22 -27:41:45.51	24.31 ± 0.07	−0.92 ± 0.11	−0.87 ± 0.21	1.85/1.15	−	−	[OII]/[OIII]	5.67 ± 0.19	545.0 ± 40.4	
68	03:32:23.88 -27:42:11.56	24.07 ± 0.05	−0.65 ± 0.05	−0.57 ± 0.09	1.85	1.60	1.50/1.70	[OII]	3.94 ± 0.12	219.5 ± 11.6	
70	03:32:33.03 -27:40:48.06	23.14 ± 0.02	−0.56 ± 0.02	−0.83 ± 0.06	1.15	1.13	1.11/1.14	[OIII]	7.26 ± 0.10	174.9 ± 3.7	
75	03:32:30.36 -27:41:46.66	24.37 ± 0.06	−0.94 ± 0.07	−0.56 ± 0.10	1.85/1.15	−	−	[OII]/[OIII]	5.99 ± 0.13	321.0 ± 20.4	
76	03:32:22.75 -27:42:11.59	23.17 ± 0.02	−0.76 ± 0.03	−0.45 ± 0.04	1.85	1.89	1.76/2.00	[OII]	28.31 ± 0.12	258.4 ± 5.5	
78	03:32:33.89 -27:42:37.92	20.13 ± 0.01	−0.73 ± 0.01	−0.74 ± 0.01	0.624	0.64	0.64/0.65	Hα	183.81 ± 0.90	210.9 ± 2.2	(7)

(1) Ravikumar et al. (2007); (2) Xu et al. (2007); (3) Trump et al. (2011); (4) Rodrigues et al. (2008); (5) Mignoli et al. (2005); (6) Guo et al. (2012); (*) This work (7) Balestra et al. (2010);

Table 2.2: Continuation of Table 2.1 with candidates from the extended sample. Col.: ID number, Col.2: coordinates of the objects. Redshift and line IDs are listed in third and fourth columns respectively. Column 5 lists narrow-band magnitudes and magnitude errors. Columns 6 and 7 present colours and colour errors for Y and J filters respectively. And final three columns are emission-line fluxes, observed frame equivalent widths, and references to the literature where we obtain spectroscopic redshift.

ID	RA & DEC	Redshift	line ID	NB	$NB - Y$	$NB - J$	Em.line flux	Eq.Width	Ref.
	(2000.0)	spectroscopic		mag (AUTO)	mag (ISO)	mag (ISO)	$[10^{-17}erg/s/cm^2]$		
ELG00	03:32:18.57 -27:42:29.50	0.6045	Hα	22.46 ± 0.01	-0.10 ± 0.01	-0.55 ± 0.02	5.07 ± 0.05	69.6 ± 0.7	(*)
x01	03:32:13.24 -27:42:40.03	0.6072	Hα	18.88 ± 0.01	-0.36 ± 0.01	-0.35 ± 0.01	227.56 ± 0.21	152.8 ± 0.1	(1)
x02	03:32:23.40 -27:43:16.58	0.615	Hα	19.72 ± 0.01	-0.47 ± 0.01	-0.29 ± 0.01	98.15 ± 0.16	135.4 ± 0.2	(2)
x03	03:32:41.83 -27:40:42.31	0.6162	Hα	23.35 ± 0.02	-1.29 ± 0.04	-1.78 ± 0.13	6.50 ± 0.16	721.0 ± 17.8	(1)
x04	03:32:38.59 -27:46:31.36	0.625	Hα	20.87 ± 0.01	-0.31 ± 0.01	-0.27 ± 0.01	25.03 ± 0.13	83.4 ± 0.4	(3)
x05	03:32:31.50 -27:41:58.04	0.620	Hα	23.32 ± 0.02	-0.32 ± 0.02	-0.27 ± 0.03	2.48 ± 0.05	77.0 ± 1.6	(1)
x06	03:32:45.65 -27:44:05.80	0.6206	Hα	20.15 ± 0.01	-0.41 ± 0.01	-0.39 ± 0.01	63.40 ± 0.17	127.7 ± 0.3	(1)
x07	03:32:28.01 -27:43:57.44	0.6207	Hα	21.93 ± 0.01	-0.53 ± 0.01	-0.78 ± 0.03	12.70 ± 0.16	133.4 ± 1.7	(4)
x08	03:32:40.79 -27:46:15.70	0.6218	Hα	19.57 ± 0.01	-0.36 ± 0.01	-0.31 ± 0.01	85.02 ± 0.20	86.6 ± 0.2	(1)
x09	03:32:46.75 -27:46:24.02	0.6250	Hα	24.86 ± 0.06	-0.78 ± 0.06	-1.12 ± 0.16	0.98 ± 0.07	169.8 ± 11.5	(5)
x10	03:32:22.25 -27:49:01.47	1.109	[O$\textsc{iii}$]	22.98 ± 0.02	-0.19 ± 0.02	-0.22 ± 0.03	2.09 ± 0.04	41.3 ± 0.8	(6)
x11	03:32:27.66 -27:45:05.77	1.110	[O$\textsc{iii}$]	23.02 ± 0.02	-0.22 ± 0.02	-0.34 ± 0.04	3.55 ± 0.09	86.8 ± 2.2	(6)
x12	03:32:26.77 -27:45:30.63	1.122	[O$\textsc{iii}$]	22.97 ± 0.02	-0.69 ± 0.02	-1.00 ± 0.06	7.11 ± 0.17	290.4 ± 6.8	(6)
x13	03:32:18.81 -27:49:08.59	1.128	[O$\textsc{iii}$]	23.19 ± 0.02	-0.46 ± 0.02	-0.91 ± 0.05	4.66 ± 0.10	177.2 ± 3.7	(7)
x14	03:32:49.83 -27:46:58.30	1.174	Hβ	24.70 ± 0.06	-1.05 ± 0.08	-1.33 ± 0.21	1.44 ± 0.09	293.3 ± 17.8	(1)
x15	03:32:17.11 -27:42:20.95	1.749	[Ne$\textsc{iii}$]	24.52 ± 0.05	-0.47 ± 0.05	-0.65 ± 0.10	0.51 ± 0.03	41.2 ± 2.2	(8)
x16	03:32:38.80 -27:47:14.82	1.836	[O$\textsc{ii}$]	22.67 ± 0.02	-0.65 ± 0.02	-0.08 ± 0.02	8.17 ± 0.16	209.6 ± 4.0	(9)
x17	03:32:18.43 -27:42:51.95	1.846	[O$\textsc{ii}$]	25.08 ± 0.09	-0.53 ± 0.09	-0.18 ± 0.13	0.56 ± 0.05	93.5 ± 9.2	(8)
x18	03:32:36.69 -27:46:48.48	1.86	[O$\textsc{ii}$]	24.60 ± 0.07	-0.47 ± 0.06	-0.17 ± 0.09	0.91 ± 0.07	101.8 ± 7.9	(10)

(*) This work; (1) Balestra et al. (2010); (2) Vanzella et al. (2005); (3) Szokoly et al. (2004); (4) Le Fèvre et al. (2004); (5)Xia et al. (2011); (6) Vanzella et al. (2006); (7) Villforth et al. (2012); (8) Straughn et al. (2011); (9) Guo et al. (2012); (10) Trump et al. (2011);

redshift determination of our narrow-band-selected sample is reduced to determining which of the three most likely redshift groups each object belongs to, Hα, [OIII]/Hβ, or [OII]. In a few cases we already have spectroscopic confirmations, and for the remainder we rely on photometric redshift analysis. For this we take advantage of the variety of photometric data available for the GOODS field. We explored a wide range of available data sets, and in the end we concluded that the most robust results are obtained primarily using the available photometry from the CANDELS survey (Guo et al. 2013) (G13 hereafter). This survey includes nearly 35000 sources that combine data from among others *HST*-WFC3 and *HST*-ACS, VLT-VIMOS, VLT-HawkI, VLT-ISAAC and Spitzer/IRAC, spanning wavelengths from the UV to the near-infrared. The CANDELS catalogue contains magnitudes and magnitude errors for 17 different bands in total. To construct the catalogue, a careful and complete source detection algorithm, as well as flux derivation methods including aperture corrections, were employed. However, no photometric or spectroscopic redshift information is provided in the catalogue.

Y band photometry was not available in G13 for a subset of objects (the last 14 in Table 2.1). For these targets we added our own Y-band photometry (from HAWK-I) to the data sets before the SED fitting and redshift determination. For these objects we performed aperture photometry in circular apertures. The aperture size was matched to the apparent extension of the object on the sky. For each used aperture size, we determined aperture corrections measured on isolated, unsaturated point sources.

For the spectral energy distribution (SED) fits we use the LePhare code (Arnouts et al. 1999; Ilbert et al. 2006). Those fits also provide a first photometric redshift probability distribution, which we use to guide us towards the final "redshift slice" assignments for each object.

To construct the model SED, we used the Bruzual and Charlot (BC03) spectral library (Bruzual & Charlot 2003). The library uses stellar evolutionary tracks for different metallicities and helium abundances from the Padova 1994 stellar synthesis models (Girardi et al. 2000). It generates spectra in the wavelength range from 3200 to 9500 at higher resolution and across a wider wavelength range, 91 to 160 μm with lower resolution, assuming Chabrier initial mass function (IMF) (Chabrier 2003) and the Calzetti extinction law (Calzetti et al. 2000). The ages for the model galaxies range from10^5 to 2×10^{10} yr. The code is based on the exponentially declining star formation history (SFH). We also include contribution from the emission lines in the models. For this, LePhare uses a simple recipe based on the Kennicutt (1998) SFR and UV luminosity relation. The code includes the strongest emission such as the $Ly\alpha$, $H\alpha$, $H\beta$, [OIII] doublet - $\lambda\lambda 4959, 5007$ and [OII], varying the ratio of the above-mentioned lines with [OII]. For further details on LePhare code characteristics, see Ilbert et al. (2006) and the LePhare manual.

For each object we go through the following steps. We fit an SED to the full set of photometric data twice, once using all data points and once where we exclude the narrow band and the Y band since they are both dominated by the emission line, which may skew the fit. We then decide, after visual inspection of each individual fit, whether there

is a unique solution or if two or even all three redshift solutions are possible. This is done independently by four of us and redshifts are only assigned if we all four agree. For most (35) objects there clearly is a unique solution, but for the remaining five objects, no unique redshift assignment is possible this way. In four cases there is a best solution (dubbed "primary redshift" and listed first in Table 2.1) but also a possible secondary solution. In one case (ELG30), all three solutions are possible but none of them are preferred. ELG30 is the object that is in the lowest left-hand corner of Fig. 2.2, that is, it has larger emission line equivalent width than any other object in our sample. Presumably the strong emission lines are confusing the SED fit. All redshifts assigned in this way are provided in Table 2.1. As a final step we then repeat the SED fit but this time locking the redshift to the spectroscopic redshift (when available) or to the assigned redshift based on the identification of the emission line. The purpose of this last fit is to obtain the best-fitted values for stellar mass and star formation rate.

In Fig. 2.3 we show examples of fits to three of the objects with unique solutions, one belonging to each redshift slice. We show both the first fit where the redshift was left as a free parameter, and the final fit with assigned redshift.

The V-I vs Z-J redshift diagnostic plot

In Fig. 2.5 we plot the V-I colour versus the Z-J colour for all the unique object redshifts and the four primary but non-unique redshift solutions. The objects are colour-coded according to redshift slice (Hα blue, [OIII]/Hβ green, and [OII] red). It is seen that the points separate out quite clearly in this diagram, in agreement with the work by Bayliss et al. (2011). Galaxies move from the lower right towards the upper left in this diagram as they move to lower redshifts, and it is a coincidence that the internal scatter of the distribution at any given redshift forms a perfect match to the separation in redshift forced by the wavelengths of the three transitions. It is therefore possible to use this figure as a diagnostic plot to assist slice identification in cases where no unique solution can be found. Our primary redshifts are seen to agree well with this plot, which is further proof that those assignments are correct. We also plotted the last object without redshift assignment (ELG30), and we see that it is mostly embedded in the region occupied by [OII] emitters, also close to [OIII] emitters, but far away from Hα emitters.

We note that ELG30 has the highest equivalent width (EW) emission line of our sample, and that would suggest that it is an [OIII] emitter since they in general have large EW (see e.g. Pénin et al. (2014)). Further insight into the redshift of ELG30 comes from Fig. 2.6, which shows the observed-frame EW of the line in the NB1060 filter (as derived in Sect. 2.4.2) against the (F125W$-$F160W) colour from the G13 catalogue. For $z = 0.62$ (Hα in NB1060), no strong emission lines will be in neither F125W nor F160W. For $z = 1.12$ ([OIII]5007 in NB1060), Hα will be in F125W while no strong lines will be in F160W. For $z = 1.18$ (Hβ in NB1060), no strong lines will be in F125W while Hα will be in F160W. For $z = 1.85$ ([OII] in NB1060), Hβ will be in F125W and [OIII]5007 will be in F160W.
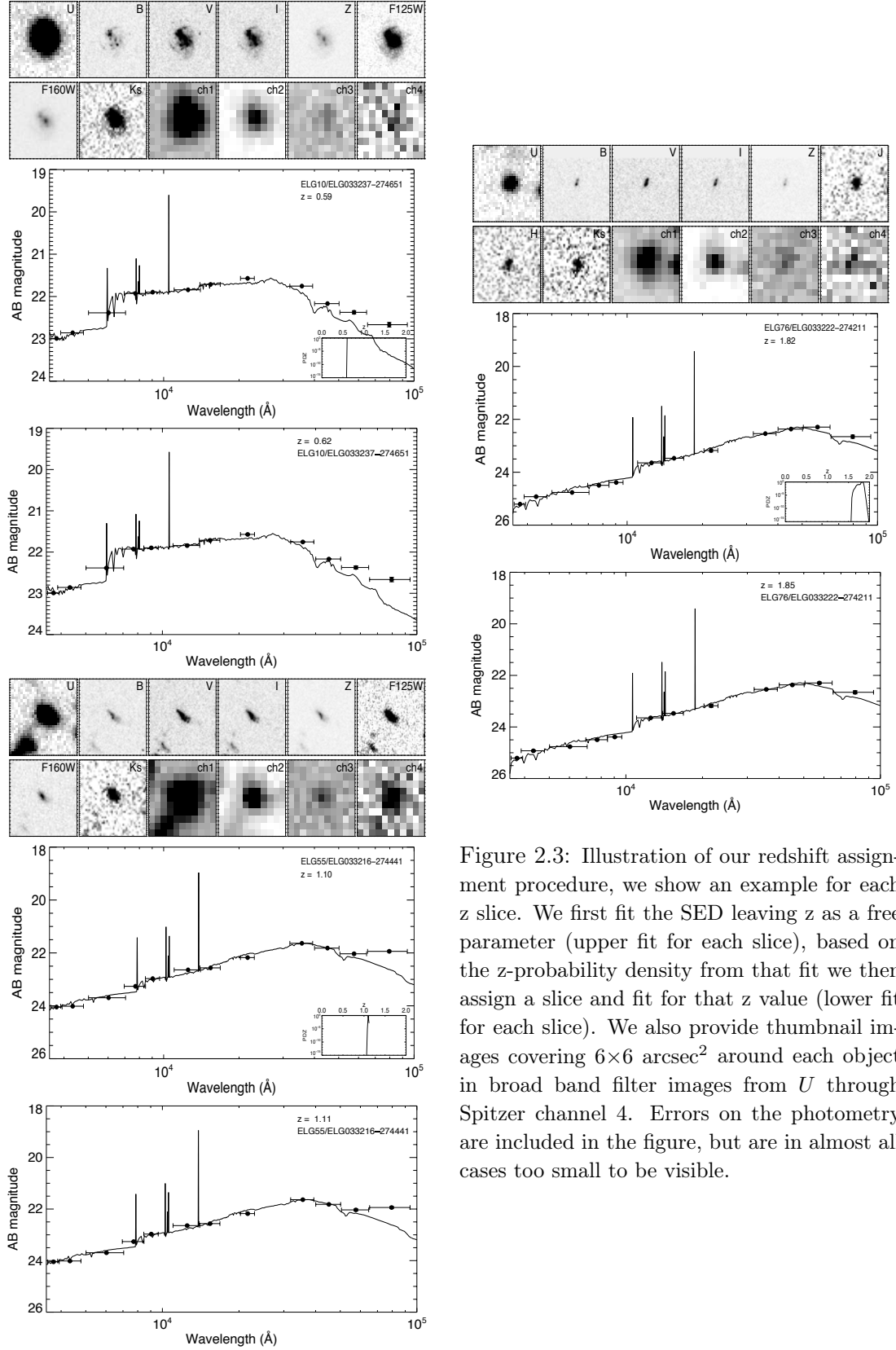
Figure 2.3: Illustration of our redshift assignment procedure, we show an example for each z slice. We first fit the SED leaving z as a free parameter (upper fit for each slice), based on the z-probability density from that fit we then assign a slice and fit for that z value (lower fit for each slice). We also provide thumbnail images covering 6×6 arcsec^2 around each object in broad band filter images from U through Spitzer channel 4. Errors on the photometry are included in the figure, but are in almost all cases too small to be visible.
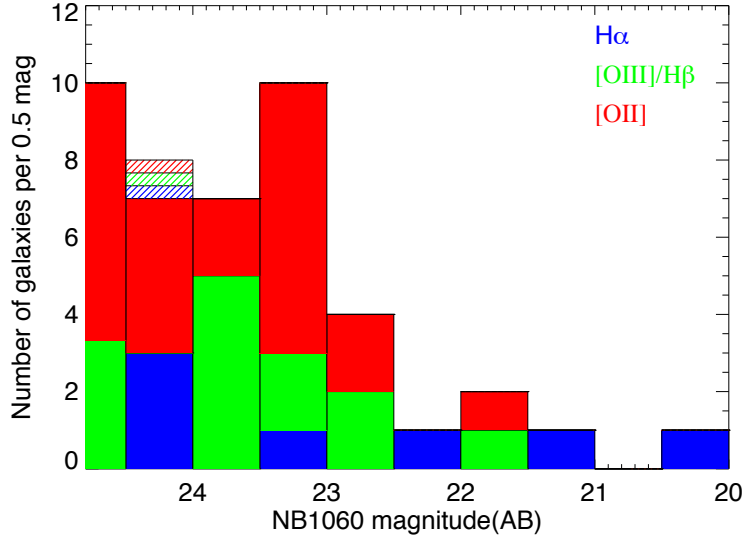
Figure 2.4: Emission-line flux distribution of objects in our three redshift slices. It is seen that the median narrow band magnitude is roughly 23.5 for all slices. ELG 30 is indicated as the hashed object with undecided redshift. The last bin size ($M_{AB} > 24.5$) is 0.3 instead of 0.5 and has been scaled accordingly.

These considerations indicate that a high-EW line emitter with a blue (F125W−F160W) colour such as ELG30 is more likely to be $z = 1.12$ [OIII]5007 than $z = 1.85$ [OII].

All things considered we are not able to assign a primary redshift to ELG30.

Cross-referencing with the MUSYC survey

In Fig. 2.7 we cross-check our final redshift assignments with those of the MUSYC survey (Cardamone et al. 2010). The MUSYC survey consists of imaging of the GOODS-South field in a wide range of broad and medium-wide filters. The MUSYC catalogue contains photometry for more than 84 000 galaxies including the GOODS field. The catalogue lists magnitudes, photometric and spectroscopic (when available) redshifts, and a wide range of other characteristics. Photometric redshifts have been obtained using the EAZY (Easy and Accurate Zphot from Yale) photometric redshift code (Brammer et al. 2008). In Fig. 2.7 we plot the MUSYC redshifts against our redshifts, excluding six objects for which we could find no MUSYC counterpart. Two primary redshift assignments (ELG51 and 58) are shown, and the agreement is seen to be good. We therefore conclude that our redshift assignments for those two objects are secure. The last three non-secure redshifts have no counterparts in MUSYC.

It is seen from Fig. 2.7 that there is very good agreement in the general trend, and the listed errors in the MUSYC catalogue mostly give a reasonable distribution of χ^2, notably for the lower redshift slices. However, four of the 18 certain [OII] emitters are $\approx 2\sigma$ off, one is at 4.6σ, and one at 10.4σ (the latter being ELG12, which has a
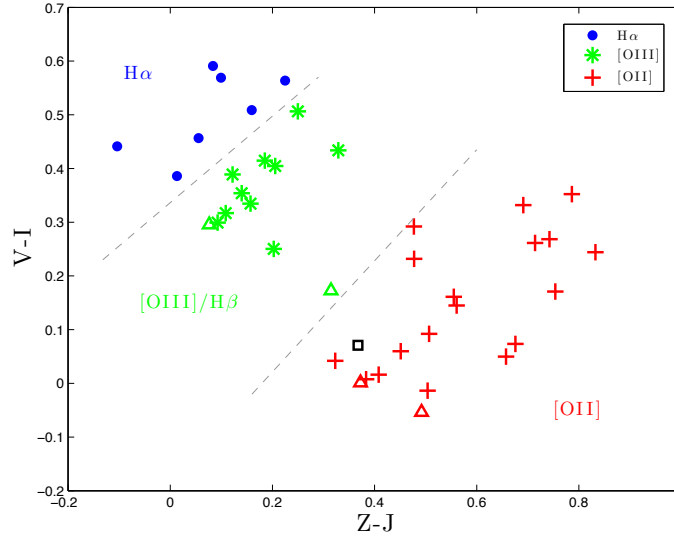
Figure 2.5: $Z - J$ versus $V - I$ colour distribution for our basic sample, with V = F606W, I = F814W, z = F850LP, and J = F125W, as taken from G13. Solid dots are secure redshifts, open triangles are primary redshift solutions, the black square labels ELG30 for which there is no preferred redshift. As in Bayliss et al. (2011), we see a clear separation of redshifts into separate colour groupings, making this diagram useful as a redshift diagnostic for emission-line-selected samples.

spectroscopic redshift and is detected in X-rays, and therefore possibly an AGN). We therefore conclude that while the general trend is in excellent agreement and the errors for the $z = 0.62$ slice are very small, the errors become increasingly larger for the two higher redshift slices, and for the $z = 1.85$ slice the errors are underestimated in about 30% of the cases. Therefore galaxy scaling relations derived from large statistical samples based on only photo-z redshifts are probably reliable out to at least $z = 0.6$, but at higher redshifts there are significant, and in some cases significantly underestimated, errors on the redshifts that will propagate into errors on the derived physical parameters, such as stellar masses ($M_\star$) and star formation rates (SFR). At higher redshifts one might therefore obtain more accurate results from smaller samples but with more accurate redshifts.

2.3.3 Broad band flux depth

Our survey function is defined based on the narrow-band flux limit and emission-line equivalent width. This means that we do not have any actual lower limit on broad band fluxes in our sample. As a result, our survey differs significantly from spectroscopic surveys where strict broad-band flux limits are used for target selection to ensure a good probability that a redshift can be determined from the spectrum. We expect that our sample is deeper than spectroscopic surveys in the same field and to assess how much
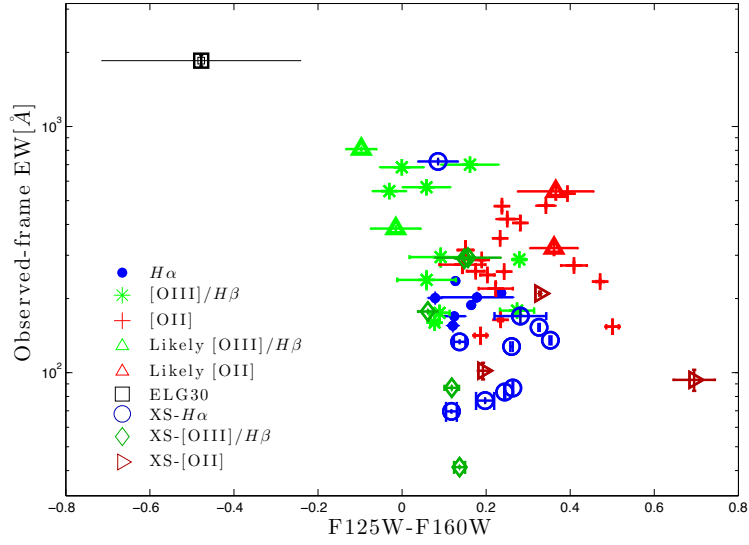
Figure 2.6: Observed-frame EW of the line in the NB1060 filter (as derived from the photometry) against (F125W−F160W) colour for the basic sample and the extended sample (labelled XS in the legend).
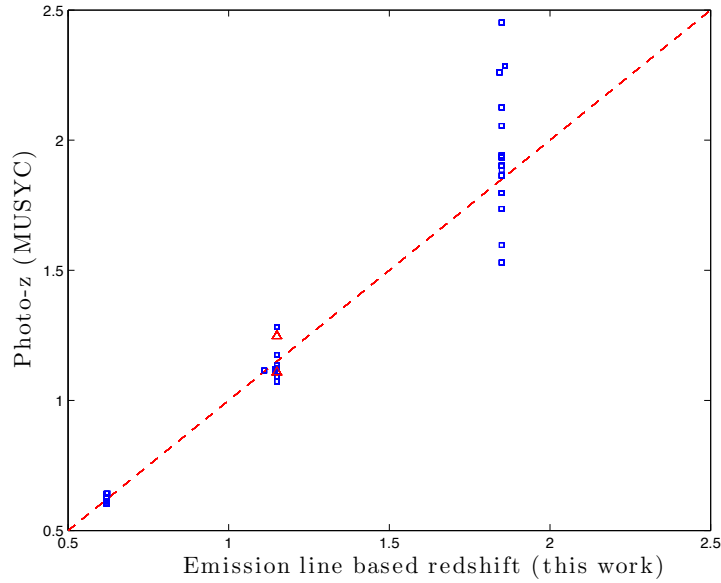

Figure 2.7:   Redshifts from the MUSYC survey versus redshifts from this work as listed in Table 2.1. Secure redshift assignments are indicated by blue squares and two "primary redshifts" by red triangles. The agreement with MUSYC redshifts is seen to be good in the mean, but the scatter of the MUSYC redshifts increases at higher redshifts.
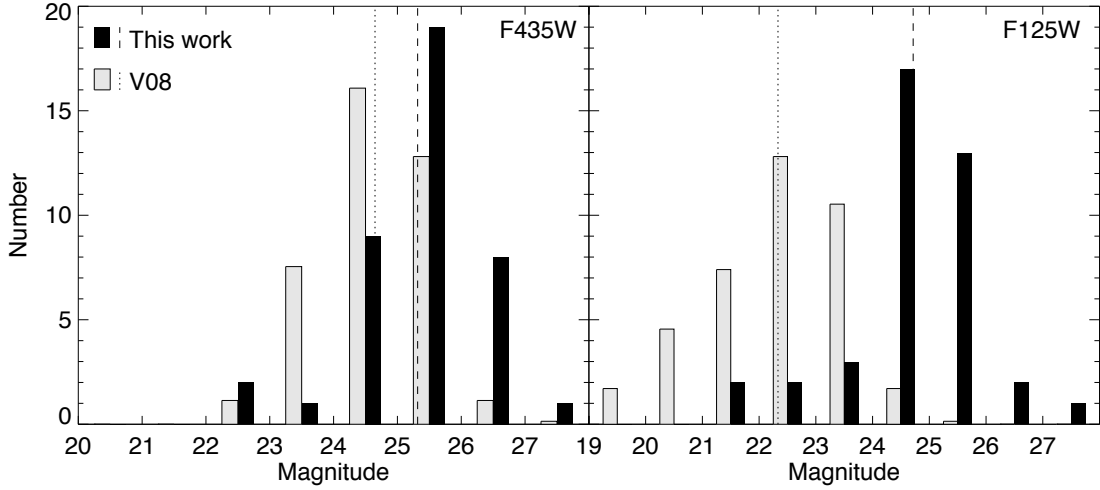
Figure 2.8: "De facto" broad band depth of our basic sample compared to the sample from (Vanzella et al. 2008) (V08), which is one of the deepest existing spectroscopic surveys. The comparison is done in two HST bands corresponding to B (left panel) and J (right panel). The medians of the samples are shown as dotted and dashed vertical lines. Comparing the medians, our sample is 0.8 and 2.3 magnitudes deeper than V08 in B and J, respectively. The height of the V08 histograms was divided by 7 for easy comparison.

we have extracted a complete spectroscopic sample from the catalogue of Vanzella et al. (2008) (V08 hereafter). The V08 survey targeted galaxies in the GOODS-S down to a limiting magnitude of $z_{850}(AB) = 26$, making it one of the deepest existing spectroscopic surveys (cf. Table 5 in Le Fèvre et al. (2015)).

From V08 we extracted all objects with redshift in one of our three redshift slices. To obtain a comparison sample of a good size we used slices of width 0.4, centred on the same redshifts, i.e. ± 0.2 around $z = 0.62$, 1.15, and 1.85. In Fig. 2.8 we show the distribution of two broad band magnitudes (F435W($\approx$B) and F125W($\approx$J)) for both our basic sample (black histogram) and the V08 sample (grey histogram). To make the studies consistent, we obtained the photometry from the G13 catalogue for all objects. It is seen that our sample is significantly deeper in both bands. The median of the comparison sample is 24.71 and 22.56 (B and J, respectively), while our sample has medians 25.49 and 24.92, that is, our sample goes around 0.8 and 2.3 magnitudes deeper.

In the overlapping region between our survey and the recent catalogue of HST grism spectroscopy (Morris et al. 2015), for example, our sample has 33 objects at redshifts probed by the HST spectroscopy ($z > 0.67$), but the HST catalogue contains only the seven brightest of them. The redshifts all agree.

2.4 RESULTS

2.4.1 THE MAIN SEQUENCE OF STAR FORMATION IN THREE NARROW REDSHIFT SLICES

The SED fits described in Sect. 2.3.2 also provide values for $M_\star$ and SFR of each galaxy. We list those values in Table 2.3, and in Fig. 2.9 we plot SFR vs $M_\star$. Both in the local universe and out to a redshift of 3.5, it has been shown that SFR forms a tight correlation with $M_\star$ (Brinchmann et al. 2004; Noeske et al. 2007; Maiolino et al. 2008), the so-called main sequence of star formation (MS). The MS has been shown to evolve with redshift, and in Fig. 2.9 we have overplotted the relations from the stacked radio data of star-forming galaxies reported in Table 2.4 of Karim et al. (2011) at each of the redshifts of our three redshift slices. From Karim et al. (2011) we take the mean of their $z = 0.4$–0.6 and 0.6–0.8 bins to represent $z = 0.62$, their $z = 1.0$–1.2 bin to represent $z = 1.15$, and their $z = 1.6$–2.0 bin to represent $z = 1.85$. Both the data and the relations are colour-coded according to a redshift slice as in Fig. 2.5. We also plot $\log(M_\star)=9.4$ which is the lower limit of the samples considered by Karim et al. (2011). One object (ELG14) turned out to provide unstable physical parameters in the sense that leaving out a single photometric point would severely change the output parameters. Upon checking the HST image, we noted a close neighbour galaxy of different colour, which presumably could have affected the photometry and caused this. The redshift is good so we keep it in the sample, but we exclude it from the analysis of the MS relation. We also exclude ELG30 from this analysis since we do not have a redshift for it. We use the primary redshift solutions for ELG66 and 75, but repeat the analysis using the secondary solutions. No significant difference is found using the secondary solutions (see Table 2.4).

From Fig. 2.9 we see that our data roughly agree with the relation from Karim et al. (2011), i.e. that there is a MS and that it evolves with redshift in the sense that galaxies of a given stellar mass have lower SFR at lower redshifts. Our data points are somewhat offset from the expected relations, but this could possibly be because our objects sample a much lower stellar mass range than the relations we compare them to. If the MS, for example, is steepening at the low-mass end, it would cause our low-mass galaxies to drop below the relations. To test this, we first assume that the slopes reported by Karim et al. (2011) at each of our redshift slices are correct for all masses, and then we determine the offsets to our data. The best fit offsets are shown as dashed coloured lines in Fig. 2.9 and provided in Table 2.4. We then remove the effect of redshift evolution in two different ways. First we assume that the evolution from Karim et al. (2011) is correct, and we apply a shift that brings all galaxies (and the relations) to what they would have been in the [OII] redshift slice (upper left panel of Fig. 2.10). We then fit a broken linear relation to the data points with the following two conditions: (*i*) at $\log(M_\star)$ larger than 9.4 it must have the slope of 0.59 (from Karim et al. (2011)) and (*ii*) it must be continuous in $\log(M_\star)=9.4$. The resulting best fit is shown in lower the left-hand panel of Fig. 2.10, and the best fit slope is found to be 1.31 with an rms of 0.31. In the two right-hand panels of Fig. 2.10, we show the same as in the left, only here we have applied redshift

Table 2.3: Physical parameters resulting from SED fitting with fixed redshift.

ID	log(mass)	log(SFR)	Redshift
ELG#	$logM_\odot$	$log(M_\odot/yr)$	fixed
3	9.01	0.06	0.619
4	8.63	0.45	1.144
5^c	9.12	1.41	1.86
6	9.04	1.13	1.86
9	8.15	-0.90	0.62
10	9.27	0.21	0.62
11	7.86	-0.91	0.62
12^c	10.21	2.38	1.843
14^c	8.67	0.76	1.85
15^c	9.12	1.58	1.85
16^c	9.87	1.52	1.85
20^c	8.92	1.20	1.85
21^c	8.89	1.07	1.85
22^c	9.40	1.84	1.85
23	8.74	0.74	1.85
25^c	8.86	1.33	1.85
26	8.85	0.36	1.15
28	8.28	-0.37	1.15
34	8.48	-0.63	1.15
35	9.41	1.27	1.85
36	8.31	-0.38	1.15
37	8.49	0.77	1.85
41	8.89	1.02	1.85
43	8.43	-0.29	1.15
45	8.50	-0.55	0.62
51	8.77	0.09	1.15
52	8.43	-0.62	1.15
53	9.61	1.47	1.85
54	9.06	1.53	1.85
55	9.29	1.49	1.15
58	8.68	-0.11	1.15
62	7.97	-1.09	0.62
65	8.61	-0.06	1.15
66^1	8.48	0.48	1.85
68	9.10	0.61	1.85
70	8.99	0.32	1.15
75^1	8.50	0.88	1.85
76	9.55	1.56	1.85
78	9.77	1.10	0.624
Ambiguous cases			
66^2	7.91	0.38	1.15
75^2	8.02	0.49	1.15
30^3	6.72	-1.15	0.62
30^3	7.31	-0.82	1.15
30^3	7.83	-0.39	1.85

[c] - Cluster member galaxy.

[1] - Primary fixed redshift solution used for ELG66 and 75.

[2] - Secondary fixed redshift solution used for ELG66 and 75.

[3] - No preferred redshift for ELG30, although $z = 0.62$ Hα is disfavoured.
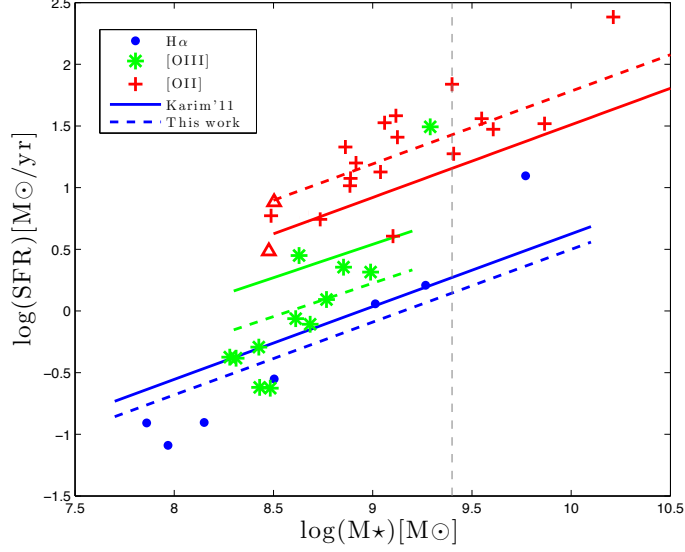
Figure 2.9: SFR vs stellar mass of emission line selected galaxies, colour-coded according to their redshift. The two red triangles mark objects with two redshift solutions (only primary solution shown). Solid lines show the relations reported by Karim et al. (2011). Dashed lines are the best fit of relations with the same slopes to our data. The vertical grey dashed line marks the lower mass limit of the Karim et al. (2011) sample.

correction shifts so that the dashed lines in Fig. 2.9 are lined up rather than the solid lines. In this case the best fit gives a slope of 1.02 with an rms of 0.29.

Table 2.4: Offsets of SFR($M_\star$) relative to Karim et al. (2011). The first 5 lines report the offset of individual redshift sub-samples assuming for each the slope found by Karim et al. (2011). The last two are best fit offset of the entire sample assuming now a slope of 1.17 for the galaxies with mass below the mass completeness limit ($10^{9.4} M_\odot$) of the Karim et al. (2011) sample. In both cases we repeat the fit using secondary redshifts for ELG 66 and 75 but no significant change is seen.

z	$N_{\rm obj}$	SFR offset	rms
0.62	7	-0.13 ± 0.16	0.35
1.15	12[1]	-0.33 ± 0.13	0.43
1.15	14[2]	-0.22 ± 0.16	0.52
1.85	19[1]	0.26 ± 0.07	0.27
1.85	17[2]	0.29 ± 0.07	0.27
All	38[1]	0.33 ± 0.05	0.32
All	38[2]	0.35 ± 0.06	0.34

[1] - Primary redshift solution used for ELG 66 and 75.
[2] - Secondary redshift solution used for ELG 66 and 75.
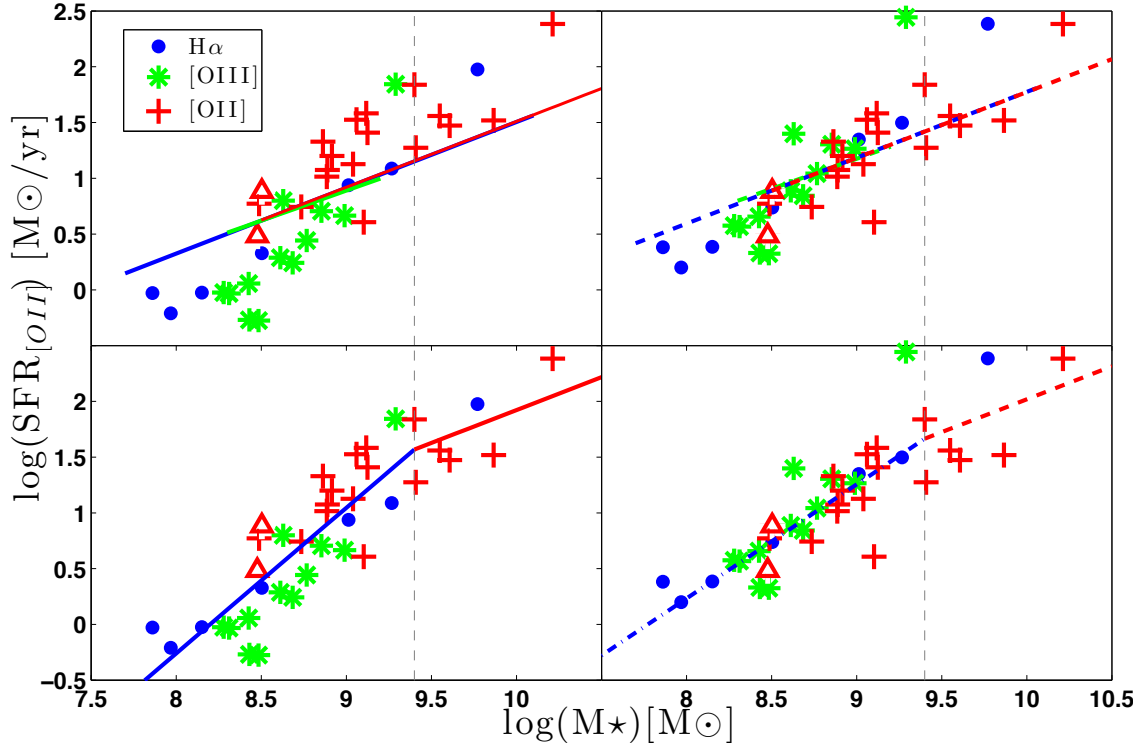
Figure 2.10: Upper two panels: the same data and relations as in Fig. 2.9. Here we have shifted each redshift slice to remove the effect of redshift evolution. In the left column we have applied shifts to bring the blue and green solid lines on top of the red (i.e. applied redshift corrections as reported in Karim et al. (2011)), in the right we did the same but used the dashed lines. In the lower panels we provide the best fit of broken MS relations. It is seen that under both assumptions, the relation steepens towards lower stellar masses.

Our sample reaches stellar masses 1.5 decades lower than the sample of Karim et al. (2011), and we see that in the range below their lower mass limit, our sample follows a significantly steeper MS, no matter how we correct for the redshift evolution. Previous analyses of the derived stellar masses from SED fits with exponential declining and increasing star-formation rates in a population of star-forming galaxies at z=1-2 have shown that the stellar masses vary within $\sim$0.1 dex (Christensen et al. 2012). As noted above, the offsets we reported in Table 2.4 may in this case be dominated by this steepening of the slope, and we therefore repeat the fit using a more realistic assumption. Rather than assuming a constant slope, we now use a slope with a break at $\log(M_\star)$=9.4. For the high-mass end we use the slope of 0.59 from Karim et al. (2011), and for the low-mass end we use the mean of the slopes we found above, which is 1.17.

The resulting best fit is shown in Fig. 2.11 and again reported in Table 2.4. We see that allowing for the change of slope, we now get a consistent positive offset towards higher SFR in all three redshift slices. This is no great surprise because one would expect samples selected by narrow-band techniques to select the objects with the strongest
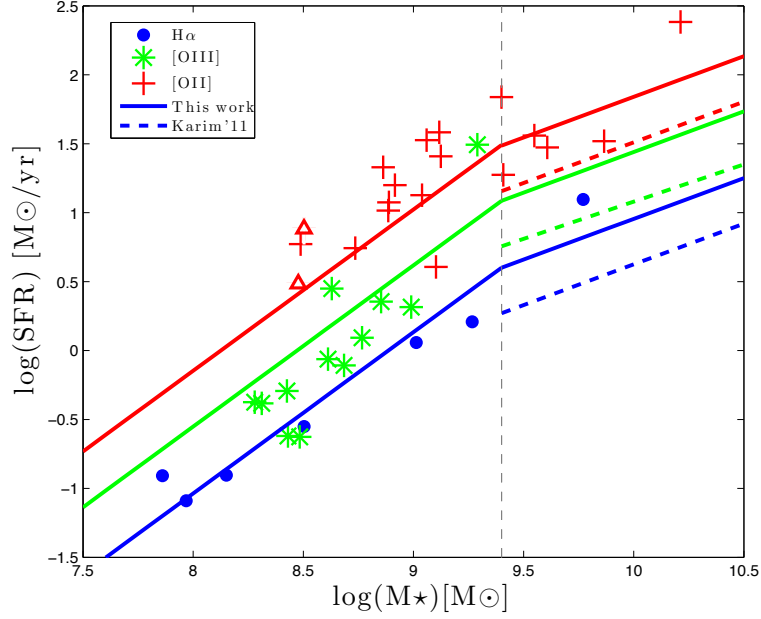
Figure 2.11: Similar to Fig. 2.9. Here we show only the Karim et al. (2011) fits (dashed lines) in the range above their lower mass bound. The full lines now show the best fit to our data of a "broken" MS with a steeper low mass slope.
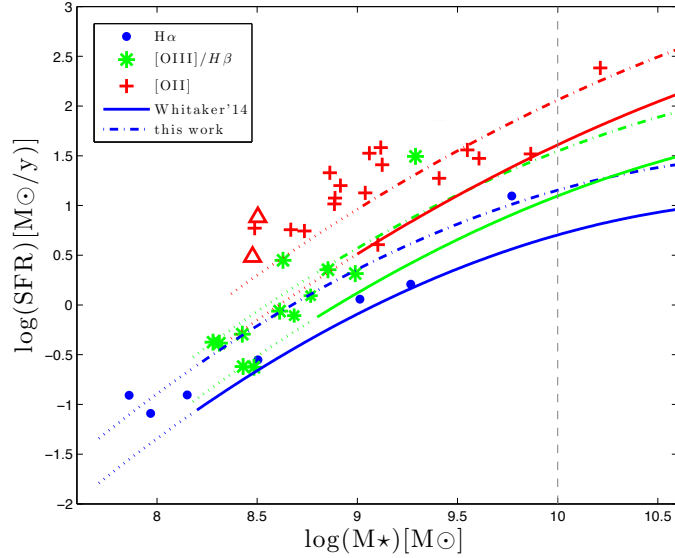

Figure 2.12: Similar to Fig. 2.11. Here we compare to the study by Whitaker et al. (2014) (solid lines), who also report a steepening towards low stellar masses. Their SFRs are seen to be lower, but adding 0.45 to their fits, we obtain a better fit to our data (dash-dotted curves). We do not see any evidence for shallower redshift evolution at low masses as they report. The dashed vertical line marks the division between their individual object (above 10^{10}) and stacked object (below 10^{10}) fits. Dotted curves are extrapolations of their fits where they had no data.

emission lines in any stellar mass bin, and consequently to contain the highest SFR galaxies of any mass at any redshift. In that sense our sample defines the upper envelope of the MS for low-to-intermediate-mass galaxies.

In conclusion to this section, we first tested that our sample was offset (up or down) in SFR compared to Karim et al. (2011) using their reported slope. We found an inconsistent scatter with both positive and negative offsets, but this could be because the median $M_\star$ is different in the three redshift slices. We then removed the effect of redshift to make them easier to compare and noted evidence that the slope is steeper at low masses. Assuming a steeper slope in the low-mass end we find that our data are consistent with a constant offset from the Karim et al. (2011) data (at 6.6σ) with an internal scatter of 0.32. Performing the same fit to the data, but instead using the constant slope of Karim et al. (2011) at all masses gives a zero offset with an internal scatter of 0.43, which is a significantly poorer fit even allowing for the one degree of freedom less.

Comparison with other studies

Whitaker et al. (2014) present MS fits from a study of galaxies in the CANDELS fields. At stellar masses larger than $\sim 10^{10}$ $M_\odot$ they use a UV+IR SFR indicator on photometry of individual photo-z galaxies, at lower stellar masses they do the same on stacked photometry and reach stellar masses of $10^{8.4}$ (at z=0.5) to $10^{9.2}$ (at z=2.5). Similar to our results of the previous section, they report a steepening of the slope at lower masses, but they fit it with a polynomial rather than a broken power law. They also report a shallower redshift evolution of the MS at lower masses than at high masses. Lee et al. (2015) also report a steepening of the MS below $M_* = 10^{10} M_\odot$, in agreement with our results.

We interpolated the polynomial fits of Whitaker et al. (2014) (their equation 2) to our three redshift slices and plot them with our data in Fig. 2.12. It is seen that the steepening is in good agreement with what we have reported, but the normalisation is again lower than our data. Also in Fig. 2.12 we show the Whitaker et al. (2014) models where we have added 0.45 to the log(SFR), which provide a better fit to our data, but it is seen that they find much less redshift evolution than seen in our sample. In particular we do not see any evidence of less evolution of the MS at low stellar masses, and our sample appears in stark disagreement with that result. We note, however, that our data are from SED fits to individual galaxies, while Whitaker et al. (2014) were fitting theirs to stacked data in the regime of comparison. Nilsson et al. (2011) performed a test fitting 40 emission-line-selected galaxies both individually and as a stack, and concluded that "Stacking of objects does not reveal the average of the properties of the individual objects". The difference could therefore be related to the stacking.

2.4.2 SFRs from SED fitting and from emission lines

From the NB magnitude we can calculate the emission-line fluxes since the flux density in the narrow band is equal to the sum of the emission line flux density and the continuum
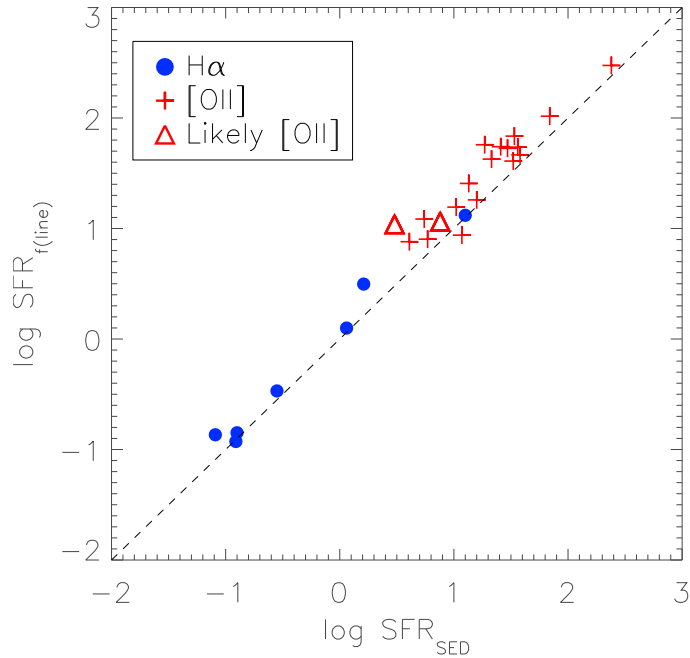
Figure 2.13: SFRs derived from the emission line flux plotted against the SFR values obtained from the SED fitting method. Symbol shapes and colours are similar to those in Fig. 2.9. The two methods show the offset of 0.19 ± 0.05 dex, which means that the values derived with two different methods are in excellent agreement for the entire sample.

flux density: $f_{\nu,NB} = f_{\nu,line} + f_{\nu,cont}$. For each galaxy, we derive the underlying continuum flux density from the best fit SED model by interpolating the flux density in adjacent 50 intervals blue and redwards of the NB filter. The continuum flux density is subtracted from the NB flux density taking the NB transmission curve into account. The derived emission line fluxes and equivalent widths (EWs) in the observed frame are listed in Table 2.1. The results are consistent if we choose to derive the continuum flux density by interpolating between the observed magnitudes in the ACS/F850LP and WFC3/F125W bands and assuming a power-law spectral slope between the bands.

For ELG 30, where we do not have a preferred redshift, the line flux for $z = 0.62, 1.15, 1.85$ is $3.17 \pm 0.16, 2.96 \pm 0.16, 2.97 \pm 0.16 \times 10^{-17} erg/s/cm^2$, and the EWs are $2011.4 \pm 106.4, 1851.6 \pm 97.9, 1969.8 \pm 104.2$. In Table 2.1 we list the value for $z = 1.15$.

Emission lines provide us with an alternative for measuring the SFR. We correct the emission line fluxes for intrinsic reddening using the best fit E(B-V) from the LePhare fits and a Calzetti extinction curve. We then calculate $H\alpha$ and [OII] luminosities, which are converted to a SFR using the calibrations in Kennicutt (1998), and we include a downward correction of a factor of 1.8 to correct from a Salpeter to a Chabrier IMF. The result is shown in Fig. 2.13, which demonstrates that there is excellent agreement between the SFRs derived from emission lines and from the SED fits. In fact the average offset in the SFR is just 0.19 ± 0.05 dex between the two different methods. Assuming a typical [NII]/$H\alpha$ ratio of 0.1 appropriate for low-mass galaxies, the emission line fluxes
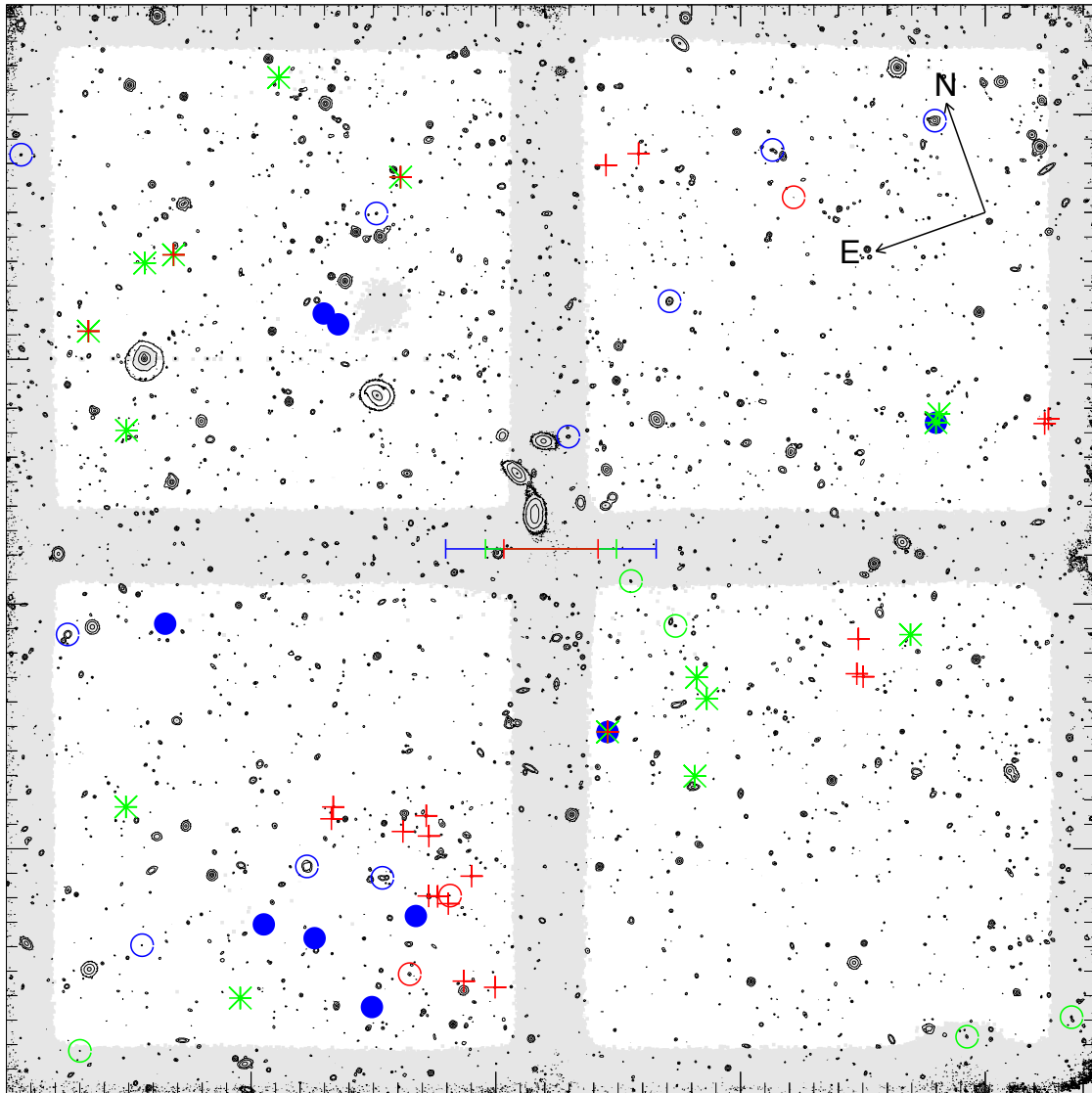
Figure 2.14: Objects identified in the three redshift slices overplotted on the narrow band image (black contours). Blue dots are $H\alpha$ emitters, green asterisks are [OIII]/$H\beta$, and red crosses represent the [OII] emitters. Lower S/N areas of the image that were excluded from the basic sample are shaded in grey. Multiple symbols that are over-plotted represent galaxies with multiple redshift solutions. Open circles represent galaxies from the "extended sample". Bars of length 1 comoving Mpc at the given redshift is over-plotted in the centre of the image with same colour-coding as for the objects.

and the blue points in Fig. 2.13 will have a downward correction of 0.05 dex. By Including this correction, the offset between the emission line derived SFRs and the SED SFRs is 0.17 ± 0.05.

2.4.3   Clustering and large scale structure in three narrow redshift slices

In this section we consider the extended sample of 58 objects in three redshift slices. In Fig. 2.14 we plot the objects in the three redshift slices overlaid on our narrow band image (in black contours). In this figure we also show the masked lower signal-to-noise regions (shaded grey). The same field covers different physical scales and different comoving scales in the three redshift slices. In Fig. 2.15 we again plot the three slices separately, but here we have scaled them all to the same comoving scale. We subsequently found that the z=1.84 cluster has been discovered independently in a study based on CANDELS and 3D-HST spectroscopic redshifts in the field (Mei et al. 2015). We refer the reader to this work for further discussion of this interesting structure.

One feature that is immediately visible is the concentration of [OII] emitters in the lower left-hand quadrant. In section 2.4.1 we found that the [OII] emitter sample on average has higher mass than galaxies in the other slices, so because high-mass galaxies are known to cluster more strongly than low-mass galaxies, this is indeed the slice where we would be most likely to find a galaxy cluster. In Fig. 2.15 we have drawn a circle with a diameter of 2.55 comoving Mpc, which encloses 13 of the 23 [OII] emitters in our extended sample. We also labelled the position of the highest mass galaxy in our sample, and it is seen to fall very close to the centre of the circle. From Fig. 2.14 we see that there is indeed evidence of higher density of both optical and X-ray sources (Xue et al. 2012) around the position of the clump of [OII] emitters. Computing the surface density of galaxies inside the circle, we find 2.5 per comoving Mpc^2, while outside of that it is 0.08 per comoving Mpc^2. On the basis of the observations reported above, we here conclude that we have identified a galaxy cluster at $z = 1.85$ in our [OII] redshift slice.

Simulations of early galaxy and structure formation all share a common prediction that the first structures to form are filaments whose ends are connected in nodes. Young low-mass galaxies form in the filaments, and while they assemble further and grow, they also drift along the filaments into the nodes where they form galaxy groups and eventually clusters (Monaco et al. 2005). Samples of high-mass galaxies are therefore strongly clustered and well suited to identifying the nodes as we showed in the previous paragraph, but to identify filaments one needs samples of lower mass galaxies covering volumes large enough to cover the expected sizes of filaments (20-25h^{-1} Mpc), (Demiański & Doroshkevich 1999). The end product of the evolution of this cosmic web has been well studied at low redshift, and recently a large catalogue of filaments in the redshift range $z = 0.009 - 0.155$ has been published Tempel et al. (2014), but at higher redshifts than 0.155 this becomes much very difficult. Warren & Møller (1996) argued that Lyα emission-line-selected galaxies have lower masses than continuum-flux-selected samples,
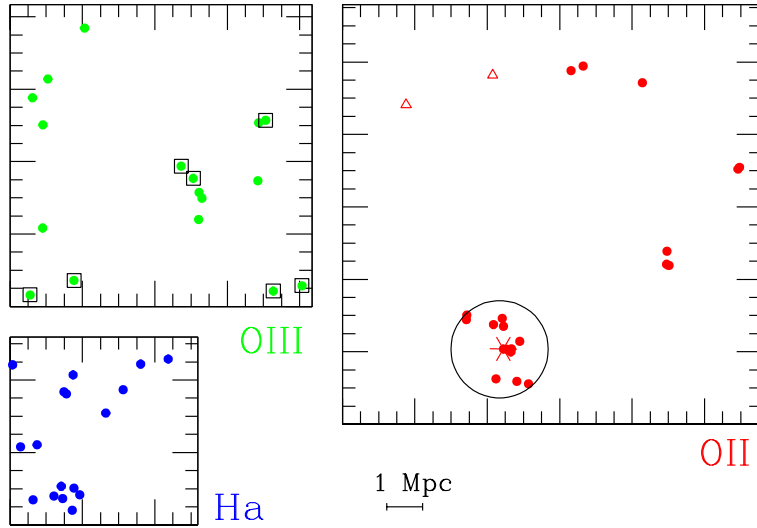
Figure 2.15: Objects detected in the three redshift slices shown separately and scaled to the same co-moving scale. The colour coding is as in previous figures: dots denote certain redshifts from the extended sample, and open triangles indicate primary redshifts for the two uncertain cases. Open black squares indicate objects with known spectroscopic redshifts in the [OIII] slice. The red star in the [OII] slice marks the galaxy with the highest $M_\star$, and the large black circle the cluster centred on it at z=1.85.

and suggested that they could be used to identify filaments. Møller & Warren (1998) showed on a statistical basis that Lyα emitters do tend to line up in strings. Nevertheless, the actual mapping of filaments is hampered by two problems: mostly the observed volumes are too small, and there is usually no follow-up spectroscopy, which is required to provide the 3-D mapping of the volume.

In one case a fully resolved filament mapped in Lyα was identified at z=3.04 (Møller & Fynbo 2001) where a total of eight objects were found to be enclosed in a cylinder with proper radius 400 kpc which in the cosmology we use here also corresponds to 400 kpc. In Fig. 2.15 we see that 10 out of 17 galaxies at $z = 1.15$ lie close to a line going almost diagonally from the lower left-hand corner of the field towards the upper right. This could be a chance alignment of galaxies at mixed redshifts, but it could also be a filament seen under some inclination angle. As in the work by Møller & Fynbo (2001) our field is too small to identify a filament that lies in the plane of the sky, we would see too few objects in such a small filament section. To test that we do indeed have enough 3-D information, we also in Fig. 2.15 indicated those objects in the [OIII] slice for which we have spectroscopic redshifts, and we see that we have five spectroscopic redshifts covering the entire length of the diagonal.

In Fig. 2.16 we again plot the objects in the [OIII] slice, but here on proper length scale and with the redshifts of the five galaxies on the diagonal line marked. We see that the redshifts in general grow from the upper right towards the lower left, so this does indeed appear to be a filament pointing from the upper right towards the lower left away
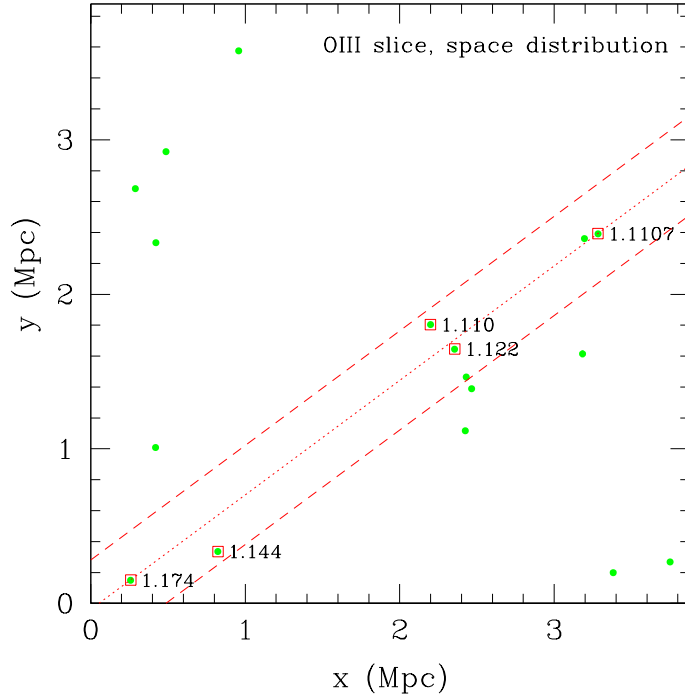
Figure 2.16: Objects detected in the [OIII] slice but now at proper scale. The red dotted and dashed lines provide the size scale of the filament of emission line galaxies at $z = 3.04$ reported by Møller & Fynbo (2001). Also we show the spectroscopic redshifts of five galaxies that may outline a similar filament at $z = 1.15$ in this field.

from us. To compare this to the previously reported Lyα filament, we have indicated the width (400 kpc) of that filament on top of this one, and all five objects are seen to fit well within this cylinder in this projection. The availability of spectroscopic redshifts allows us to also compute the arrangement of the objects along the line of sight.

The [OIII] redshift slice is thicker than the other two slices because we have three individual lines ([OIII] 5007, [OIII] 4959, and Hβ) here, either of which could fall into the narrow pass band. We visualise this in Fig. 2.17 where we have kept the field y-axis of Fig. 2.16, but have turned the volume 90 degrees and replaced the x-axis by the z-axis (i.e. redshift converted to proper distance). The three dotted boxes here represent the volumes sampled by each of the three emission lines, green dots are the galaxies, and the diagonal dashed lines again mark out a filament of thickness as in Fig. 2.16. We see that the first four galaxies would indeed fit into a straight, cylindrical filament of this thickness, but it would be somewhat longer than the Lyα filament at redshift 3.04. The last galaxy seen in Hβ may well belong to the same filament, but it would have to be bent or thicker in that case. The length of the filament is in excellent agreement with the detection of the Lyα filament at $z = 3.01$ reported by Matsuda et al. (2005) and the recent work at low redshifts Tempel et al. (2014).
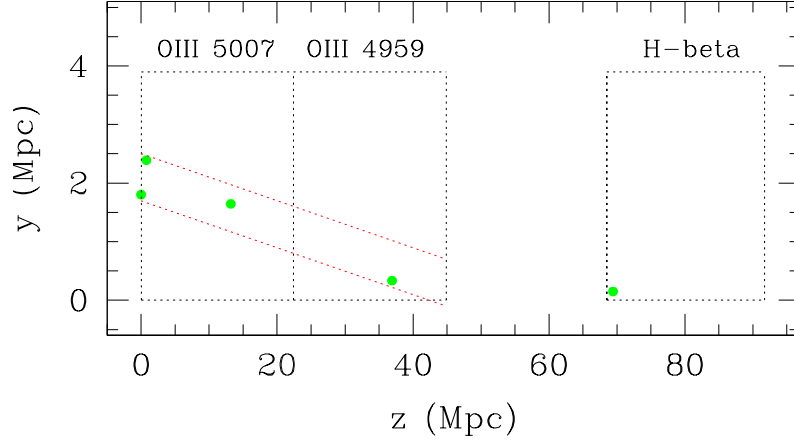
Figure 2.17: Similar to Fig. 2.16 but with converted redshifts to proper distance. We show the projection onto the (y vs distance) plane. For comparison we again indicate a filament of the same proper width as in Fig. 2.16. The [OIII] slice covers a *z*-range about four times wider than the other slices because of the three emission lines. Selection by each of the three lines is indicated by the dotted lines.

In conclusion, we have shown that emission line selected galaxies at those redshifts are well suited to performing observational tests of simulations of a large scale structure. The Hα field size is in this case too small, but surveys over larger fields like UltraVISTA (McCracken et al. 2012; Milvang-Jensen et al. 2013) will provide fields of sufficient size. The [OII] slice has a larger volume, and in general the [OII] selected galaxies have higher mass than the lower redshift slices, making the [OII] slice ideal for rich group and cluster statistics. The [OIII] slice is extremely well suited for filament searches because the depth allows to identify filaments at any inclination angle. This promises that it may soon be possible to perform the alternative and "purely geometrical" cosmological test and determine Ω_Λ using filaments as described in detail by Weidinger et al. (2002). Identifying filaments require spectroscopic redshifts, or some other diagnostic for more accurate redshift determination. One such novel method using only VISTA narrow band data has recently been described (Zabl et al. in preparation).

2.5 DISCUSSION AND CONCLUSIONS

2.5.1 GALAXY SCALING RELATIONS AT LOW MASSES

Understanding the scaling relations of galaxies of all masses is fundamental to understanding galaxy formation and evolution. Nevertheless, galaxy samples selected in all emission bands ranging from X-rays, through UV, optical, IR, sub-mm, and mm, to radio, all form flux-limited samples of galaxies that are the most luminous, and presumably the most massive, of their kind. Such samples are, by definition, the easiest to obtain,

and normally large portions of our knowledge of high-redshift galaxies come from such samples. However, to explore the low-mass range of galaxies, notably at high redshifts, other selection techniques are required. One such technique is emission line selection via deep narrow and broad band imaging.

We are involved in several narrow/broad band imaging surveys, and in this paper we reported on a pilot project to study the feasibility of using them to trace low-mass galaxy scaling relations and their redshift evolution. Simple narrow/broad emission line selection allows galaxies to be selected with strong emission lines, thereby providing a deepening of the flux-limited samples, and here we have specifically chosen a broad-narrow-broad selection that results in a selection of the highest emission-line equivalent width galaxies. Two simple predictions for a study of this kind would be

(*i*) that our sample in the mean could have higher SFR for any given galaxy stellar mass, and

(*ii*) that our sample in the mean will select galaxies down to lower stellar masses than continuum flux-limited samples.

We carried out a detailed comparison of our data set to previous studies and find that both of those predictions have been confirmed. We thus provide an "upper boundary" to the main sequence of star formation (MS) at each of the three redshifts we studied.

Our comparison to previous work also shows that the MS has a significantly steeper slope at the low-mass end (below $M_\star = 10^{9.4}$) than at higher masses.

2.5.2 NARROW BAND SELECTION AS COSMOLOGICAL TOOL

Any narrow/broad band survey carried out at a wavelength in excess of the rest wavelength of Hα provides a roughly even coverage of three widely separated narrow redshift slices corresponding to the redshifted wavelengths of Hα, [OIII]/Hβ, and [OII]. A few additional species at other wavelengths will also appear on occasion, but only rarely, owing to the much weaker strength of their transitions. The exact ratio of detected objects between the three main slices depends on their relative equivalent widths (as a function of redshift), their relative number density (as a function of redshift), and the ratio of the surveyed volumes (as a function of narrow band wavelength and assumed cosmology).

We surveyed comoving volumes of 1221 Mpc^3 (Hα), 3092 Mpc^3 ($\times 3$ due to Hβ, [OIII]$\lambda 4959$, and [OIII]$\lambda 5007$), and 5536 Mpc^3 ([OII]). Down to our conservatively chosen narrow-band AB magnitude limit of 24.8, they are distributed in the following proportions: Hα emitters 20%, [OIII]/Hβ emitters 30%, and [OII]-emitters 50% (see Fig. 2.4). We compared our redshifts to previous photo-z redshifts from the literature and showed that narrow band selection allows a much more accurate redshift assignment, notably in the highest redshift slices. The errors on redshift assignment from photo-z will propagate into errors on the physical parameters ($M_\star$ and SFR), so that smaller, but more accurate, samples of narrow-band-selected galaxies will provide checks of whether the propagated errors simply add scatter or if they add systematic effects.

We showed that the galaxies can be classified fairly robustly based on two broad band

colours (Fig. 2.5), confirming the earlier study by Bayliss et al. (2011). Therefore, we conclude that emission-line selected galaxies do indeed split into the evolutionary groups according to their colour. In Fig. 2.9 we see that the galaxies in our lowest redshift slice have on average the lowest masses and that galaxies then become progressively more massive at higher redshifts. This could possibly be related to the selection via different emission lines in the three slices, but is more likely a result of using the same observed magnitude limit for all slices. One very interesting thing to note is that we are able to select star-forming galaxies of stellar masses down to $10^{8.5} M_\odot$ at a redshift of 1.85, and well below the masses in the other two slices. With emission-selected samples, it is very difficult to study low-mass galaxies beyond the critical redshift of "cosmic high noon" at z=2.5, but absorption-selected galaxy samples and samples selected as gamma ray burst host galaxies (GRBs) have been shown to reach much lower masses (Møller et al. (2013); Christensen et al. (2014); Arabsalmani et al. (2015)). Therefore, to be able to connect absorption and GRB-selected samples (with median $M_\star$ of $10^{8.5} M_\odot$) with continuum-emission-selected samples at high redshifts, it is important to create well-studied samples with a wide overlap in stellar masses. Absorption-selected galaxies are in general more easily identified via line emission than via continuum emission (e.g. Weatherley et al. 2005; Rauch et al. 2008; Fynbo et al. 2010, 2011, 2013), and the ongoing UltraVISTA (McCracken et al. 2012) narrow-band survey covering ≈ 0.8 deg^2 at slightly higher redshifts (for Hα: z=0.815, for [OIII]/Hβ: z=1.38/1.45 and for [OII]: z=2.19) will create a large sample of low-mass emission-line-selected galaxies in those three slices (Milvang-Jensen et al. 2013). The UltraVISTA sample will be well suited to connecting the current flux-limited galaxy samples out to the highest redshifts (z=6-8) currently explored by DLA galaxies and GRBs.

One of the objectives of this paper was to derive more robust forecasts of what will be found in ongoing or upcoming deep surveys, in particular the UltraVISTA survey (McCracken et al. 2012; Milvang-Jensen et al. 2013). The UltraVISTA survey uses a slightly redder narrow-band filter centred at 1.19μm (Milvang-Jensen et al. 2013), but this difference is small enough that evolutionary effects on the population of $z < 2$ emitters (Hα, [OIII]/Hβ and [OII]) should be small. We can thus make forecasts of which numbers of the most common types of such emitters we expect to find in the UltraVISTA survey based on the present work. After scaling with the area, we expect to detect $\gtrsim 1000$ of each of the Hα, [OIII], and [OII] emitters. Given the large area of the UltraVISTA we predict that we will find more rare line emitters that are not represented in the more than 70 times smaller area sampled in the present work.

2.5.3 STRUCTURE FORMATION TRACED BY EMISSION-LINE-SELECTED GALAXIES

In Fig. 2.11 we show that objects in the [OII] slice on average have higher masses than in the other two slices. As argued by Møller & Fynbo (2001) and Monaco et al. (2005), the lowest mass galaxies at any redshift are the best candidates for mapping out the

filamentary structure of the cosmic web, while the higher mass galaxies will be more clustered around the nodes of the web and could thus mark the sites of early cluster formation.

In this paper we have pursued their line of thought and identified a galaxy cluster (or proto cluster) at $z = 1.85$. The cluster has an elliptical shape as predicted by N-body simulations and has no extended X-ray emission, so it is probably in its early stages of formation. The galaxy with the highest mass of our entire sample lies in the centre of the forming cluster and has been identified as an X-ray emitter. This makes this galaxy especially interest since it is a very good candidate for the pre-stage of a central cluster cD galaxy.

Secure identification of filaments is more difficult since it requires even better redshift determinations than the narrow band data alone can provide. We identified a possible filament that lies diagonally across the field of the [oIII] slice, and enough of the objects had known spectroscopic redshifts for a 3D mapping. The candidate filament has width and length in good agreement with simulations and with the previous detection of Møller & Fynbo (2001). Obtaining a few more redshifts would be good in order to securely confirm the identification, but detecting a forming cluster and a likely filament are examples of the strong potential of tracing the formation of structure in the early universe with deep narrow band data.

3

WHAT FAINT GALAXIES WHISPER

Pushing the magnitude boundaries in GOODS South

Ia Kochiashvili[1], Johan P.U. Fynbo[1]

[1] Dark Cosmology Centre, Niels Bohr Institute, University of Copenhagen, Juliane Maries Vej 30, 2100 Copenhagen, Denmark

Abstract

We present the results of a multiband photometric study of emission-line galaxies in the GOODS South field selected in deep narrow-band imaging obtained with the HAWK-I instrument mounted on the ESO Very Large Telescope. The narrow-band filter used is the NB1060 filter centred at 1060 nm in the Y-band. This is a follow-up of a study where we used a colour-colour selection technique to select emission line galaxies down to a narrow-band magnitude level of 24.8 (on the AB system). The current extension of that sample has been selected using a more traditional color-magnitude selection and the goal has here been to achieve the maximum magnitude depth possible.

90 galaxies have been investigated in total down to a magnitude limit of about 25.6. These galaxies have photometric redshifts consistent with either $z = 0.6$, $z = 1.15$ and $z = 1.85$ corresponding to $H\alpha$, [OIII]/$H\beta$ or [OII] emission-lines falling in the NB1060 filter.

We investigate the M_* vs SFR relation and confirm that the steepening of the slope at the low-mass end, which we found in paper I, holds also here with a sample that is more than twice as large in size and more importantly extend to lower masses. We compare the results of the two different selection methods (colour-colour vs. colour-magnitude) and discuss the differences between them.

3.1   INTRODUCTION

Selecting and studying properties of low-mass galaxies with $M_* < 10^{10} M_\odot$ is comparatively easy using narrow-band selection of emission-line galaxies (ELGs). This is because the selection is not directly dependent on the broad-band continuum emission, which coming from stars correlates directly with the stellar mass. The emission lines on the contrary can have very large equivalent widths meaning that galaxies with much less stellar emission can be selected for further study.

It has become increasingly clear that galaxies obey a correlation between stellar mass and star formation – the so-called main sequence of star formation (e.g., Daddi et al. 2007). Samples of ELGs make it possible to explore the low-mass end of this main sequence of star formation, letting us probe the validity of empirical relations derived with different selection methods and converge on a more complete mapping of the formation and evolution of the baryonic content in galaxies. In Kochiashvili et al. (2015) (paper I from here on) we described an extensive study of ELGs selected by a colour-colour selection technique and limited to a magnitude limit of $\mathrm{m_{NB}} < 24.8$. The motivation for limiting the sample magnitude in paper I was that 24.8 is the expected narrow-band depth of the UltraVISTA survey (e.g., Milvang-Jensen et al. 2013; McCracken et al. 2012) and a goal of paper I was exactly to characterize the interloper-populations to be expected in the UltraVISTA survey. The main results of paper I were *i)* the selection of 40 ELGs, which from spectroscopic redshift measurements based on the extensive set of broad band imaging available for the GOODS fields are estimated to be 20% Hα emitters at $z = 0.62$, 30% Hβ/[OIII] emitters at $z = 1.15$ and 50% [OII] emitters at $z = 1.85$, *ii)* we confirm that ELGs selected in this way can be fairly robustly classified simply based on $v - i$ and $z - J$ colours (consistent with earlier work by Bayliss et al. 2011), *iii)* an apparent steepening of the main sequence of star-formation below a stellar mass of about $\log(M_*) = 9.4$, and *iv)* the detection of large scale structure in the spatial distribution of the ELGs. Motivated by this study we here wish to explore the data set further by pushing the sample to a fainter flux limit. Thereby we may strengthen the evidence for a steepening of the main sequence of star-formation and explore it to fainter mass limits. In addition we will of course trace the large scale structure better with more galaxies.

Throughout this project, we again assume a flat cosmology with $\Omega_\Lambda = 0.70$, $\Omega_m = 0.30$ and a Hubble constant of $H_0 = 70$ km s^{-1} Mpc^{-1}.

3.2   SAMPLE SELECTION

The method that we use in paper I relies on selecting galaxies according to their position in a colour-colour diagram based on the two broad-bands and one narrow band Y, J and NB1060 (for further details see paper I). In this study, we adopt a more traditional magnitude-colour selection method instead of the colour-colour selection. Dropping the magnitude limit of 24.8 in the narrow band will allow us to probe the fainter end of the selection into further detail and therefore study the low-mass end of the mass-SFR
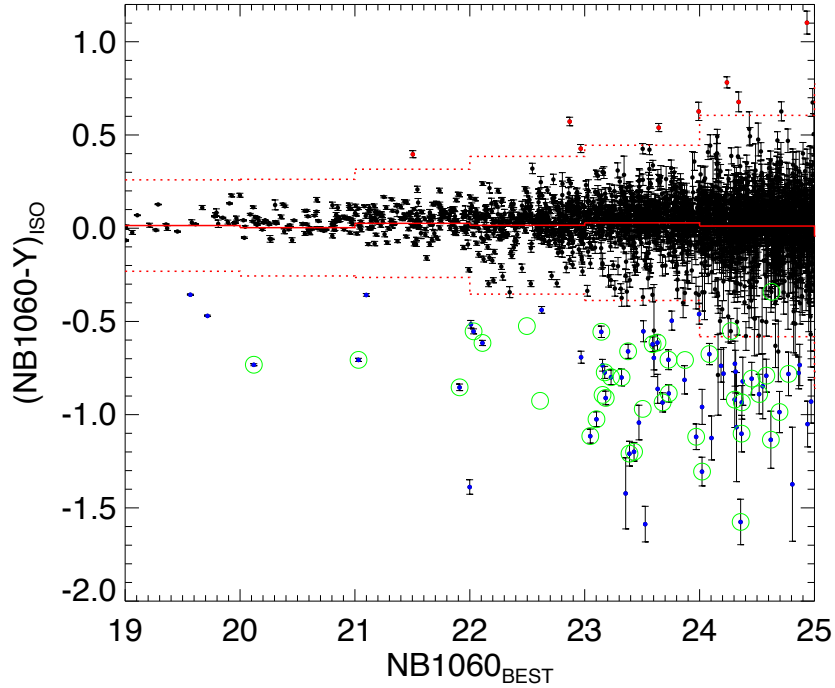
Figure 3.1: The colour vs magnitude selection of candidate ELGs. The distribution is divided into bins of 1 mag length in NB1060 magnitude. Red solid line marks the centre and the dotted red lines mark the 5σ edges of the distribution in each bin. Every object more than 1σ below the 5σ threshold is a candidate ELG (blue dots). The negative colour corresponds to flux excess in the NB1060 filter; the positive colour excess on the contrary, corresponds to the decrease of flux in the NB1060 filter (Red dots). Green circles mark the candidates from paper I. The cases where green circles are empty, are the cases of "disappeared" candidates (i.e., the candidates that are present in paper I, but are absent here due to non-zero flags as discussed in the text).

relation. The main question to answer in this study is whether the steepening of the M_* vs. SFR relation below $M_* = 10^{9.4} M_\odot$ that we found in paper I, (e.g. in their Fig. 12) is still present when the sample is extended below 24.8.

An additional difference in this new study compared to the work in paper I regards the use of masking. In paper I we created a mask file to block the bad pixel areas and detector edges of the detection images (NB, Y and J). We decided to drop the masking in this study because in paper I we saw that adopting masking caused us to leave out good ELG candidates that happened to be located in the noisy areas representing the edges of the detectors, but have very strong flux and are important to retain as part of our sample. This said, we now proceed to explain in further details what has been done and found in this project.

The first step is the candidate extraction from the fits images. This was done using the same method described in paper I with SExtractor (Bertin & Arnouts 1996). A total of 3990 objects were found in the images and extracted.

For candidate selection, we use the following procedure. We divide the sample into bins of NB1060 magnitude (1 mag bin size) and fit a Gaussian to the colour distribution of the continuum sources in each bin. The continuum sources are distributed into a "cloud"; objects that are in the 5σ wings of the distribution, have either flux excess or flux deficit in the NB1060 filter. Those with excess flux in the narrow band, i.e. with a negative N-Y colour and out of the 5σ wing are potential candidate emission-line sources. The objects with positive colour are left out, but it could be interesting to study the nature of these objects and see what kind of sources they are.

In order to study the candidates further, we select them according to the flux excess value and also the SExtractor flags. The objects that have SExtractor flag value of 0, are selected for being candidate ELGs and are adopted for further study. [1]

The reason for only including objects with flag=0 is that we wanted to be conservative and to avoid objects for which the photometry could be affected by light from bright neighbours, since obtaining robust physical properties of candidates is very important for this study. However, despite the conservative selection parameters, we still have to make sure that none of the selected objects are due to noise or are selected as NB excess due to being bad pixel regions, spurious objects etc. The first step in testing this, is to identify them in the CANDELS catalogue (Guo et al. 2013) (G13 hereafter). 75 out of 87 candidates are present in G13 and are selected for further study. The remaining 12 candidates are re-checked to make sure none of the excluded candidates are real objects. We had to reinstate one of the objects from the excluded list, because it appears to be a real object that has no photometric data in the G13 catalogue. All remaining 11 cases are due to noise close to the image edges. For the extra object, we have performed aperture photometry. Since the aperture photometry is not as robust as G13 photometry, the object will not be included in the further studies, but will just remain in Table 3.1 as an extra entry. It is worth mentioning though, that the aperture photometry has been successful enough to form the bases of a robust determination of a photometric redshift for this candidate.

After a second iteration of tests, we had to exclude three more objects from our sample. These were three bright stars that have been misselected as NB excess objects due to saturation effects. Overall, 72 candidates were left for further study. We next cross-matched with the candidates from our previous study (see paper I); 33 out of 40

---

[1]Concerning SExtractor flagging: the value of "0" means that the object is well isolated from its neighbours and has no damaged pixel areas; the value of "1" means that the object has a bright neighbour nearby whose flux can blend with the candidate; the flag value of "2" means that there is at least one pixel damaged in the area of the object, etc. The final SExtractor flag values for each source are added up and calculated according to these individual flags. this means that if the object has a flag value of 3, than there is a bright neighbour nearby the candidate and also there is at least one damaged pixel that may cause flux value to be wrong; therefore, the final flag value is calculated to be "1+2"=3, etc. For further details on flagging, we refer to the SExtractor manual (Bertin & Arnouts 1996).

objects from paper I were identified and given the same numbering as before (see Table 1). All new cases have been numbered with first number after last ID# in paper I and above (i.e. the first new candidate in this selection is named as "ELG79", the second - "ELG80", etc.). Further comparison with the "extended sample", shows that 7 candidates are present in Table 2. These candidates are marked with asterisk in Table 3.1.

Thumbnail images in the NB, Y and HST v bands for all new candidates can be inspected in appendix B.

3.3 Results

3.3.1 Candidates from paper I not included in the new selection

As mentioned above, seven out of 40 candidates from the "basic sample" and 12 out of 19 candidates from the "extended sample" of paper I are are not recovered in the new selection.

After examining their SExtractor flags we find that five out of seven "basic sample" objects from paper I have flags of 2 or 3. The same explanation applies to five "extended sample" objects. All other candidates from both samples have a flag of 0. However, these objects have a too weak colour excess for given magnitude bin to pass the selection threshold adopted here.

3.3.2 Spectroscopic redshifts

We next queried the NED/IPAC[2] and SIMBAD (Wenger et al. 2007) databases to find spectroscopic redshifts for our candidates and found that four of them have robustly measured redshifts. The results are included in the Table 3.1. No additional spectral data has been obtained.

3.3.3 SED fitting and photometric redshifts

We have used the LePhare code (Ilbert et al. 2006; Arnouts et al. 1999) to fit the SEDs and to derive photometric redshifts. We adopted the same procedure as in paper I and refer to that paper for details. In this way we ensure that the results are consistent and can be combined into one overall sample. Here, as well as in paper I, we use the photometric data from the G13 catalogue (Guo et al. 2013).

We first look into the $v - i$ vs. $z - J$ colour-colour distribution of our candidates in the same manner as in paper I. We find that the galaxies do indeed still overall fall in the same three clumps occupied by Hα emitters, Hβ/[Oiii] emitters and [Oii] emitters.

We ran LePhare in two different setups: with and without NB and Y-band data points to check if the output of SED fitting was dependent on the presence of the emission-line

---

[2]The NASA/IPAC Extragalactic Database (NED) is operated by the Jet Propulsion Laboratory, California Institute of Technology, under contract with the National Aeronautics and Space Administration.

Table 3.1: In this table we provide essential information on the candidate ELGs. In the first column we present the ID numbers of the new candidates. In the second column we list RA & Dec of the candidates. Third and fourth columns are the $NB1060$ magnitudes and colours ($NB1060 - Y$) and corresponding errors. Fifth column is the redshift that we obtain in this study. Columns 6 and 7 are the peak (best) and 1σ minimum and maximum redshift values found in the MUSYC catalogue (Cardamone et al. 2010). Column 8 lists the line identifiers and in the final column we provide the references to the spectroscopic redshift (if present).

ID	RA & DEC	NB	$NB - Y$	Redshift	z[Peak]	z[min/max]	line ID	Ref
$ELG\#$	(2000.0)	mag (AUTO)	mag (ISO)	This work	MUSYC	MUSYC		
79	03:32:19.39 -27:49:30.09	24.32 ± 0.14	-1.07 ± 0.29	1.85/1.15	–	–	[OII]/[OIII]	
80	03:32:28.82 -27:48:29.69	23.60 ± 0.05	-0.70 ± 0.06	1.85			[OII]	
81	03:32:51.52 -27:46:44.37	24.38 ± 0.09	-0.82 ± 0.13	1.1456	1.73	1.26/2.28	Hα/[OIII]	(1)
82	03:32:23.12 -27:48:49.25	23.51 ± 0.05	-0.55 ± 0.06	1.85	–	–	[OII]	
83	03:32:18.62 -27:48:46.07	25.09 ± 0.12	-1.19 ± 0.24	1.85	1.35	1.14/1.57	[OII]	
84	03:32:41.43 -27:46:51.44	21.10 ± 0.01	-0.36 ± 0.01	0.62	0.63	0.62/0.64	Hα	
85*	03:32:46.75 -27:46:24.00	24.86 ± 0.06	-0.78 ± 0.08	0.625	0.59	0.57/0.61	Hα	(2) (3)
86	03:32:17.11 -27:48:23.13	24.21 ± 0.08	-0.78 ± 0.14	1.85	2.09	1.98/2.17	[OIII]	
87*	03:32:40.78 -27:46:15.68	19.57 ± 0.01	-0.36 ± 0.01	0.6218	0.69	0.67/0.70	Hα	(2)
88	03:32:49.59 -27:45:48.35	23.64 ± 0.05	-0.86 ± 0.08	1.15	1.07	1.03/1.09	[OIII]/Hβ	
89	03:32:33.42 -27:46:29.35	25.44 ± 0.14	-1.36 ± 0.30	1.85/1.15	2.16	1.55/2.65	[OII]/[OIII]	
90	03:32:45.03 -27:45:30.73	25.09 ± 0.06	-1.09 ± 0.14	1.15/0.62	–	–	[OIII]/Hα	
91	03:32:31.89 -27:46:20.59	23.53 ± 0.03	-1.59 ± 0.10	1.85/1.15	1.42	1.14/1.77	[OII]/[OIII]	
92	03:32:31.04 -27:46:10.27	22.00 ± 0.01	-1.39 ± 0.04	1.125	1.15	1.14/1.17	Hα/[OIII]	(4)
93	03:32:33.38 -27:45:12.69	25.31 ± 0.10	-1.17 ± 0.19	1.15	–	–	[OIII]/Hβ	
94*	03:32:26.77 -27:45:30.54	22.97 ± 0.02	-0.69 ± 0.03	1.122	1.11	1.09/1.13	[OIII]/Hβ	(5)
95	03:32:20.46 -27:45:46.47	25.29 ± 0.11	-1.61 ± 0.31	1.15/1.85/0.62	–	–	–	
96	03:32:15.94 -27:45:55.61	24.31 ± 0.07	-0.77 ± 0.11	1.85	2.18	1.99/2.39	[OII]	
97	03:32:43.60 -27:43:44.72	25.20 ± 0.12	-1.13 ± 0.22	0.62	1.25	1.22/1.32	Hα	
98	03:32:41.72 -27:43:51.29	24.10 ± 0.07	-1.12 ± 0.12	1.85/1.15	1.85	1.68/2.00	[OII]/[OIII]	
99	03:32:43.70 -27:43:34.66	24.81 ± 0.13	-1.38 ± 0.31	1.85	1.65	1.33/2.00	[OII]	
100	03:32:17.08 -27:45:35.77	24.55 ± 0.10	-0.85 ± 0.17	1.85	1.75	1.62/1.87	[OII]	
101	03:32:45.12 -27:42:59.60	24.31 ± 0.08	-0.73 ± 0.12	1.85	–	–	[OII]	
102	03:32:44.39 -27:42:45.45	23.87 ± 0.05	-0.81 ± 0.08	1.85	1.70	1.50/1.85	[OII]	
103	03:32:44.04 -27:42:44.09	24.02 ± 0.06	-0.96 ± 0.09	1.85	1.46	1.35/1.60	[OII]	
104*	03:32:28.01 -27:43:57.39	22.01 ± 0.02	-0.52 ± 0.02	0.6207	–	–	Hα	(6)
105	03:32:15.80 -27:44:34.53	22.63 ± 0.01	-0.44 ± 0.02	1.107	1.110	1.10/1.12	[OIII]/Hβ	(4)
106	03:32:15.35 -27:44:31.73	23.16 ± 0.03	-0.74 ± 0.03	1.835	1.82	1.76/1.90	[OII]	(4)
107*	03:32:23.40 -27:43:16.52	19.72 ± 0.01	-0.47 ± 0.01	0.615	0.01	0.01/0.012	Hα	(2)
108	03:32:41.12 -27:42:06.32	24.87 ± 0.07	-0.73 ± 0.11	1.85	1.68	1.58/1.82	[OII]	
109	03:32:34.60 -27:42:11.44	24.97 ± 0.07	-0.93 ± 0.12	0.62/1.15	0.60	0.57/0.62	Hα/[OIII]	
110	03:32:31.90 -27:40:46.55	25.60 ± 0.11	-1.27 ± 0.25	0.62/1.15/1.85	–	–	–	
111	03:32:25.31 -27:42:07.60	24.19 ± 0.05	-0.74 ± 0.09	1.15	1.14	1.04/1.26	[OIII]	
112*	03:32:41.83 -27:40:42.32	23.47 ± 0.05	-1.04 ± 0.09	0.6162	0.61	0.60/0.62	Hα	(2)
113	03:32:37.81 -27:39:53.01	23.36 ± 0.09	-1.42 ± 0.19	0.62/1.15/1.85	2.27	1.76/2.59	–	
114	03:32:27.66 -27:42:25.70	24.00 ± 0.04	-0.46 ± 0.05	1.15	1.14	1.10/1.17	[OIII]	
116	03:32:34.84 -27:40:18.16	23.76 ± 0.05	-0.50 ± 0.05	1.15	1.15	1.12/1.17	[OIII]	
118	03:32:13.27 -27:42:31.19	24.94 ± 0.07	-1.05 ± 0.12	1.85	–	–	[OII]	
120*	03:32:13.24 -27:42:40.91	18.88 ± 0.01	-0.36 ± 0.01	0.62	0.63	0.62/0.64	Hα	(7)
121	03:32:20.82 -27:48:35.96	25.32 ± 0.10	-1.19 ± 0.20	1.85	–	–	[OII]	

(1) (Le Fèvre et al. 2015); (2) Wolf et al. (2001); (3)Straughn et al. (2008); (4)(Morris et al. 2015) ; (5)Vanzella et al. (2006); (6) (Le Fèvre et al. 2004); (7) Balestra et al. (2010)

* The candidate is present in the extended sample of paper I.
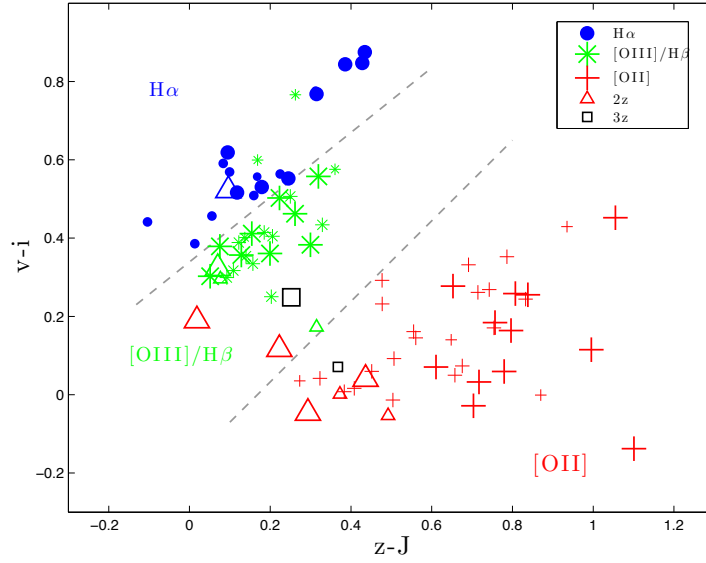
Figure 3.2: The colour-distribution of the candidate ELGs. The colour-coding is also given in the legend. Blue dots represent Hα galaxies at the redshift $z \sim 0.62$; green asterisks are [OIII]/Hβ emitters at the redshift $z \sim 1.15$ and red crosses represent [OII] emitters at the redshift of $z \sim 1.85$. Open triangles and squares are the candidates with double/triple redshift solutions respectively.

in the narrow-band filter and the Y-band filter which also contains the emission line. This ensures that the NB excess does not force the fit to a wrong outcome, and helps avoid that the derived physical parameters are skewed by the presence of the emission-line, which may not be correctly modelled by LePhare.

Overall, we were able to assign plausible and convincing redshifts to 28 of the new candidates. In deciding the most plausible redshift assignment we (admittedly) subjectively weighed in information from the SED plots and from the $v - i$ vs. $z - J$ colour-colour distribution. In 6 cases we have two equally plausible redshift solutions and we fail to assign redshift in three cases. These three galaxies are either very faint with high flux excess in the NB filter and none or very little detection in the broadband filters, or all three photometric redshift options appear equally probable. All faint objects have at least one detection bluewards of the NB filter, which eliminates the possibility for them to be the candidate high-redshift Lyman-α emitters.

All candidates obtained in this project, together with all candidates from paper I, are plotted on Fig. 3.2 using the same colour-coding as before. The size of plotting symbols indicates whether candidate is found in the new study (bigger plotting symbols) or comes from paper I (smaller symbols). There are three cases where we have double redshift solutions with primary options suggesting wrong placing of the candidates; but secondary options positioning them in the same location in the plot as other ELGs of the same type.

Overall we can say that this broad-band colour distribution can be a good guide in

cases where the photo-z method fails to provide unambiguous results.

SED fits for all candidates can be inspected in appendix B

3.3.4 SPATIAL DISTRIBUTION OF THE NEW ELG CANDIDATES

In Fig. 3.3 we plot the spatial distribution of candidates as in paper I. Here we find that nine out of twelve members of the galaxy protocluster are present in both studies. It is worth emphasising that there is a good chance that the two "new" galaxies on the north-east side of the protocluster, that have been excluded from the basic sample of paper I because they are located on the high-noise stripes caused by the chip gaps, may belong to the system. But both of them have two plausible redshift solutions, [OII] and [OIII]/Hβ. Spectroscopic observations are needed to firmly establish the redshift of these objects.

3.4 DISCUSSION

3.4.1 THE MAIN SEQUENCE OF STAR-FORMATION AND THE DUST CONTENT IN THE GALAXIES

The relation between galaxy mass and SFR and its behaviour with redshift is crucial to understand since it is a way to unveil the evolutionary picture of galaxies. We find substantial diversity in the galaxy populations and it is important to know what is the relation between these populations and what are the stages of galaxy evolution. From massive, red galaxies that show no star formation activity to low-mass, dust-free galaxies with bursty star-formation, we meet all types and diversities in our studies and therefore it is one of our goals to find out what is the evolutionary framework for these galaxies and how they go from one stage to another and why. In this project we are probing the main sequence of M_* vs SFR relation (Brinchmann et al. 2004; Noeske et al. 2007; Maiolino et al. 2008). For this, we obtained masses and SFRs using the same LePhare setup as in paper I. Namely, we use the same spectral templates, IMF, ages, etc. in order to get consistent and coherent results.

Table 3.2: Best-fit parameters for SFR vs M_* relation (See e.g., Fig. 3.6). First column represents the redshift bins of study, Second and third columns list slopes and constants for linear best-fits and fourth and fifth columns are χ^2 values corresponding to the linear and 2nd order polynomial best-fits.

Redshift	Slope	interception	χ^2	χ^2
			Linear	Polynomial
0.62	0.8608	-7.6061	2.0282	1.8357
1.15	0.8539	-7.4946	3.3684	3.3630
1.85	0.7117	-5.3544	5.2641	4.7993

Compared to previous studies we probe galaxies with stellar masses an order of mag-
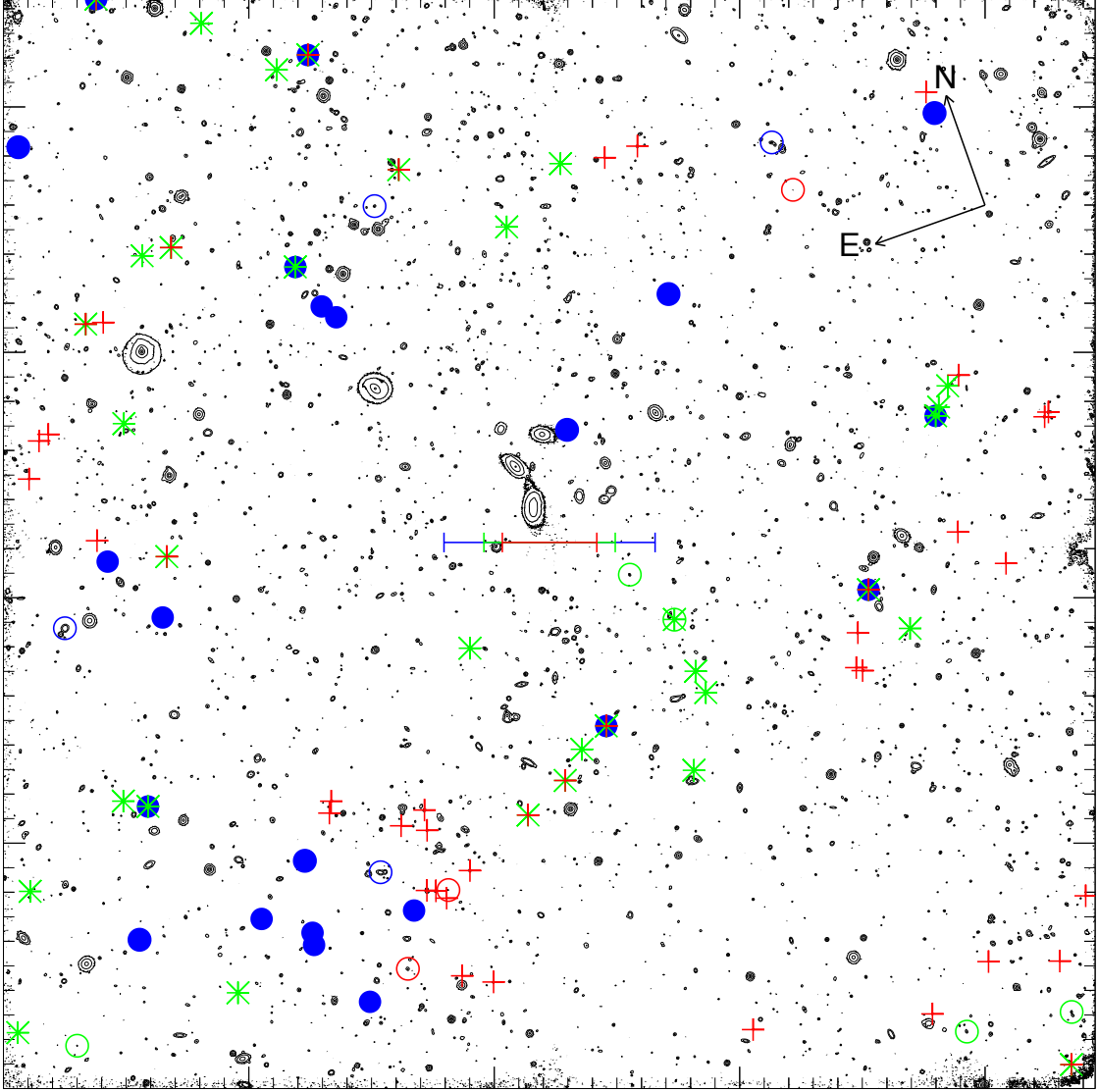
Figure 3.3: Spatial distribution of the candidate ELGs. The colour-coding is the same as in other figures. Namely, blue dots are the Hα emitters at the redshift of z∼ 0.62, green asterisks are the [OIII]/Hβ galaxies at the redshift of z∼ 1.15 and red crosses are the candidate [OII] emitters with the redshift of z∼ 1.85. Open circles are again the candidates from the "extended sample" of paper I. The multiple symbols over-plotted on top of each-other are the double and triple redshift solution cases. Here we do not distinguish between old and new candidates and are plotting them in the same plotting manner. The co-moving lengths of 1 Mpc is plotted in the centre and the NB image used in this plot is the same as in Fig. 15 in paper I, but the masking is obviously, not present on this image.
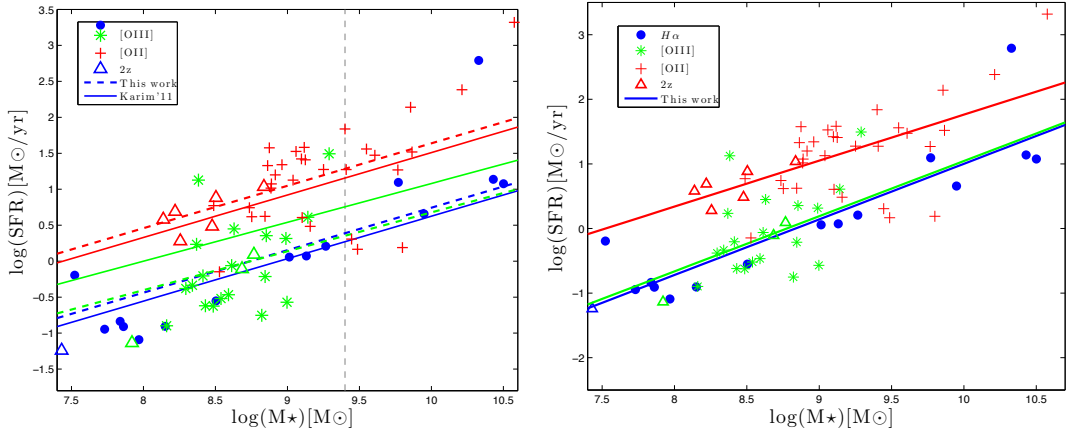
Figure 3.4: Star formation rate vs. stellar mass relation for our emission-line selected galaxies. Left frame presents best-fits obtained using (Karim et al. 2011) slopes (extrapolation of their relation with their constants down to lower masses (solid lines) and same slopes fitted to our data (dashed lines). Right panel presents our data and our best-fits obtained in the frame of this project. Blue dots represent Hα emitter galaxies at $z \sim 0.6$, green asterisks are the [OIII]/Hβ emitters at the redshift of $z \sim 1.15$ and red crosses are the candidate [OII] emitters at $z \sim 1.85$.

nitude smaller than previously. Overall, we now stretch the mass range between $M_* = 10^{7.5} - 10^{10.5} M_\odot$ and probe the galaxies with as modest star formation as $\sim 10^{-1.2} M_\odot / yr$ to up to almost $\sim 10^{3.5} M_\odot / yr$.

Results of this study are in agreement with those of paper I. But there are also significant differences. Namely, with this method we successfully select galaxies not only in their main-sequence stage of SFR vs. M_* relation, but also in the starburst phase. This is because we are able to allow smaller emission line EWs for very bright galaxies. This implies that varying selection methods can significantly influence the population of the galaxy sample of study. This on the other hand, means that the magnitude-colour selection method is the better way to probe the mass vs SFR relation for galaxies with different properties. We also compare our findings with the findings of other authors to see how consistent we are.

In this article we compare our data and the best-fit parameters by two different groups. First of all, we compare our work with Karim et al. (2011) (K11 hereafter) study by adopting their slopes of the linear best-fit relation and applying shift to obtain best-fits to our data. The results of this part can be visualized on the left panel of the Fig. 3.4. The best-fits are significantly shifted from each other in each redshift bin and since the emission-line selected galaxies are expected to have higher average SFR values, we would expect to find a higher normalisation at all redshifts. However looking at the left panel of Fig. 3.4, we see that in case of $z = 1.15$ galaxies our resulting best-fit is significantly below K11 one. This can be caused by the difference in the selection methods (our and K11) and the fact that the galaxies in the above-mentioned redshift bin are more concentrated in terms of mass range; i.e. there are no massive [OIII]/$H\beta$ emitters present in this study,
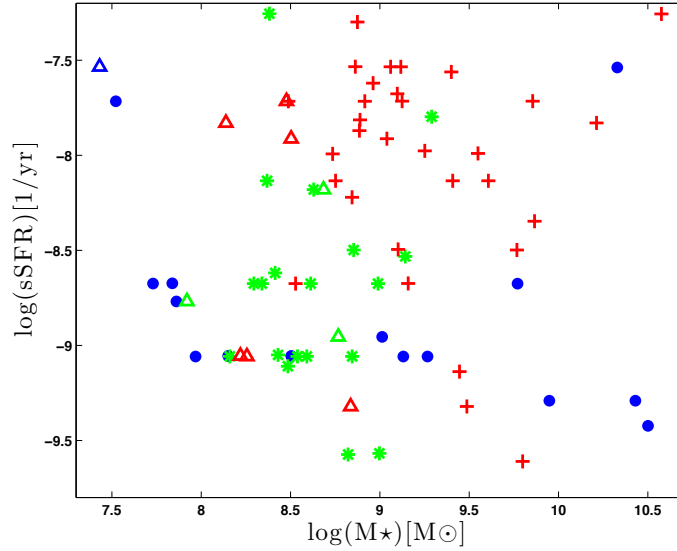
Figure 3.5: Specific star formation rate vs M_* relation for candidate ELGs

therefore this might influence the best-fit. However this kind of comparison in itself, is not very accurate to show the nature of the SFR vs M_* relation properly because *a).* the slopes for three different redshift bins are not the best-fits to our data, but are borrowed from the other work which is based on completely different selection method instead. *b)* Another problem with this kind of comparison is that K11 probes the relation only for galaxies with masses above $log(M_*) > 9.4 M_\odot$ which in our case covers less than a half of the range of study. What happens to the galaxies below this mass limit, K11 work can only predict by extrapolation to the low-mass end.

In paper I we compared our work with the same article and saw that we obtain slopes that are steeper than those, K11 can predict (by extrapolation of the same relation down to lower masses). In this paper we aim to obtain the best-fit parameters for our data independent from other works. In Fig. 3.4 we present the linear best-fits to our SFR vs M_* relation and corresponding slope and constant values are listed in Table 3.2. The slopes seem to be steeper than K11 extrapolated estimates (See right panel of Fig. 3.4 or left column of Fig. 3.6 for better comparison with K11 slopes in each redshift bin). The steepening is still the case, however it seems to be less pronounced than in paper I. In our previous work we find the mean slope for three redshift bins to be 1.17. While in this work the values are between $\sim 0.7 - 0.9$ and the mean slope for three redshift slices is 0.81. One of the reasons why the steepening of the SFR vs M_* slope is different from paper I estimated mean is the difference in the selection methods. In this work we find galaxies with more diverse nature - from "normal" to "starburst" populations. The latter characterizing the upper end of the SFR vs M_* relation influences the steepness of the slope making it flatter.

One way of obtaining estimates for our emission-line galaxies would be to derive

the mass-independent SFRs (or specific SFR) and exclude the galaxies with extreme star-formation this way, but it is not trivial. First of all, defining where the "starburst" characteristics end and "normal" ones begin needs to be very strict; in our case, for the lowest redshift bin ($z \sim 0.62$) the two populations seem to separate quite clearly, but as soon as we look at the sSFR values for the $z \sim 1.15$ and $z \sim 1.85$ samples, the picture becomes more complicated – there is a smooth transition between the populations and no way of splitting them in a objective way (see Fig. 3.5), hence, making the study a combination of galaxies of filling out a continuum of star-formation intensities. Moreover, all these galaxies entered our sample because of being selected by the emission-line flux excess in the narrow-band filter, so they are representative of the study that we are performing. Hence, their influence on the estimates is one of the new findings of this study compared to paper I. In summary, after comparing our findings with K11, we still find the steepening of the SFR vs M_* slopes for three redshift slices, but with the sample that almost doubled in size, we find slope values that indicate less steepening (see Table 3.2) than that found in paper I.

We also compare our findings with the work by Whitaker et al. (2014) (W14 here-after), who instead of using linear best-fits, use polynomials. We over-plot W14 estimates to our data to check how they fit with our results. In the right column of Fig. 3.6 we plot these estimates with dashed lines. The W14 estimates do not agree well with our data, therefore we obtain polynomial best-fits and plot them to see how diverse is the picture (solid lines in the right column of the same Fig. 3.6). We expected to find best-fits that would have the same direction, but different coefficients depending on our data points. However in two out of three redshift bins ($z = 0.62$ and $z = 1.85$) the polynomials have an upturn in the low mass end, hence have completely opposite direction relative to W14 estimates.

In the case of $H\alpha$ emitters (top-right panel of the Fig. 3.6), the upturn seems to be caused by the presence of the low-mass starburst galaxies and a galaxy with a very high SFR in the upper mass end. While in the case of [OII] galaxies (bottom-right panel of the same Fig. 3.6), the low-mass end upturn seems more likely due to the shallowness of the galaxy sample. One of the proofs that starbursts strongly influence the estimates can be seen in the middle panel of the Fig. 3.6 ($z = 1.15$). Galaxies in this bin, as we already mentioned above, are more concentrated mass-wise and have less dramatic SFR values, therefore the 2nd order polynomial estimate for this bin seems to be less influenced by the starburst galaxies. And in the case of [OII] galaxies, looking at the sSFR values (Fig. 3.5), we can see that most of them are the starbursts. Because of the selection effect, the chance of detecting galaxies less massive than $M_* < 10^8$ at this high redshift are small, therefore in order to obtain better polynomial fits for this redshift bin, we will need to have more members of the "normal" population together with these starbursts.

In order to adopt the linear or polynomial coefficients as final results, we derive the χ^2 values for both types. These χ^2 values are listed in Table 3.2. Going from linear fits to polynomial ones does not increase significantly in precision, i.e., the χ^2 values for linear and polynomial fits are in the same range. Looking at Fig. 3.4 we can see that we
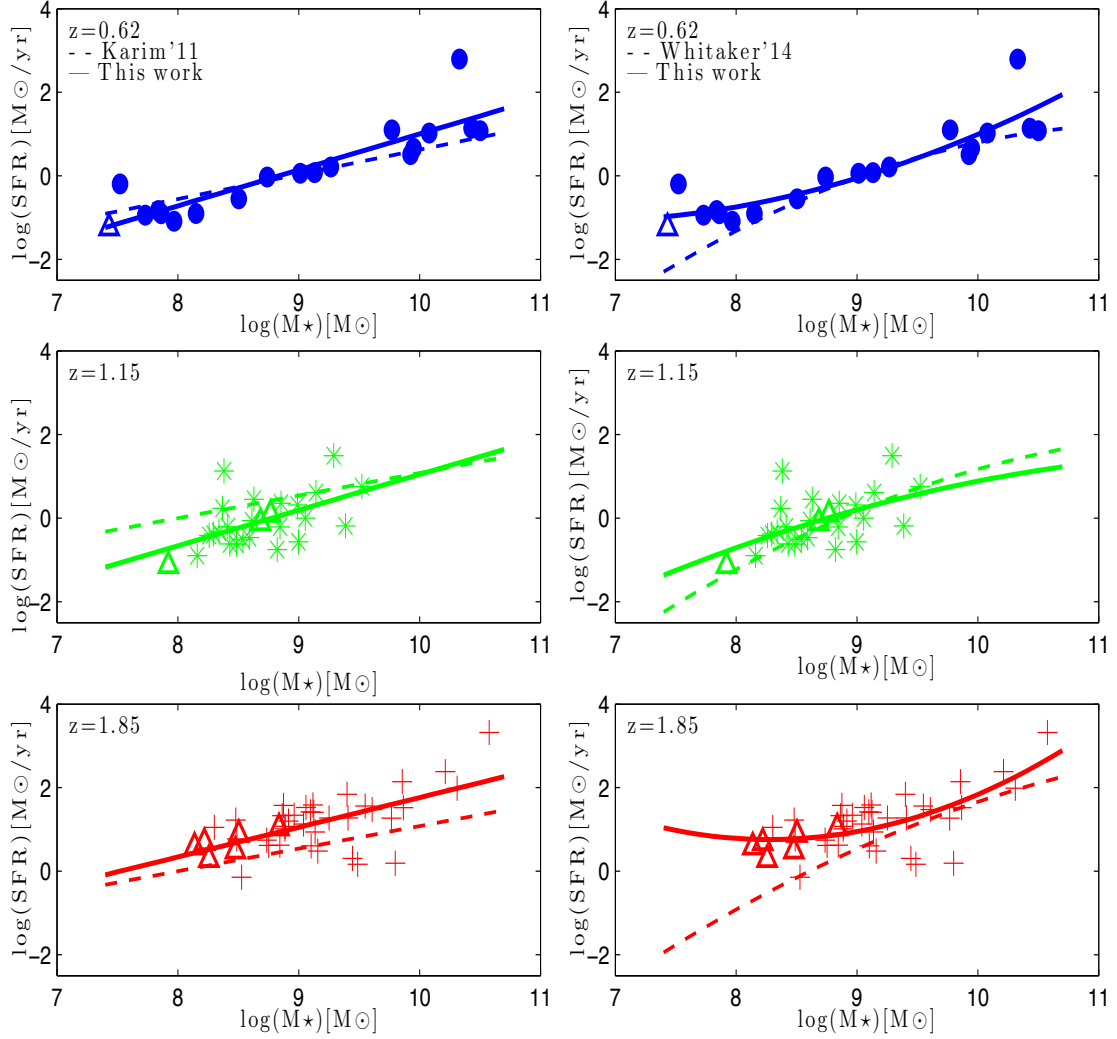
Figure 3.6: SFR vs $M*$ relation for three different redshift bins and comparison with studies by other authors. Left column shows the relation for linear best-fits and comparison with Karim et al. (2011) work; blue dots correspond to $H\alpha$ emitters and the redshift of $z = 0.62$; green asterisks are the [OIII]/$H\beta$ emitters at the redshift of $z = 1.15$ and red crosses are the [OII] emitters at $z = 1.85$. Colour and symbol coding in the right column is identical to that of the left column, but here we plot polynomial best-fits from Whitaker et al. (2014) and best-fits obtained in the frame of this project.

characterize the nature of emission-line galaxies better with linear fits than polynomial ones. Therefore, at this point, we adopt coefficients for linear best-fits.

Overall, we conclude that the steepening of the SFR vs M_* slope that has been found in the paper I is present also in this study despite the difference in the selection methods.
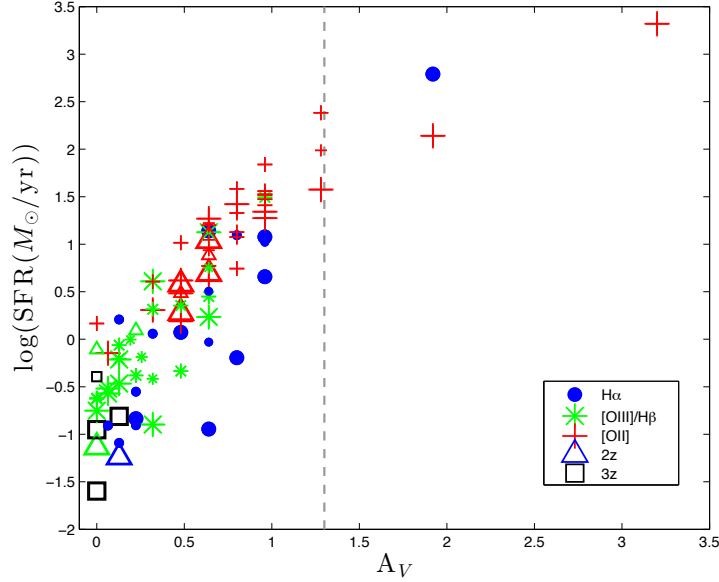
Figure 3.7: SFR vs A_V relation for our emission-line selected galaxies. The colour-coding and the symbols are the same as in all other plots. The grey dashed line marks the maximum dust abundance for candidates from paper I.

We are also looking into the dust content of galaxies to see what can be inferred from there. In Fig. 3.7 we plot the A_V vs SFR relation of our candidate ELGs. The grey dashed vertical line in this case, marks the maximum A_V value in paper I. It is clear that there are new candidates that are heavily dust-obscured with quite high star-formation rate. In general, we probe very diverse populations in this study. Namely, from low-mass dust-free galaxies at all redshifts to dusty, star-forming ones. Overall, there seems to be a tight relation between the A_V index and the star-formation rate. For the Hα and [OII] slices, the span of relation in the direction of SFR is almost 4 and 3 dex accordingly. While for [OIII]/Hβ slice the scatter is in the range of ~ 1.5 dex.

Part of the reason for a large span for $z \sim 0.62$ galaxies is due to the selection effect. At higher redshifts we are not able to detect galaxies with as low masses. But there seems to be one more interesting thing to pay attention to. The [OIII]/Hβ population seems to be less variant among the three. Also, if we look at the mass vs SFR relation plot (see e.g. Fig. 3.6), it is clear that these galaxies probe masses that are in a more compact range than the other two bins. The reason why this happens is not so obvious. First of all, the [OIII]/Hβ galaxies are the ones that have the most extreme EWs usually. This would imply that the these galaxies are the most actively star-forming ones in general, but the picture looks pretty different.

3.4.2 NOTES ON INDIVIDUAL OBJECTS

Since we detected galaxies that seem to be markedly different from the ones in paper I, more specifically very dusty and IR-luminous starbursts, we describe these in more detail in this subsection.

ELG80
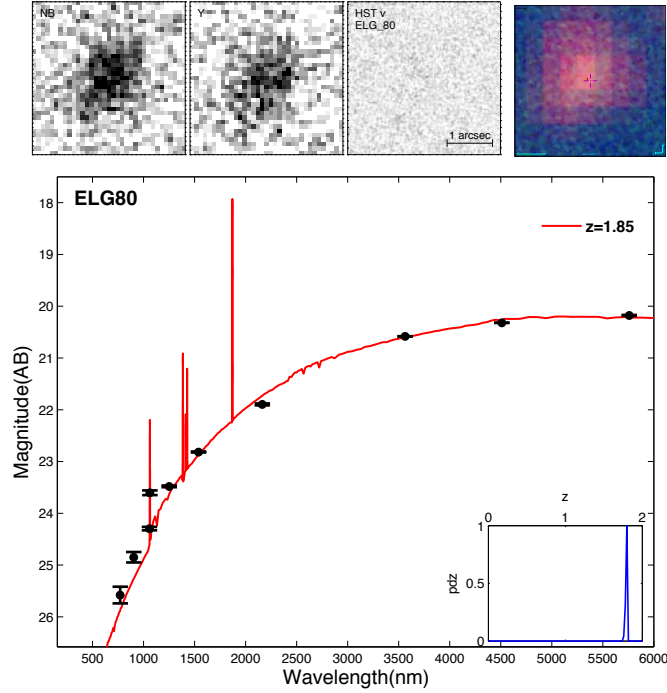
Figure 3.8: ELG80 – a massive ($M_* = 10^{10.5} M_\odot$) starburst galaxy (SFR=$10^{3.3} M_\odot/yr$) that is completely dust-obscured in the NUV and part of the visible bands U, $F435$, $F606W$); its flux gradually increases from ACS $F775W$ all the way to IRAC 8.0μm. The upper panel represents poststamp images of the object in $NB1060$, Y and $F606W$ bands and the fake colour-composite (Blue - HST $F435W$, Green - HST $F606W$, Red - IRAC 3.5μm) as well. The lower panel shows the actual SED fit of the object. Red solid line is the theoretical fit to the photometry (black points) and the blue line in the right low corner represents the probability distribution per redshift bin.

ELG80 is a spectacular candidate emission-line galaxy, with moderate colour excess value $NB1060 - Y = -0.70 \pm 0.06$ and is undetected in the UV and visible bands up to HST $F850LP$. It is also above the magnitude cut threshold of paper I, therefore, in principle, it ought to be selected also in paper I. We find that it has not been selected as an ELG candidate in paper I because of its $NB - J$ colour. Namely, the object is brighter in the J filter ($NB - J = 0.12 \pm 0.05$).

In Fig. 3.8 we present the SED. The upper panel of the figure shows the poststamps

from $NB1060$, Y and HST $F775W$ and the fake colour-composite image of the same object where we use three different frames: ACS $F435W$, $F606W$ and IRAC 3.5μm. The lower panel shows the actual SED fit of the object: it is undetected in VIMOS U, HST ACS $F435W$ and $F606W$ bands and has a detection (and its flux gradually increases) from HST ACS $F775W$ all the way to SPITZER IRAC 8.0μm. The fact that it has a detection in two of the visible bands, excludes the possibility of this object to be a candidate high-redshift Lyman-α emitter, but its SED fit suggests that is a starburst galaxy that would be left out of the selection sample with the colour-colour selection method used in paper I due to the steep continuum slope around the position of the emission line.

ELG102

ELG102 is detected in all photometric bands included in our study. Unlike the previous case, the main reason why this candidate was not selected as an ELG in paper I is its location in the edge of the image, which was excluded in paper I due to masking. However, even if it was located in a better area, it would have been placed just outside the selection threshold of paper I with its colour excess values of $NB - Y = -0.81 \pm 0.08$ and $NB - J = -0.17 \pm 0.06$.

In Fig. 3.9 we, again, plot the poststamps of the candidate in $NB1060$, Y and HST $F775W$ bands and the fake colour-composite constructed using ACS $F435W$, $F606W$ and IRAC 3.5μm. The lower panel presents the SED fit of the galaxy. Here, as well as in the previous case, the flux gradually increases from UV to NIR. The candidate is very compact, which is not something that we would expect for starbursts because the bursty star formation is usually related to morphological transformations (see, e.g., Conselice et al. (2000); Knapen & James (2009)). The A_V index of this galaxy is significantly smaller than that of the ELG80 (see Fig. 3.7).

ELG120

This galaxy (Fig. 3.10) is the most spectacular amongst all objects selected here and in paper I. It is a complex system with several emission components. Some of the complexity may of course be due to change alignments and it would be very interesting to secure IFU spectroscopy of this system. The central object of the system looks like a disky system with clear spiral arms (these are clear in HST ACS frames). In addition to this it has four distinct separate blobs and a tadpole counterpart on the NW side.

The object did not make it to be part of the selection in paper I because of the relatively small colour excess. The colour indices for this system are: $NB1060 - Y = -0.36 \pm 0.01$, and $NB1060 - J = -0.34 \pm 0.01$, which place it in the cloud of continuum sources in paper I, their Fig. 2.

ELG120 is a massive ($M_* = 10^{10.3} M_\odot$) starburst galaxy with strong dust-obscuration ($A_V = 1.92$) and a high star formation rate of $SFR = 10^{2.8} M_\odot/yr$. It seems likely that the star formation in this galaxy is enhanced due to a merger.
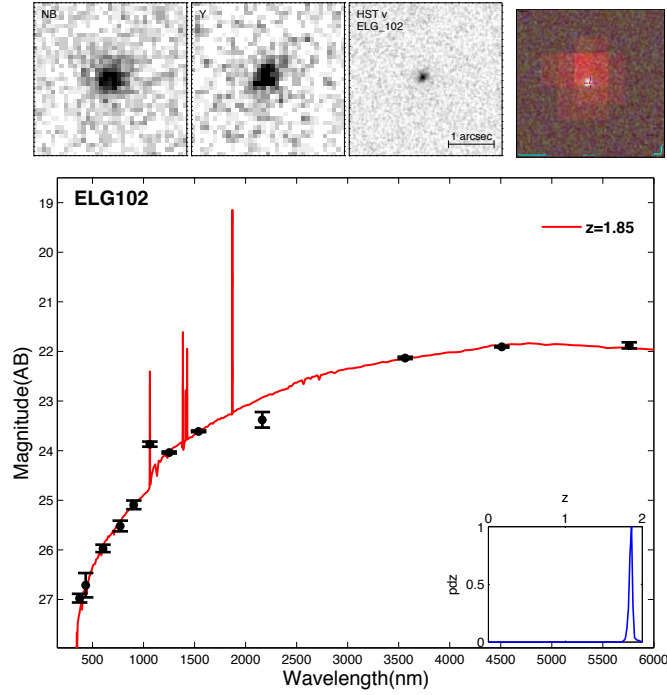
Figure 3.9: The upper four frames are the poststamps of ELG102 in $NB1060$, Y and $F606W$ bands and the fake colour-composite (HST $F435W$, $HSTF606W$, and Red - IRAC 3.5μm) and the lower part is the SED fit. The black points are the measured fluxes and the red solid line is the theoretical fit. The blue solid line in the lower right corner represents the probability distribution for the redshift.

The 5.8 μm and 8.0 μm data points seem to be boosted compared to the theoretical best fit model estimate (Fig. 3.10). The reason why this could have happened is the weight of the other data points that shifts the entire fit down, thus the theoretical flux value in the above-stated two filters gets underestimated. If the error bars on these measurements were a little bit larger, than the fit would match the 5.8 μm and 8.0 μm data points better.

ELG121

We first discarded this candidate from the sample after cross-matching with G13 catalogue where it is not included. However, after re-visiting the list of discarded objects to make sure that we were not losing real sources we found that this particular object was a real object and not spurious.

At first, we thought that this could be a high-redshift Ly-α candidate, but once we closely inspected the HST ACS images, it was clear that there was a detection in the HST v-band, which immediately excluded a high-redshift interpretation.

Since the object is not included in the G13 sample we had to perform aperture photometry in order to examine the SED of the candidate. The aperture photometry
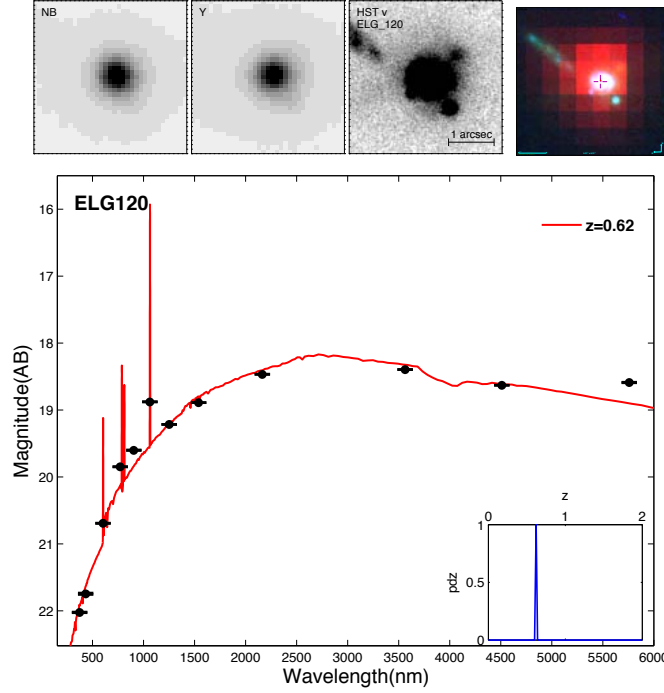
Figure 3.10: ELG120 appears to be a merging system. The mass of the system is $M_* = 10^{10.3} M_\odot$ and the star-formation rate is also quite enhanced - SFR=$10^{2.8} M_\odot/yr$. The upper panel of the image represents the poststamps of the candidate in the $NB1060$, Y, ACS $F606W$ bands and a fake colour-composite image (HST Red - IRAC 3.5μm Green - HST F606W, Blue - F435W). The lower panel is the actual SED fit with black points corresponding to the photometry from G13 and the red solid line - theoretical best-fit model. The blue solid line in the lower corner of the image is the probability distribution per redshift bin.

suggests that the object is a heavily dust-obscured star-forming galaxy at the redshift of $z = 1.85$ and hence that we detect the [OII] emission-line in the NB1060 filter. The candidate is massive ($M_* = 10^{10.5} M_\odot$) and has a quite high star-formation rate ($SFR = 10^{2.22} M_\odot/yr$), which is heavily obscured by dust ($A_V = 3.2$).

Looking at the cutout images (especially the HST WFC3 $F160W$-band) and the SED fit (Fig. 3.11), we find that the source has a very close neighbour on the SE side, which seems to be blended with our candidate in the IRAC images. This same counterpart is also found in the G13 catalogue with the same blended IRAC photometry. The distance between the two components is around 1". Having this all in mind, and also the fact that the source seems to be one very bright clump in the IR, we conclude that this is likely to be a merger at redshift of $z = 1.85$.
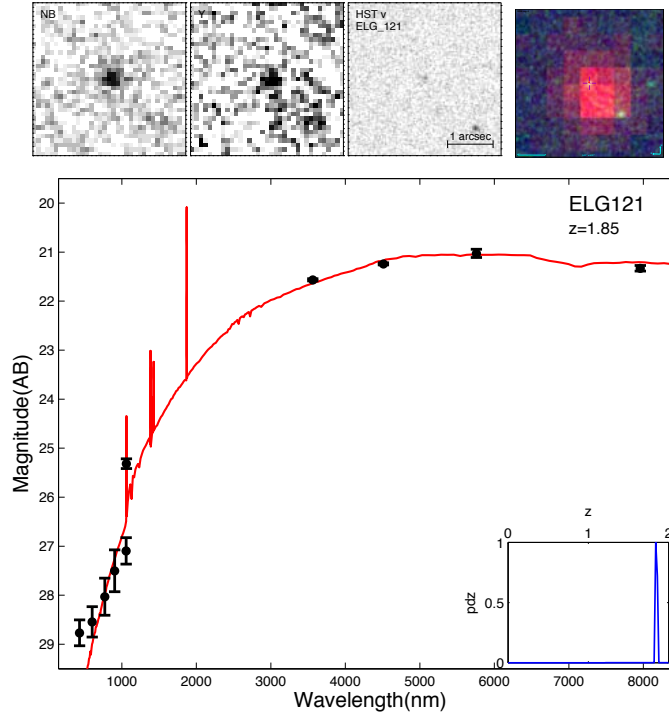
Figure 3.11: ELG121 was originally excluded as is is not detected in the G13 catalogue. However, after visual inspection we concluded that this indeed looks like a real object and not a spurious detection caused by image defects. The upper panel presents the poststamp images of the source in three different photometric bands: $NB1060$, Y and $F606W$ and the fourth image is the fake-colour-composite of the same object (R - IRAC 5.8μm, G - WFC3 $F105W$ B - ACS $F775W$). The lower panel shows the actual SED fit of the very same galaxy. It seems that the IR flux of the system is very high. But closer examination of ELG121 shows that the object has a very bright neighbour nearby (R$\sim 1''$), that shows a very similar character. Namely, it is absent or very compact in the UV and visible bands and becomes bright in the IR. The objects seem to be blended in the IRAC frames, which probably causes the boost in the IR flux. However, there is a good chance that the system is an interacting (possibly merging) one.

3.5 CONCLUSIONS

In this study we aimed to compare two different narrow-band selection methods in order to see how the results would differ. Together with this goal, we also wanted to reach down to fainter objects and see how reliable their SED fits would be and what would be learned about *1)* SFR vs M_* relation and *2)* the large-scale structure. It is especially interesting to test if the steepening of the SFR vs $M_\odot$ relation still holds when we complete our sample down to faintest magnitudes possible. We also eliminated the masking that we applied in paper I, hence included the more noisy areas in our new study. After performing selection and study and analysing the results, we conclude that:

1. The magnitude vs colour selection method has an advantage of selecting a wider variety of candidate emission-line galaxies compared to the colour-colour selection method. This implies that with the magnitude-colour selection method, one does not lose candidates with relatively small colour excess that are bright. These kind of objects are still emission-line galaxies that end up being "hidden" in the cloud of colour-colour continuum due to the small colour index.

   One might think that the colour-colour selection method would be more successful in selecting high-redshift Ly-α candidates, but since the Ly-α line is very sensitive to dust, it is only very high EW early galaxies that end up being selected with the colour-colour selection method, thus candidates with smaller colour excess may be left undetected. Very dust-obscured galaxies have continua with a very red spectra slope, which make it difficult to select such object in the colour-colour plot method. The magnitude-colour selection method, on the other hand, picks galaxies that can have relatively small colour excess, but are bright. However, one has to balance the selection criteria well between not mis-selecting the low EW candidates that are still ELGs and selecting spurious sources.

2. Plotting masses and SFRs from all samples (this project, "basic" and "extended samples" of paper I), we find that overall, as we already mentioned, the emission-line selection method successfully detects galaxies not only at the main sequence, but also those that occupy the starburst region of the relation.

3. The steepening of the M_* vs SFR slope that has been found in paper I, still holds in this study. The estimates that have been obtained in comparison with other studies, are still valid even though the size of the sample has doubled in this work. We now confirm that despite the increased depth and expected shaky SED fits, the results are robust and hold well. Although we find that the steepening of the M_* vs SFR slopes for three redshift slices are relatively small compared to the average slope we found in paper I. In this work we present the new slope values and interceptions (Table 3.2).

4. We successfully locate the galaxy cluster that has been detected in paper I. Nine out of twelve cluster member galaxies are present in this study and the other three disappear because of the flags or little $NB1060 - Y$ colour excess for a given magnitude bin.

Table 3.3: Physical parameters resulting from SED fitting

ID	log(mass)	log(SFR)	Redshift
ELG#	$logM_\odot$	$log(M_\odot/yr)$	
80	10.58	3.32	1.85
81	8.37	0.23	1.15
82	9.10	1.42	1.85
83	8.53	-0.15	1.85
84	9.95	0.66	0.62
85	7.52	-0.19	0.62
86	8.96	1.34	1.85
87	10.43	1.14	0.62
88	8.54	-0.52	1.15
92	8.38	1.13	1.13
93	8.16	-0.90	1.15
94	9.00	-0.57	1.15
96	9.16	0.48	1.85
97	7.73	-0.94	0.62
99	9.80	0.19	1.85
100	8.75	0.62	1.85
101	8.87	1.58	1.85
102	9.86	2.14	1.85
103	9.25	1.27	1.85
104	9.13	0.07	0.62
105	9.14	0.61	1.11
106	9.77	1.27	1.84
107	10.50	1.08	0.62
108	9.45	0.31	1.85
111	8.59	-0.47	1.15
112	7.84	-0.83	0.62
114	8.82	-0.75	1.15
116	8.85	-0.21	1.15
118	8.84	0.62	1.85
120	10.33	2.79	0.62
Ambiguous cases			
79	8.22	0.69	1.85/1.15
89	8.26	0.28	1.85/1.15
90	7.92	-1.14	1.15/0.62
91	8.14	0.58	1.85/1.15
98	8.84	1.04	1.85/1.15
109	7.43	-1.24	0.62/1.15
95	7.23	-0.95	1.15/1.85/0.62
110	7.09	-1.60	0.62/1.15/1.85
113	7.09	-0.81	0.62/1.15/1.85

4

CONCLUSIONS AND FUTURE PLANS

The evolution of galaxies up to redshift $z \sim 2$ has been actively studied in the last decade and important results have been obtained (Daddi et al. 2007; Rodighiero et al. 2010) regarding their nature and evolution. Studying the formation and evolution of galaxies at different cosmic ages is crucial for understanding evolutionary picture of the Universe. We nowadays have a sufficient amount of observational data to study the properties of the Universe with different methods. Thanks to multiband photometric data, we can construct the Spectral Energy Distribution of galaxies and obtain physical properties with significantly improved accuracy. Physical properties based on SED fits nevertheless hinge on the accuracy with which the photometric redshifts can be determined.

In this thesis I have presented studies aimed at exploring the nature of galaxies spanning a redshifts range of $0.5 < z < 2$ and selected with narrow-band selection technique.

Below I briefly summarise the main results obtained in the thesis and discuss possible future developments and other ways to study galaxies at a wider redshift range.

4.1 SELECTION AND STUDY OF GALAXIES AT $0.5 < z < 2$

In Chap. 2 and 3 I presented a study based on the narrow-band selection method. Narrow-band transmission filters are designed to detect emission-lines from galaxies with equivalent widths in the range of a tenths to a few hundred Ångströms. With such a method it is possible to detect galaxies that have very faint, or even undetectable continuum spectrum, but (relatively) strong emission-lines. The ultimate goal is to detect Ly-α emitters at the cosmic dawn for galaxies at $z > 7$. However, the downside of this method is that the higher redshift we aim for, the bigger the number of so-called interlopers that are detected. Interlopers are galaxies at lower redshift with other emission-lines than Ly-α in the same range as high-redshift Ly-α emission-line would. There are a few strong emission-lines other than Ly-α and these are primarily Hα, [OIII]/Hβ, [OII].

The main goal of this project was to characterise the nature of the interloper emission line galaxies found in searches for $z \sim 7 - 8$ Ly-α galaxies. More precisely we have consequently studied these interlopers: Hα at $z \sim 0.6$, [OIII]/Hβ at $z \sim 1.15$ and [OII] at

$z \sim 1.85$ with two slightly different selection methods and obtained the following results.
Colour-colour selection method - In the work presented in Chap. 2 we selected
our galaxy sample with two sets of colours ($NB1060 - Y$ and $NB1060 - J$) imposing
a magnitude limit of 24.8 AB. The main reasons for adopting this procedure are the
following. First of all, the SED fits obtained for galaxies that are brighter than the
above-stated limit, are very reliable and robust. The Second reason for adopting this
magnitude limit is the expected depth of the UltraVISTA survey. UltraVISTA is one of
the biggest and deepest on-going surveys to trace the primeval galaxies in the COSMOS
field with the VISTA telescope. Studying interlopers, their nature and abundance in this
project, is a very good starting point for having an idea what to expect from the deep
surveys like UltraVISTA.

With this motivation in mind, we studied a sample of 40 galaxies in the GOODS-
South field, selected with the colour-colour method, and obtained the following results.

I. For 35 out of 40 galaxies we found unique redshift solutions. These redshift solutions
are in perfect agreement with the spectroscopic values already measured for some of
these galaxies. In four cases we find two redshift solutions, but we have a favoured
and a less likely one. The favoured solutions agree well with the photo-z values
from large on-line catalogues like e.g., the MUSYC catalogue (Cardamone et al.
2010). In only one case all three redshift solutions obtained are equally likely.

II. We derived a number of physical properties for our candidate emission-line galaxies
(*e.g.* M_*, SFRs, E(B-V), photometric redshifts, ages, etc.) and investigated the
relation between M_* and SFR. In this project, we probed galaxies with masses in
the range ($\sim 10^{7.8} - 10^{10} M_\odot$) and report a steepening of the M_* vs SFR slope for
galaxies with $M_* < 10^{9.5} M_\odot$.

III. We discovered a galaxy protocluster at redshift $z \sim 2$, which seems to be an actively
star-forming system. The very same cluster has been discovered spectroscopically
by Mei et al. (2015) few months before us. This provides a very nice confirmation
of the validity and strength of the photo-z method. Finally, we report the discovery
of a likely large-scale structure at $z \sim 1.15$.

Magnitude-colour selection method - In Chap. 3 I presented a follow-up study to
project described above. The two main differences with respect to the previous study
are: *1)* instead of using a set of three filters for the candidate selection, we use the set
of two filters, the $NB1060$ and its transmission-counterpart, broad - Y and the $NB1060$
magnitudes to select the candidate emission-line galaxies; *2)* we drop the magnitude
limit imposed in the previous selection. By doing so, we find some important differences,
which can be summarised as follows:

I. the magnitude-colour selection method successfully traces the galaxies that have
relatively smaller colour excess, but are very bright. Loosing these kind of candi-
dates is unfortunate and biases the sample,

II. the candidates selected with the magnitude-colour method are successfully picking not only the galaxies on the MS of the M_* vs. SFR relation, but also the starburst populations.

Despite these changes in the candidate selection method, the main results of the previous study are confirmed. Namely, the steepening of the slope in the M_* vs. SFR relation for galaxies with $M_* < 10^{9.5} M_\odot$ still holds, and we of course still detect the galaxy protocluster at $z \sim 2$.

4.2 TREASURE HUNT IN THE COSMOS WITH ULTRAVISTA

In the last few months I have been working on the detection of NB118 selected Ly-α galaxies in the UltraVISTA survey. Since no valid candidates have been found, my main goal in the project was optimising the search technique by introducing mock point-like sources in the real UltraVISTA data frame and recovering them with SExtractor. The aim is to determine the recovery rate of mock objects of different magnitudes. After completing this first step, I plan to use the simulated image of the Ly-α blob (by Peter Laursen), instead of the point-like sources, and determine if this can also be successfully recovered using the same technique.

4.3 WORK IN PROGRESS: MUSYC GALAXIES OF DIFFERENT GENERATIONS (MUSYCALS)

Understanding the relation between different physical properties of galaxies, (e.g., M_* vs SFR) and their behaviour across a large redshift range, gives us hints on the mass assembly in the galaxies and how the evolutionary picture evolves with cosmic time.

In the framework of this project, we are investigating all galaxies that have spectroscopically confirmed redshifts between $0 < z < 6$ despite the selection method that has been used to obtain them. We choose the GOODS-South field because of the amount of multiband photometric and accurate spectroscopic data available to-date. In particular, we use the MUSYC survey (Cardamone et al. 2010). For retrieving the SED fits and physical properties of galaxies, we use the LePhare code (Arnouts et al. 1999; Ilbert et al. 2006).

4.3.1 FIRST RESULTS AND PROJECT DEVELOPMENT

In the current data set we have about 1300 galaxies that have robustly measured spectroscopic redshifts; we obtained physical parameters and are currently in the process of performing a thorough scientific investigation of various fundamental relations throughout large redshift range ($0 < z < 6$).

Here we present the first sample plot of the M_* vs. SFR relation for our galaxy sample. The relation of this kind gives us possibility to understand how galaxies of

different population are interconnected and how they transform and evolve with cosmic time See Fig. 4.1. In this plot we present galaxies in consecutive redshift bins (two or three bins in each plane) and investigate the behaviour of the stellar mass and the SFR across $0 < z < 6$. From our first preliminary plot we see that the slope of the SFR changes dramatically with redshift. The slope for the lower redshift galaxies is pretty steep and the galaxy population clearly divides into star-forming and passive populations. However for the galaxies that have $z > 2.5$, the SFR becomes almost constant and the average SFR value gets higher and higher.
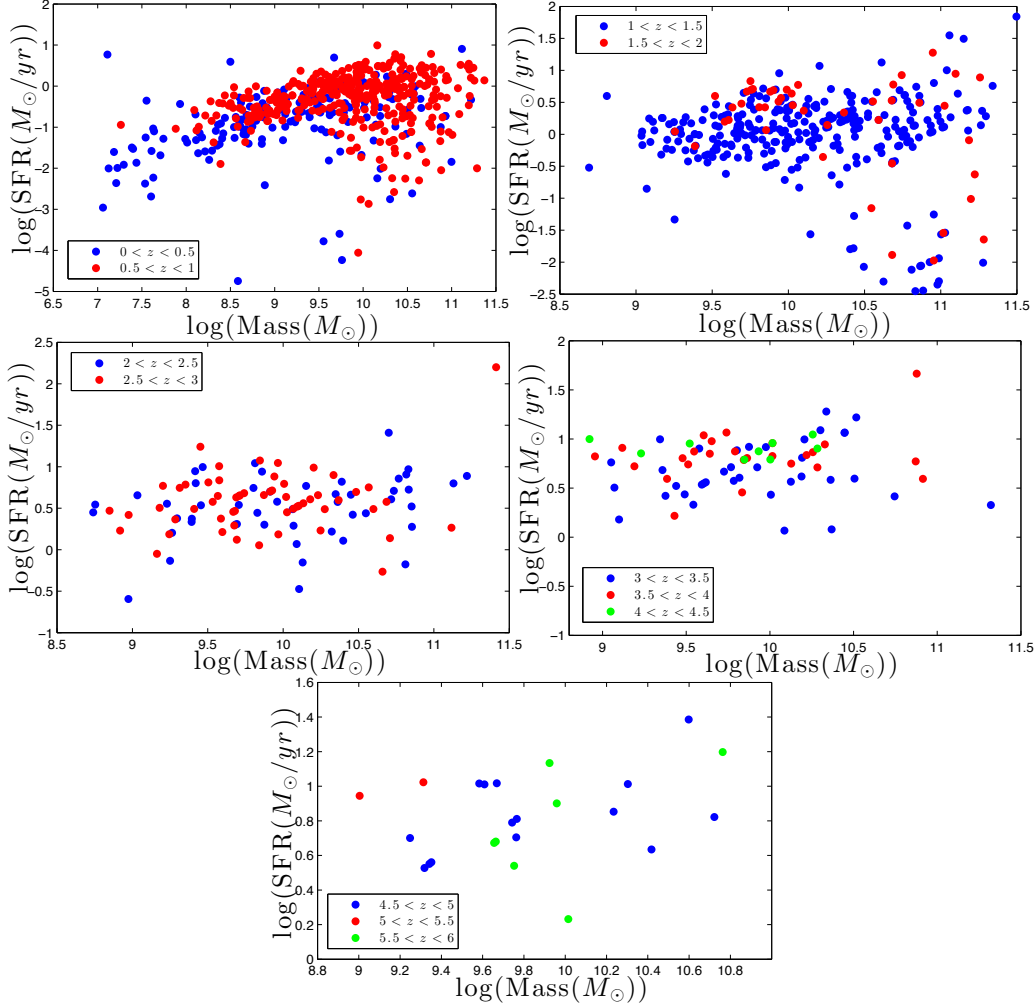
Figure 4.1: $M_\odot$ vs SFR relation for ~ 1300 objects . The sample is divided into five plotting groups. First panel represents the galaxies in first two consecutive redshift bins: $0 < z < 1$. Second and third panels represent galaxies in the following two consecutive bins ($1 < z < 2$ and $2 < z < 3$). In the fourth and fifth bin we plot three consecutive redshift bins per panel (therefore $3 < z < 4.5$ and $4.5 < z < 6$).

The preliminary results that we obtain so far, are in a significant disagreement with the works by other authors. One of the reasons why this is the case, could be the amount

of data that we have gathered so far. In order to be able to obtain solid arguments on the matter and investigate the galaxy evolution picture across such a vast redshift range, we will need to extend our data set further and obtain more galaxies with robustly measured redshifts (especially in the bins above $z > 3.5$).

The aim in this project is to derive the global star-formation estimates across vast redshift range and find the ways of completing the mass assembly picture for galaxies. We expect to have a quality information and new results about the evolution of the Universe from the perspective of galaxies, by the time the project enters final stages of its development.

4.4 GENERAL EPILOGUE: MY VISION FOR THE FUTURE

Accurately mapping galaxies in the universe, is key to reconstruct the history of the galaxy evolution. In my view, at this stage, it is the right moment to bring together catalogues, containing galaxies with accurately determined properties and combine them. The standardisation of the analysis procedures plays a central role for the success of such a programme (for example, it is crucial to have identical initial input information like, photometry from the same wavelength ranges). Deriving various different relations, such as mass-metallicity relation, mass-star formation rate relation, for large samples of galaxy populations is going to give us more reliable hints on the evolution of the universe from the point of view of galaxies. In this framework robust statistical analyses based on large samples are vital in my opinion.

At the same time, it is as crucial to continue looking for early galaxies and to try to define a clear boundary for the beginning of the reionization era. Extensive observations of the skies, with more and more advanced instruments, are of course the primary tool for achieving this goal. But simulations of different types is equally important.

The Georgian Coat of Arms says "the strength is in unity", and for cosmology this saying holds true. Bringing together our analyses, methods, knowledge, and intelligence is the fastest (and probably the only) way to solve the mystery of the formation and evolution of the universe.

A

THUMBNAIL IMAGES

In this Appendix, I collect all thumbnail images for the emission-line candidates studied in Chap. 2 and Chap.3.
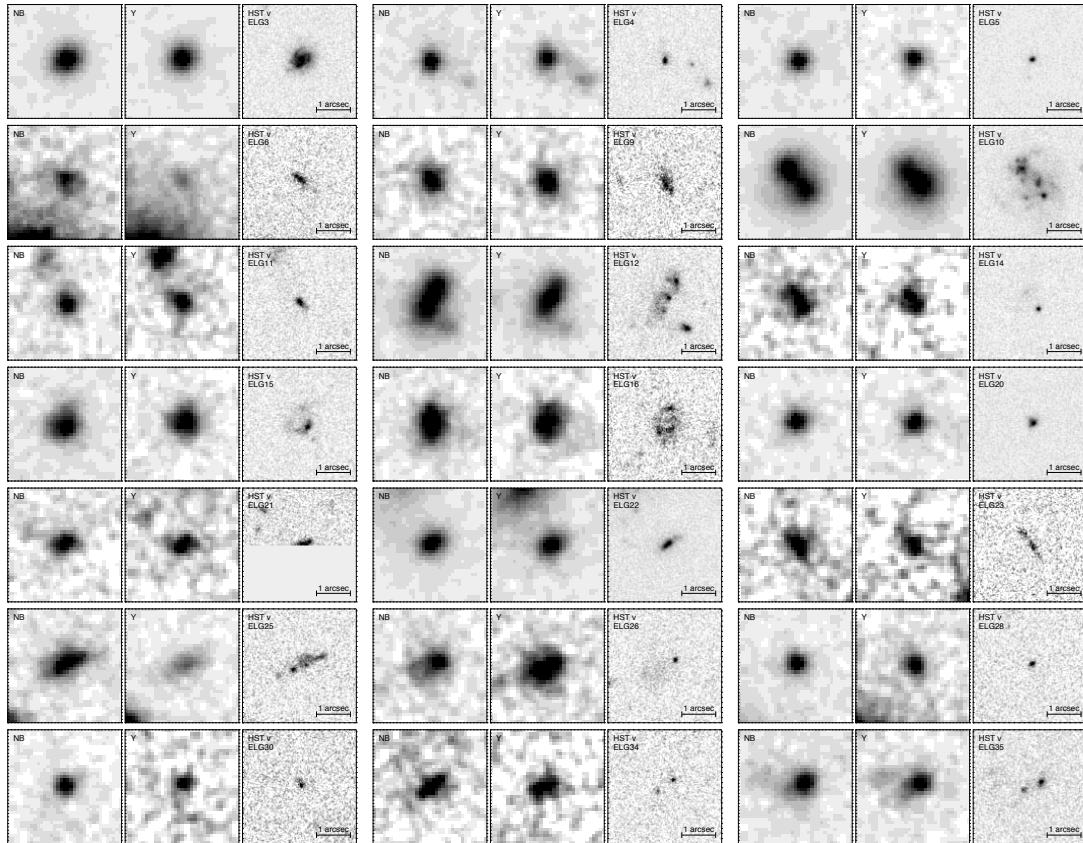

Figure A.1: Thumbnail images of the $NB1060$, Y, and HST F606W ("v band") filters for the candidates selected from $NB1060 - Y$ and $NB1060 - J$ colours and the additional source (ELG00) only detected including the $NB1060 - J$ colour. A $1''$ bar is given on the panels.
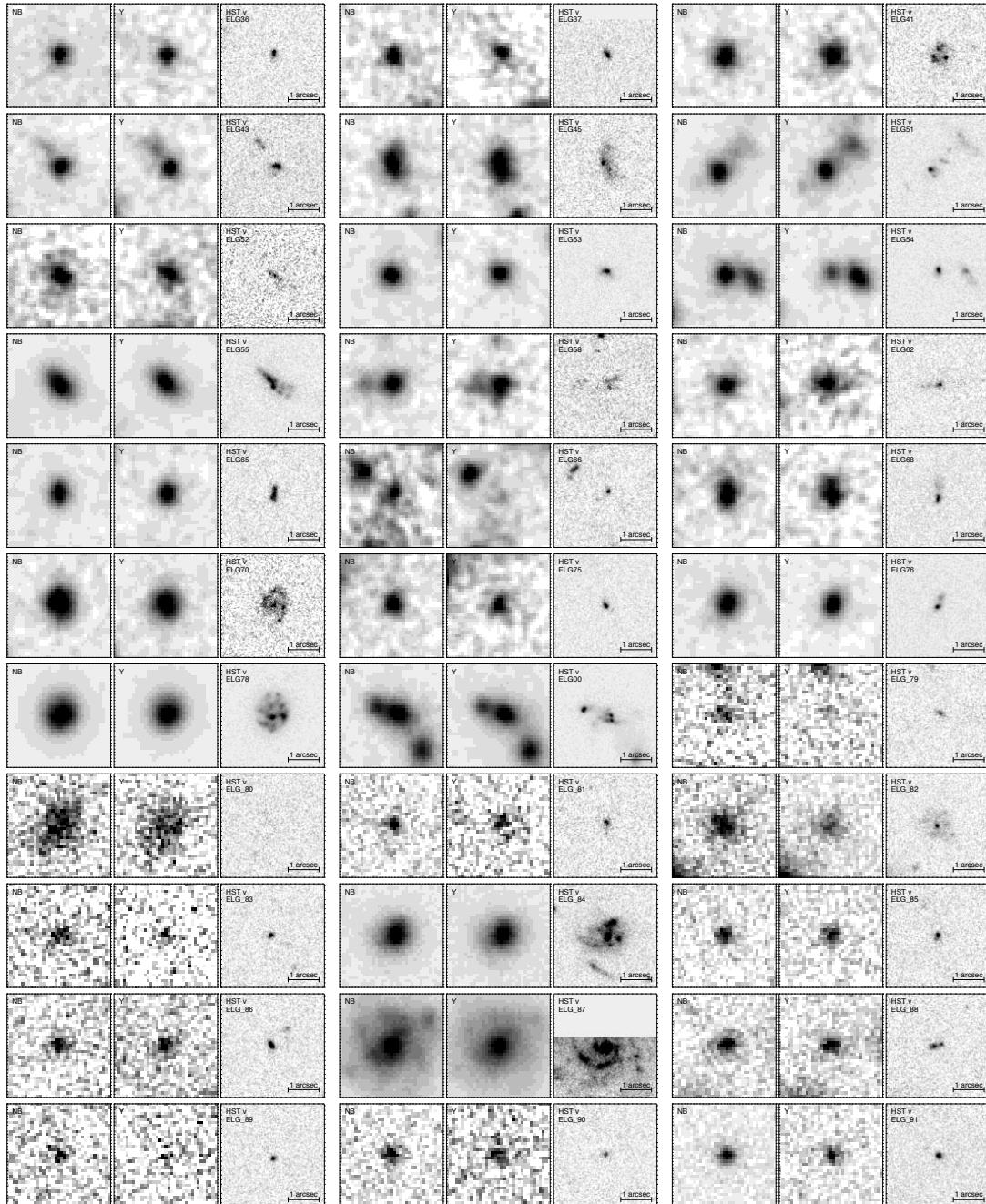
Figure A.1:   Contunued
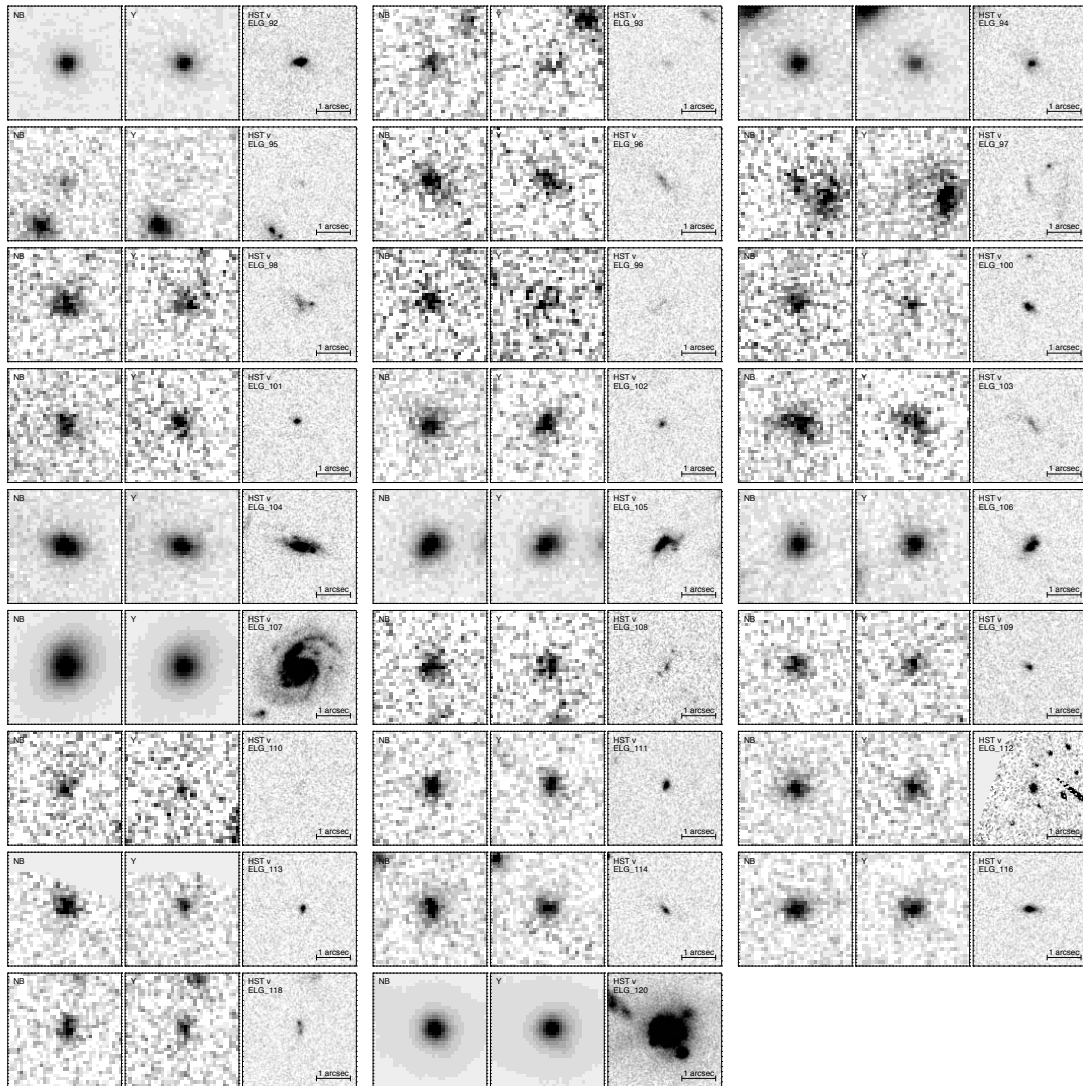
Figure A.1: Contunued

B

SED fits for candidate emission-line galaxies
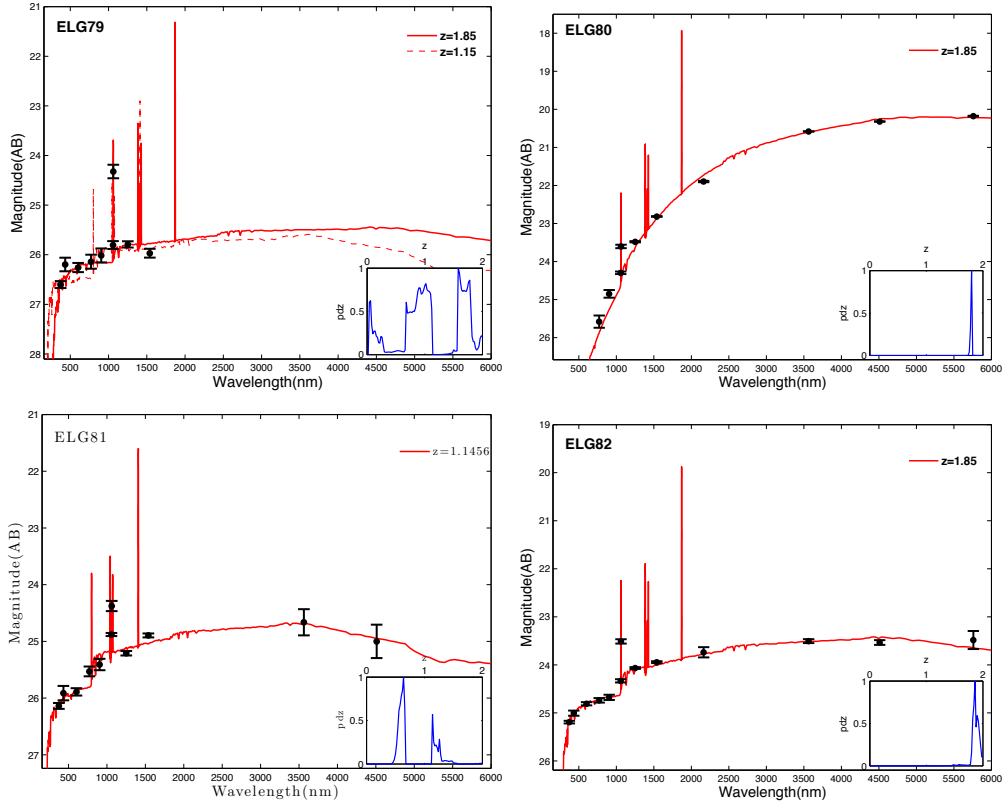
Figure B.1: SED fits (excluding the narrow-band) for all new ELG candidates found in this study. In cases where we have multiple (two or three) solutions considered equally plausible we plot all considered solutions. We only plot bands in which the source is detected (not upper limits).
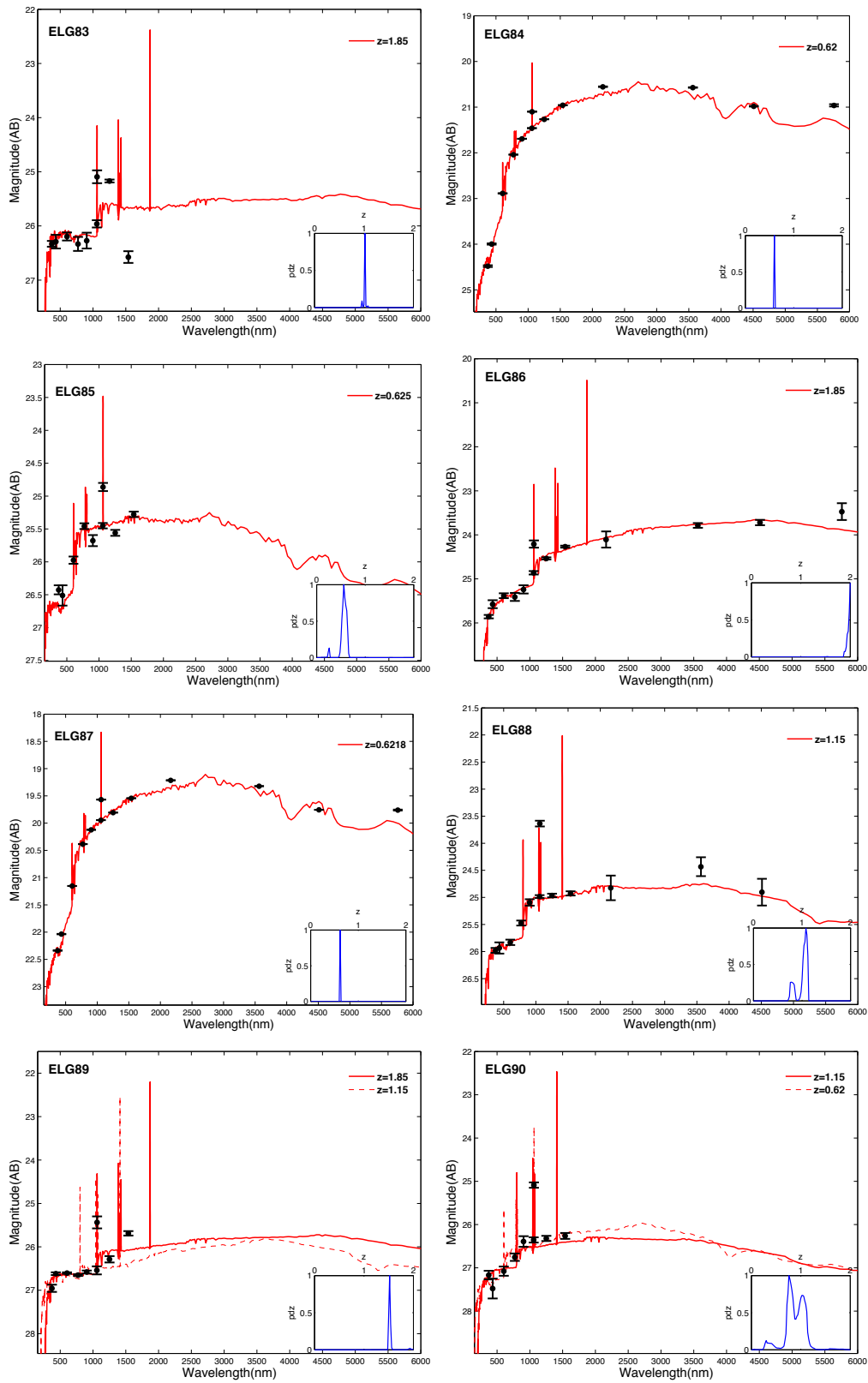
Figure B.1: continued.
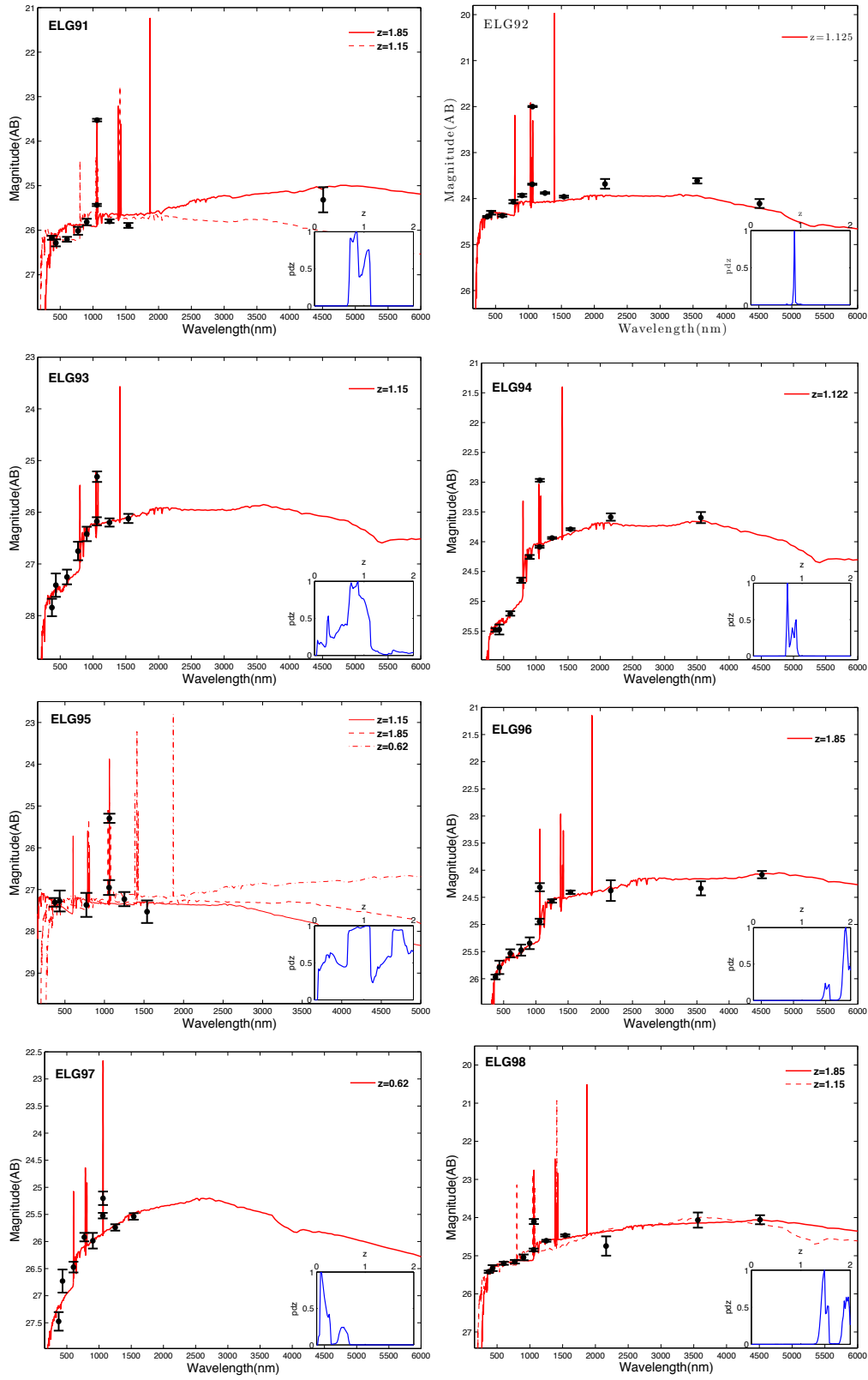
Figure B.1: continued.
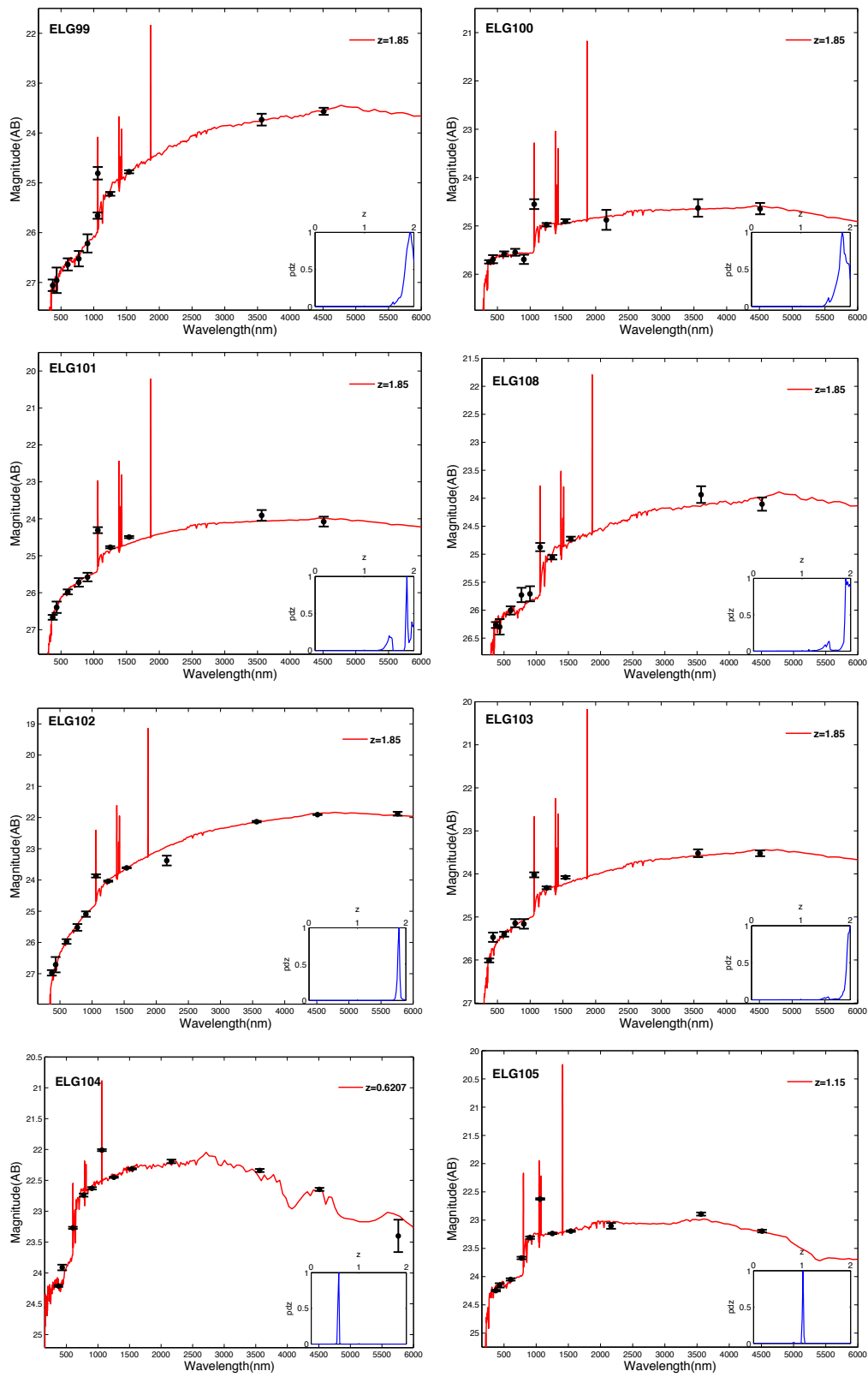
Figure B.1: continued.
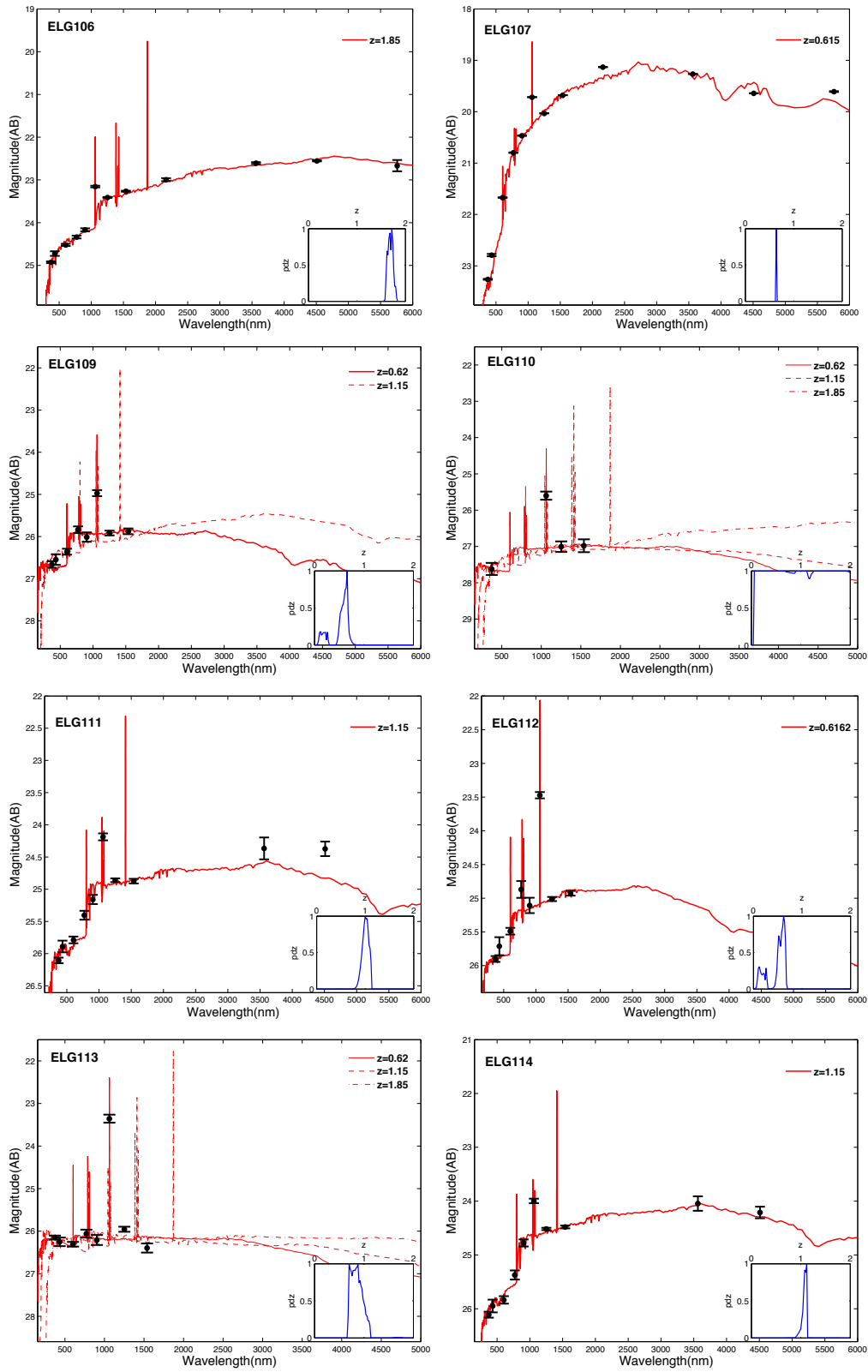
Figure B.1: continued.
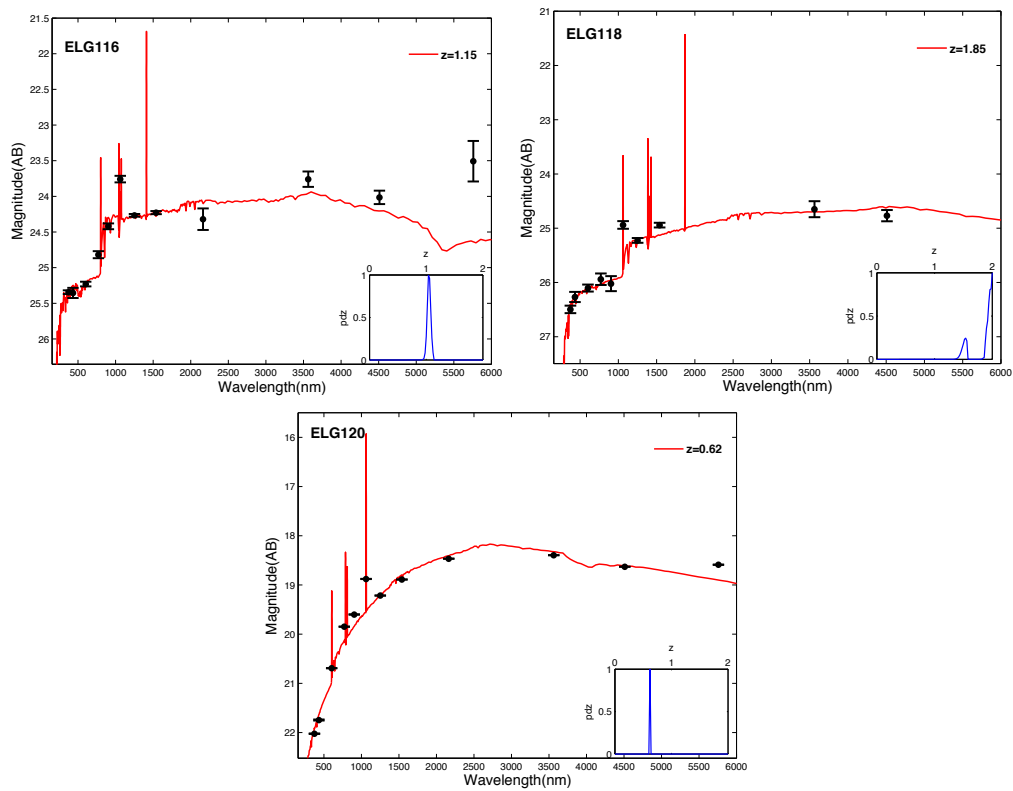
Figure B.1: continued.

Bibliography

Aaronson, M. & Mould, J. 1983, ApJ, 265, 1

Anderson, L. D., Bania, T. M., Jackson, J. M., et al. 2009, ApJS, 181, 255

Arabsalmani, M., Møller, P., Fynbo, J. P. U., et al. 2015, MNRAS, 446, 990

Arnouts, S., Cristiani, S., Moscardini, L., et al. 1999, MNRAS, 310, 540

Balestra, I., Mainieri, V., Popesso, P., et al. 2010, A&A, 512, A12

Baumann, D. 2009, ArXiv e-prints

Bayliss, K. D., McMahon, R. G., Venemans, B. P., Ryan-Weber, E. V., & Lewis, J. R.
    2011, MNRAS, 413, 2883

Bertin, E. & Arnouts, S. 1996, A&AS, 117, 393

Bolzonella, M., Miralles, J.-M., & Pelló, R. 2000, A&A, 363, 476

Brammer, G. B., van Dokkum, P. G., & Coppi, P. 2008, ApJ, 686, 1503

Brammer, G. B., van Dokkum, P. G., Illingworth, G. D., et al. 2013, ApJ, 765, L2

Brinchmann, J., Charlot, S., White, S. D. M., et al. 2004, MNRAS, 351, 1151

Bruzual, G. & Charlot, S. 2003, MNRAS, 344, 1000

Burgarella, D., Heinis, S., Magdis, G., et al. 2011, ApJ, 734, L12

Calzetti, D. 2013, Star Formation Rate Indicators, ed. J. Falcón-Barroso & J. H. Knapen,
    419

Calzetti, D., Armus, L., Bohlin, R. C., et al. 2000, ApJ, 533, 682

Cardamone, C. N., van Dokkum, P. G., Urry, C. M., et al. 2010, ApJS, 189, 270

Castellano, M., Fontana, A., Boutsia, K., et al. 2010, A&A, 511, A20

Castro Cerón, J. M., Michałowski, M. J., Hjorth, J., et al. 2010, ApJ, 721, 1919

Cervantes-Cota, J. L. & Smoot, G. 2011, in American Institute of Physics Conference Series, Vol. 1396, American Institute of Physics Conference Series, ed. L. A. Ureña-López, H. Aurelio Morales-Técotl, R. Linares-Romero, E. Santos-Rodríguez, & S. Estrada-Jiménez, 28–52

Cesarsky, C. 2000, The Messenger, 101, 1

Chabrier, G. 2003, PASP, 115, 763

Christensen, L., Hjorth, J., & Gorosabel, J. 2004, A&A, 425, 913

Christensen, L., Møller, P., Fynbo, J. P. U., & Zafar, T. 2014, MNRAS, 445, 225

Christensen, L., Richard, J., Hjorth, J., et al. 2012, MNRAS, 427, 1953

Clément, B., Cuby, J.-G., Courbin, F., et al. 2012, A&A, 538, A66

Coe, D., Zitrin, A., Carrasco, M., et al. 2013, ApJ, 762, 32

Coleman, G. D., Wu, C.-C., & Weedman, D. W. 1980, ApJS, 43, 393

Conselice, C. J., Bershady, M. A., & Gallagher, III, J. S. 2000, A&A, 354, L21

Daddi, E., Dickinson, M., Morrison, G., et al. 2007, ApJ, 670, 156

de Vaucouleurs, G. 1948, Annales d'Astrophysique, 11, 247

de Vaucouleurs, G. 1974, in IAU Symposium, Vol. 58, The Formation and Dynamics of Galaxies, ed. J. R. Shakeshaft, 1–52

Demiański, M. & Doroshkevich, A. G. 1999, MNRAS, 306, 779

Djorgovski, S. & Davis, M. 1987, ApJ, 313, 59

Einstein, A. 1915, Sitzungsberichte der Königlich Preußischen Akademie der Wissenschaften (Berlin), Seite 778-786., 778

Faber, S. M. & Jackson, R. E. 1976, ApJ, 204, 668

Fioc, M. & Rocca-Volmerange, B. 1999, ArXiv Astrophysics e-prints

Fisher, J. R. & Tully, R. B. 1975, A&A, 44, 151

Friedmann, A. 1922, Zeitschrift fur Physik, 10, 377

Furlanetto, S. R., Oh, S. P., & Briggs, F. H. 2006, PhysRep, 433, 181

Fynbo, J. P. U., Geier, S. J., Christensen, L., et al. 2013, MNRAS, 436, 361

Fynbo, J. P. U., Laursen, P., Ledoux, C., et al. 2010, MNRAS, 408, 2128 (F10)

Fynbo, J. P. U., Ledoux, C., Møller, P., Thomsen, B., & Burud, I. 2003, A&A, 407, 147

Fynbo, J. P. U., Ledoux, C., Noterdaeme, P., et al. 2011, MNRAS, 413, 2481

Geach, J. E., Alexander, D. M., Lehmer, B. D., et al. 2009, ApJ, 700, 1

Giavalisco, M. 2002, ARA&A, 40, 579

Giavalisco, M., Ferguson, H. C., Koekemoer, A. M., et al. 2004, ApJ, 600, L93

Girardi, L., Bressan, A., Bertelli, G., & Chiosi, C. 2000, A&AS, 141, 371

Goldoni, P. 2011, Astronomische Nachrichten, 332, 227

Guo, Y., Ferguson, H. C., Giavalisco, M., et al. 2013, ApJS, 207, 24

Guo, Y., Giavalisco, M., Ferguson, H. C., Cassata, P., & Koekemoer, A. M. 2012, ApJ, 757, 120

Gutiérrez, R., Solano, E., Sarro, L. M., & Resa, R. 2011, in Highlights of Spanish Astrophysics VI, ed. M. R. Zapatero Osorio, J. Gorgas, J. Maíz Apellániz, J. R. Pardo, & A. Gil de Paz, 776–776

Hodge, J. A., Karim, A., Smail, I., et al. 2013, ApJ, 768, 91

Hubble, E. 1926, Contributions from the Mount Wilson Observatory / Carnegie Institution of Washington, 324, 1

Hubble, E. 1929, Contributions from the Mount Wilson Observatory, vol. 3, pp.23-28, 3, 23

Hubble, E. P. 1925, The Observatory, 48, 139

Hubble, E. P. 1936, Realm of the Nebulae

Ilbert, O., Arnouts, S., McCracken, H. J., et al. 2006, A&A, 457, 841

Jacobs, B. A., Sanders, D. B., Rupke, D. S. N., et al. 2011, AJ, 141, 110

Karim, A., Schinnerer, E., Martínez-Sansigre, A., et al. 2011, ApJ, 730, 61

Kennicutt, R. C. & Evans, N. J. 2012, ARA&A, 50, 531

Kennicutt, Jr., R. C. 1998, ARA&A, 36, 189

Kirby, E. N., Cohen, J. G., Guhathakurta, P., et al. 2013, ApJ, 779, 102

Knapen, J. H. & James, P. A. 2009, ApJ, 698, 1437

Kochiashvili, I., Møller, P., Milvang-Jensen, B., et al. 2015, A&A, 580, A42

Koyama, Y., Smail, I., Kurk, J., et al. 2013, MNRAS, 434, 423

Kroupa, P. 2001, MNRAS, 322, 231

Krühler, T., Greiner, J., Schady, P., et al. 2011, A&A, 534, A108

Le Fèvre, O., Tasca, L. A. M., Cassata, P., et al. 2015, A&A, 576, A79

Le Fèvre, O., Vettolani, G., Paltani, S., et al. 2004, A&A, 428, 1043

Le Floc'h, E., Duc, P.-A., Mirabel, I. F., et al. 2003, A&A, 400, 499

Ledoux, C., Petitjean, P., Fynbo, J. P. U., Møller, P., & Srianand, R. 2006, A&A, 457, 71

Lee, N., Sanders, D. B., Casey, C. M., et al. 2015, ApJ, 801, 80

Lejeune, T. & Schaerer, D. 2001, A&A, 366, 538

Lemaître, G. 1931, MNRAS, 91, 483

Longair, M. S. 2008, Galaxy Formation

Ly, C., Malkan, M. A., Kashikawa, N., et al. 2012, ApJ, 757, 63

Maiolino, R., Nagao, T., Grazian, A., et al. 2008, A&A, 488, 463

Malhotra, S. & Rhoads, J. E. 2004, ApJ, 617, L5

Matsuda, Y., Yamada, T., Hayashino, T., et al. 2005, ApJ, 634, L125

Matthee, J., Sobral, D., Santos, S., et al. 2015, ArXiv e-prints

McCracken, H. J., Milvang-Jensen, B., Dunlop, J., et al. 2012, A&A, 544, A156

Mei, S., Scarlata, C., Pentericci, L., et al. 2015, ApJ, 804, 117

Melchior, P., Suchyta, E., Huff, E., et al. 2015, MNRAS, 449, 2219

Michałowski, M., Hjorth, J., & Watson, D. 2010, A&A, 514, A67

Mignoli, M., Cimatti, A., Zamorani, G., et al. 2005, A&A, 437, 883

Miller, G. E. & Scalo, J. M. 1979, ApJS, 41, 513

Milvang-Jensen, B., Freudling, W., Zabl, J., et al. 2013, A&A, 560, A94

Mo, H., van den Bosch, F. C., & White, S. 2010, Galaxy Formation and Evolution

Møller, P. & Warren, S. J. 1998, MNRAS, 299, 661

Mohr, J. J., O'Shea, B., Evrard, A. E., Bialek, J., & Haiman, Z. 2003, Nuclear Physics B Proceedings Supplements, 124, 63

Møller, P., Fynbo, J. P. U., Ledoux, C., & Nilsson, K. K. 2013, MNRAS, 430, 2680

Møller, P. & Fynbo, J. U. 2001, A&A, 372, L57

Møller, P. & Warren, S. J. 1993, A&A, 270, 43

Monaco, P., Møller, P., Fynbo, J. P. U., et al. 2005, A&A, 440, 799

Morris, A. M., Kocevski, D. D., Trump, J. R., et al. 2015, AJ, 149, 178

Natarajan, A. & Yoshida, N. 2014, Progress of Theoretical and Experimental Physics, 2014, 060000

Nilsson, K. K., Orsi, A., Lacey, C. G., Baugh, C. M., & Thommes, E. 2007, A&A, 474, 385

Nilsson, K. K., Östlin, G., Møller, P., et al. 2011, A&A, 529, A9

Noeske, K. G., Weiner, B. J., Faber, S. M., et al. 2007, ApJ, 660, L43

Oyaizu, H., Lima, M., Cunha, C. E., Lin, H., & Frieman, J. 2008, ApJ, 689, 709

Partridge, R. B. & Peebles, P. J. E. 1967, ApJ, 147, 868

Peebles, P. J. E., Schramm, D. N., Kron, R. G., & Turner, E. L. 1991, Nature, 352, 769

Pénin, A., Cuby, J.-G., Clément, B., et al. 2014, ArXiv e-prints, arXiv:1410.5558

Perlmutter, S., Aldering, G., Goldhaber, G., et al. 1999, ApJ, 517, 565

Planck Collaboration, Ade, P. A. R., Aghanim, N., et al. 2014, A&A, 571, A16

Pritchet, C. J. & Hartwick, F. D. A. 1987, ApJ, 320, 464

Rauch, M., Haehnelt, M., Bunker, A., et al. 2008, ApJ, 681, 856

Ravikumar, C. D., Puech, M., Flores, H., et al. 2007, A&A, 465, 1099

Riess, A. G., Filippenko, A. V., Challis, P., et al. 1998, AJ, 116, 1009

Robertson, H. P. 1935, ApJ, 82, 284

Rodighiero, G., Cimatti, A., Gruppioni, C., et al. 2010, A&A, 518, L25

Rodighiero, G., Daddi, E., Baronchelli, I., et al. 2011, ApJ, 739, L40

Rodrigues, M., Hammer, F., Flores, H., et al. 2008, A&A, 492, 371

Ryden, B. 2003, Introduction to cosmology

Salpeter, E. E. 1955, ApJ, 121, 161

Seo, H.-J. & Eisenstein, D. J. 2003, ApJ, 598, 720

Sérsic, J. L. 1963, Boletin de la Asociacion Argentina de Astronomia La Plata Argentina, 6, 41

Shapley, A. E. 2011, ARA&A, 49, 525

Slipher, V. M. 1914, Lowell Observatory Bulletin, 2, 66

Sobral, D., Best, P. N., Smail, I., et al. 2014, MNRAS, 437, 3516

Sobral, D., Matthee, J., Darvish, B., et al. 2015, ArXiv e-prints

Sofue, Y. & Rubin, V. 2001, ARA&A, 39, 137

Songaila, A. 2004, AJ, 127, 2598

Steidel, C. C., Adelberger, K. L., Shapley, A. E., et al. 2003, ApJ, 592, 728

Steidel, C. C., Giavalisco, M., Pettini, M., Dickinson, M., & Adelberger, K. L. 1996, ApJ, 462, L17

Steidel, C. C. & Hamilton, D. 1993, AJ, 105, 2017

Straughn, A. N., Kuntschner, H., Kümmel, M., et al. 2011, AJ, 141, 14

Straughn, A. N., Meurer, G. R., Pirzkal, N., et al. 2008, AJ, 135, 1624

Szokoly, G. P., Bergeron, J., Hasinger, G., et al. 2004, ApJS, 155, 271

Tanvir, N. R., Fox, D. B., Levan, A. J., et al. 2009, Nature, 461, 1254

Tempel, E., Stoica, R. S., Martínez, V. J., et al. 2014, MNRAS, 438, 3465

Tremonti, C. A., Heckman, T. M., Kauffmann, G., et al. 2004, ApJ, 613, 898

Trump, J. R., Weiner, B. J., Scarlata, C., et al. 2011, ApJ, 743, 144

Vanzella, E., Cristiani, S., Dickinson, M., et al. 2008, A&A, 478, 83

Vanzella, E., Cristiani, S., Dickinson, M., et al. 2005, A&A, 434, 53

Vanzella, E., Cristiani, S., Dickinson, M., et al. 2006, A&A, 454, 423

Vanzella, E., Giavalisco, M., Dickinson, M., et al. 2009, ApJ, 695, 1163

Vernet, J., Dekker, H., D'Odorico, S., et al. 2011, A&A, 536, A105

Villforth, C., Sarajedini, V., & Koekemoer, A. 2012, MNRAS, 426, 360

Walker, A. G. 1937, PLMS, 42, 90

Warren, S. J. & Møller, P. 1996, A&A, 311, 25

Weatherley, S. J., Warren, S. J., Møller, P., et al. 2005, MNRAS, 358, 985

Weidinger, M., Møller, P., Fynbo, J. P. U., Thomsen, B., & Egholm, M. P. 2002, A&A, 391, 13

Wenger, M., Oberto, A., Bonnarel, F., et al. 2007, in Astronomical Society of the Pacific Conference Series, Vol. 377, Library and Information Services in Astronomy V, ed. S. Ricketts, C. Birdie, & E. Isaksson, 197

Whitaker, K. E., Franx, M., Leja, J., et al. 2014, ApJ, 795, 104

Wolf, C., Dye, S., Kleinheinrich, M., et al. 2001, A&A, 377, 442

Woltjer, L. 2006, Europe's quest for the universe : ESO and the VLT, ESA and other projects

Xia, L., Malhotra, S., Rhoads, J., et al. 2011, AJ, 141, 64

Xu, C., Pirzkal, N., Malhotra, S., et al. 2007, AJ, 134, 169

Xue, Y. Q., Wang, S. X., Brandt, W. N., et al. 2012, ApJ, 758, 129